TÉCNICO LISBOA

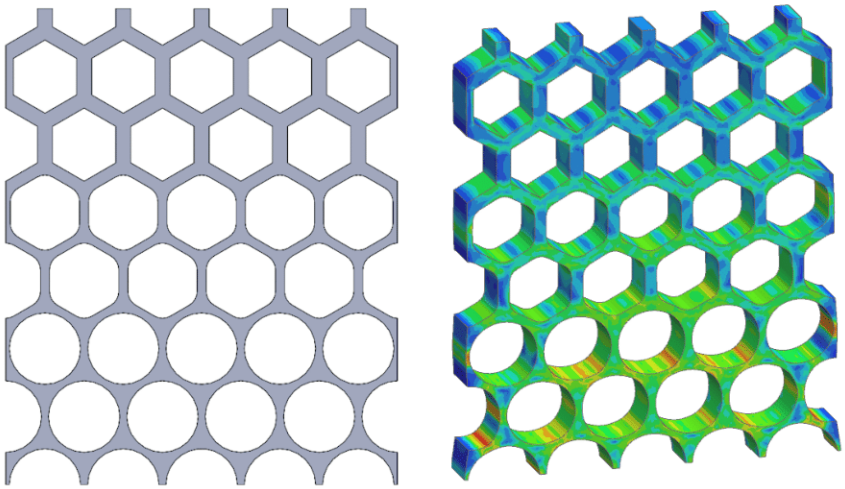

Modeling and Characterization of Novel Honeycomb Structures with Mass Gradient Produced by Additive Manufacturing Technologies

Luís Aser Castillo Portela

Thesis to obtain the Master of Science Degree in

Mechanical Engineering

Supervisors: Prof. Maria de Fátima Reis Vaz
Prof. Augusto Manuel Moura Moita de Deus

Examination Committee

Chairperson: Prof. Luís Filipe Galrão dos Reis
Supervisor: Prof. Augusto Manuel Moura Moita de Deus
Member of the Committee: Prof. Sofia Teixeira de Freitas

November 2023

Declaration

I declare that this document is an original work of my own authorship and that it fulfills all the requirements of the Code of Conduct and Good Practices of the Universidade de Lisboa.

This work was created using LaTeX typesetting language
in the Overleaf environment (www.overleaf.com).

Acknowledgments

I would like to firstly thank my supervisors, Professor Augusto Moita de Deus and Professor Maria Fátima Vaz, for their help and guidance throughout this work, as their advices helped me pave my way to success. I want to extend my gratitude towards Frederico Alves, whom provided me help and insight of finite element analysis. Also I would like to thank the faculty members of Instituto Superior Técnico who had a positive impact in my stay in this institution while I completed my educational process. I would like to thank Professor Etienne Copin from IMT Mines Albi, for their availability in producing the specimens used in my work.

To my parents, grandparents and my family, I appreciate your help and support throughout my life, to whom I wouldn't be who I am today, and wouldn't be where I am today. I would like to express my profound appreciation to my parents who always supported me and guided me into being the best version of myself. To my older sister Pilar, I would like to thank you for your advices which were very helpful. To my younger sister Victória, thank you for putting up with me. To my cousin Vicente, thank you for the bike trips and how the other's stop loss is my take profit.

To my favourite and only karaoke/board-gaming friend group. I would like to thank you for making this path less dull and mundane. Whether it be in lunches, the breaks in the "Esplanada de Civil", our karaoke sessions, educational presentations, board gaming afternoons or "studying" somewhere in a corner in IST. I would like to thank Afonso, Sofia, Alda, Lucas, Bea, Luís Miguel, Resende, Marta and Rafa for all the fond memories I have created with you. To my childhood friends Elias, Cunha, Araújo e Ascensão, a word of appreciation for all the good times we spent which helped me along the way. To Bernie and JéM, I will always remember our trio as the ones who share a single brain cell when it comes to our *unorthodox* humour.

Last but not least, I would like to show my appreciation to Joana who brought me the most positive impact I had here and who I wouldn't be who I am today. Through thick and thin, you were always there for me, and for that, I am evermore grateful. Thank you for your help, and dedication, and for putting up with me over the last five years.

To each and every one who helped me or had an impact on my life, I would like to thank you, for without you I would be who I am today.

Abstract

An increase in the use of honeycomb structures has been noted in the aerospace, automotive and prosthetic industries due to their low weight and high strength. The dissemination of additive manufacturing methods allowed the manufacture of more complex shapes, which were impossible with traditional methods such as die casting or machining. This work aims to study several types of metallic regular honeycombs and functionally graded honeycombs which were manufactured through Selective Laser Melting, a type of additive manufacturing, particularly a Laser Powder Bed Fusion Method. Three types of gradients were studied: regular gradients, radial gradients and linear gradients. These types of honeycombs have three configurations for the repeating units: regular hexagons, Plateau borders and Lotus. The compressive in-plane properties of the structures were evaluated using experiments and numerical simulations. In the experimental testing, the regular specimens with and without annealing were tested, and the ones with annealing were studied to investigate how the mechanical properties changed with said treatment. The numerical method resorted to the Finite Element Method to obtain the specific stiffness, energy absorbed and yield strength. The results indicated that the mechanical properties increased with an increase in the relative density. The Lotus configuration has the highest specific mechanical properties and reduces the stress concentrations within the honeycombs. The numerical simulations were accurate and matched well with the experimental results. The observed discrepancies were attributed to the limitations of the manufacturing method used.

Keywords

Additive Manufacturing; Cellular Materials; Functionally Graded Structures; Honeycombs Structures; Selective Laser Melting.

Resumo

Na industria aeroespacial, automóvel e prostetica, verificou-se um aumento do uso de estruturas de favo-de-mel, devido ao seu baixo peso e e alta resistência. A disseminação dos métodos de manufatura aditiva permitiu que se produzissem estruturas complexas que não seriam possiveis através dos métodos de manufatura convencionais como a fundição ou a maquinagem. Este trabalho tem como por objectivo estudar estruturas metálicas favo-de-mel regulares e com gradiente funcional que foram fabricadas através de *Selective Laser Melting*, que é um tipo de manufatura aditiva, nomeadamente *Laser Powder Bed Fusion*. Foram estudados três tipos de configurações para as unidades repetitivas: hexagonos regulares, com limites Plateau e Lotus. As propriedades mecânicas compressivas *in-plane* foram estudadas através de ensaios experimentais e numéricos. Na análise experimental foram ensaiados provetes regulares com e sem tratamento térmico sendo que os provetes com o tratamento térmico serviram para averiguar a sensibilidade das propriedades mecânicas das estruturas a este tratamento. O método numérico recorreu ao Método dos Elementos Finitos para obter a rigidez, energia absorvida e tensão de cedência específica. Os resultados indicam que um aumento da densidade relativa traduz-se num aumento das propriedades mecânicas. Também foi possível averiguar que a configuração Lotus tem as melhores propriedades mecânicas específicas que as outras configurações e é capaz de dissipar melhor as concentrações de tensões. Foi possível concluir que os resultados numéricos são precisos e existe uma boa correlação com os experimentais. As discrepâncias entre os resultados numéricos e experimentais advêm das limitações do método de manufatura.

Palavras Chave

Manufatura Aditiva; Materiais Celulares; Estruturas com Gradiente Funcional; Estruturas Favo-de-mel; *Selective Laser Melting*.

Contents

List of Figures

List of Tables

Acronyms

2D	Two-dimensional
AM	Additive Manufacturing
ASTM	American Society for Testing and Materials
BJT	Binder Jetting
CAD	Computer Aided Design
CNC	Computer Numerical Control
CPU	Central Processing Unit
DED	Directed Energy Deposition
Exp	Experimental
FEA	Finite Element Analysis
FEM	Finite Element Method
FFF	Fused Filament Fabrication
FGCM	Functionally Graded Cellular Material
FGM	Functionally Graded Material
GEI	Geometric Efficiency Index
HPL	Hexagonal-Plateau-Lotus
HT	Heat Treatment
ISO	International Organization for Standarization
L-PBF	Laser Powder Bed Fusion
LHP	Lotus-Hexagonal-Plateau
MEX	Material Extrusion
MJT	Material Jetting
Num	Numerical

NX	Siemens NX
PBF	Powder Bed Fusion
PLH	Plateau-Lotus-Hexagonal
Pt	Plateau
RAM	Random Access Memory
SHL	Sheet Lamination
SLM	Selective Laser Melting
SLS	Selective Laser Sintering
STL	Standard Triangle Language
TPMS	Triply Periodic Minimal Surfaces
TPU	Thermoplastic polyurethane
VPP	Vat Photopolymerization

List of Symbols

$\bar{\rho}$	Relative density
ρ^*	Density of the cellular material
ρ_s	Density of the solid
m^*	Mass of the cellular material
m_s	Mass of the solid
V^*	Volume of the cellular material
V_s	Volume of the solid
A_s	Area of the solid
A_T	Total area
A^*	Area of the cellular material
K	Stiffness
$\bar{K}$	Relative stiffness
E_a	Energy absorbed
$\bar{E_a}$	Relative energy absorbed
σ_y	Yield strength
$\bar{\sigma}_y$	Relative yield strength
E	Young's modulus
σ	Stress
ϵ	Strain
ϵ_R	Real strain
ϵ_N	Nominal strain
L_1	Length of the side of the inner hexagon
L_2	Length of the side of the outer hexagon
e	Repeating unit cell wall thickness
t	Wall thickness between two inner hexagons
r	Plateau border corner radius

R	Lotus border radius
l	Length of the structure
w	Width of the structure
A_{T_i}	Total area of the configuration i
$\bar{\rho}_i$	Relative configuration of the configuration i
L_{1_i}	Length of the side of the inner hexagon of the configuration i
F_y	Yield force
R^2	Coefficient of determination
K^*	Stiffness of the cellular material
K_s	Stiffness of the solid
$E_a{}^*$	Energy absorbed of the cellular material
E_{a_s}	Energy absorbed of the solid
$\sigma_y{}^*$	Yield strength of the cellular material
σ_{y_s}	Yield stregnth of the solid

1

Introduction

Contents

1.1 Motivation

When looking for solutions to a given problem, engineers often look at nature, as it has the best naturally occurring solution. Honeycombs were one solution found by observing the way bees build their beehives and how they store their honey. Gibson and Ashby classified honeycombs as two-dimensional cellular materials with an arrangement of cells with solid edges that repeat periodically [1].

The structures were first used in the aviation industry due to their high strength-to-weight ratio, as early as the 1920s [2]. As time moved on, honeycombs found their way into other industries such as the automotive or the prosthetic sector.

As the honeycombs were exploited by other sectors, their complexity began to increase, the regular hexagons started to change their dimensions according to their position such that the structure would sustain higher forces whilst maintaining a low mass. Also, the regular hexagons became rounded or even changed shape completely to fit other needs. In some cases, the regular honeycombs were replaced by functionally graded honeycombs. The honeycombs started to be combined with other materials to further increase their resistance, for instance, the sandwich panels were created, in which the honeycombs were combined with carbon-fibre reinforced polymer which has an outstanding resistance in the out-of-plane direction and in-plane resistance.

With the development of the Additive Manufacturing (AM) techniques, such as Fused Filament Fabrication (FFF) for polymers - also known as 3D printing - and Laser Powder Bed Fusion for metals, it became cost-effective to use such methods to produce honeycombs. Moreover, these techniques allow the manufacture of shapes that were not available through other traditional methods hence, a broader range of solutions became feasible.

1.2 Objectives

This thesis aims to characterize the in-plane mechanical properties of the regular and functionally graded honeycomb structures with three configurations: regular hexagons, Lotus and Plateau borders. These specimens were produced by additive manufacturing, more specifically through Selective Laser Melting (SLM). The characterization of the mechanical properties was made with experimental in-plane compression tests on some structures and a Finite Element Analysis (FEA) on all structures. Furthermore, the FEA and the practical tests will be compared to assess the accuracy of said analysis. This study follows up on the thesis done by Bernardo Coelho [3] for his Master's thesis in Materials Engineering.

The main talking points of this work will be the following:

- Assess the influence of the several configurations for the borders of the structure - regular hexag-

onal, Lotus and Plateau borders - on the compressive properties;

- Compare different types of regular and functionally graded honeycombs resorting to their mechanical properties;
- Evaluate the efficacy of the configuration and the gradient of the structure;
- Evaluate the accuracy of the FEA model when compared to the experimental results.

1.3 Organization of the document

This thesis has an Introduction in Chapter 1, followed by the State of the art in Chapter 2. Afterwards, the Materials and Methods are presented in Chapter 3, together with the CAD modelling, the numerical and experimental methodology. Then in Chapter 4 it is presented the Results and discussion, together with a Performance analysis of the structures. Lastly, the Conclusions are presented in Chapter 5. The appendices are in Appendix A and Appendix B.

2

State of the art

Contents

The state of the art covers the definition of a cellular solid, then moves into a subcategory of cellular solids: functionally graded cellular materials. Afterwards, it will be looked into manufacturing methods, more specifically, additive manufacturing, and a heating treatment. Lastly it will be presented the scientific gap that this work fulfills.

2.1 Cellular solids

Cellular solids are structures made up of "cells with solid edges of faces, packed together so that they fill space" [1]. These types of structures are naturally occurring materials, such as honeycombs from beehives, cork, and wood, among others [4]. Some can even be graded, such as the ones of bones [5]. Ashby *et al.* [1] goes further into the definition of a cellular structure by resorting to the structure's relative density ($\bar{\rho}$). The relative density is defined by the ratio between the density of the cellular material (ρ^*) and the solid's density (ρ_s), *i.e.* the density of the material. This ratio is shown in Equation 2.1. A cellular solid is said to be one if the relative density is below 0.3, otherwise, the structure might have isolated pores.

$$\bar{\rho} = \frac{\rho^*}{\rho_s} \tag{2.1}$$

D. Bhate *et al.* [6] define that a cellular structure can be classified through three categories (Figure 2.1). These categories can be seen as the possible way a cellular solid can be built. The first category that is mentioned is *tessellation*, which is the most basic form of cellular materials. Tessellation consists in building a cellular solid by filling the space with cells such that no gap is left to fill, the authors deepen this definition by organizing several sub-categories of tessellation, those being *periodical*, *stochastic* and *hierarchical*.

Periodical tessellation is made with the propagation of one or several repeating units; Figure 2.2 outlines the types of periodic tessellation.

Stochastic tessellation is built without a repeating unit. D. Bhate *et al.* [6] and Møller [7] point out several types of stochastic tessellation, those being the Point process, Random process, Poisson process, Germ-grain process and Voronoi and Delaunay tessellations. These processes are mathematically described in the work by J. Møller and D. Stoyan [7]. These types of tessellation are not very usual but can be seen in cracked mud (Figure 2.3) or in grain formation (Figure 2.4).

The last type of tessellation outlined by D. Bhate [6] is the hierarchical tessellation. This type of tessellation is often seen in nature for the veins on the wings of bugs [8] (Figure 2.5), branches of trees [9] (Figure 2.6) and the bone structure of humans [10] (Figure 2.7).

Another category in which cellular solids can be built is named *Elemental*. This one is mostly seen in sandwich panels where the "interior" of the sandwich resembles a truss. An example of this kind of

tessellation can be seen in Figure 2.8.

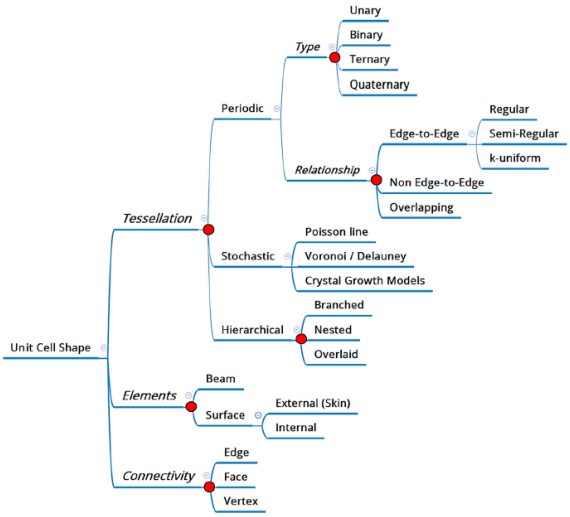

Figure 2.1: Cellular classification. Adapted from [6].

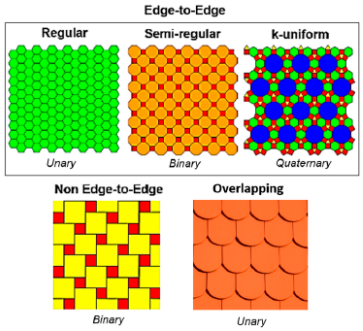

Figure 2.2: Types of periodic tessellation. Adapted from [6].

Figure 2.3: Cracked mud. Retrieved from [11].

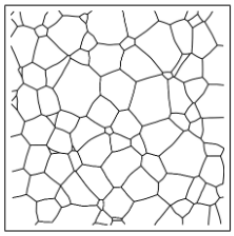

Figure 2.4: 2D and 3D grain-growth propagation. Adapted from [12].

Figure 2.5: Tessellation of a bug's wing. Adapted from [8].

Figure 2.6: Tessellation inside of a femur. Adapted from [10].

Figure 2.7: Tree branches hierarchical tessellation. Adapted from [9].

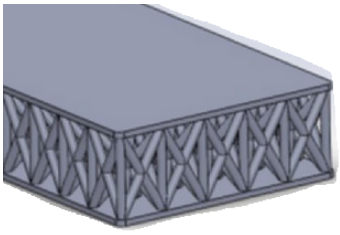

Figure 2.8: Elemental tessellation. Adapted from [13].

The last category mentioned by D. Bhate [6] is the *connectivity*, in which the repeating unit is made by Triply Periodic Minimal Surfaces (TPMS) (Figure 2.9). TPMS are defined by mathematical functions which in turn produce a non-intersecting, continuous surface. These surfaces have gained a foothold in the biotechnology and prosthetic industry as they are easily manufactured through additive manufactur-

ing techniques and their structures provide a high strength resistance [14–16].

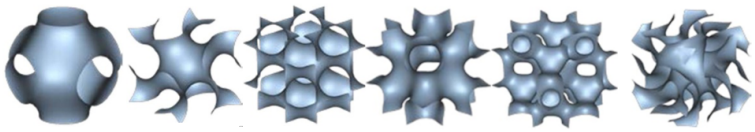

Figure 2.9: Several types of TPMS. Adapted from [17].

There are more applications for cellular solids which are outlined by Ashby *et al.* [18]. Besides the structural application, these can be used in heat exchangers or used in catalyst carriers (Figure 2.10).

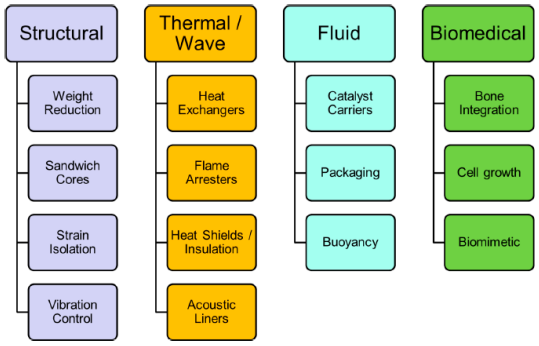

Figure 2.10: Applications of cellular solids. Adapted from [18].

2.2 Functionally Graded Cellular Materials

This section covers what defines a Functionally Graded Material (FGM) and the findings of several papers on this topic such influence of the geometry on the mechanical properties, the thickness of the cell walls and the gradient used in the structure. Furthermore, was also looked into the calculations required for the relative density of several structures.

2.2.1 An overview

A FGM is a material which repeating unit is not constant. Usually, the variation of the repeating unit follows a specific pattern, depending on the requirements, or loads applied to the structure. These structures are seldom seen in nature such as the bone structure, the vessels in the bug's wings or the honeycombs in beehives, and the tessellation or gradient of the repeating unit is adjusted to the needs. Within the FGM there are Functionally Graded Cellular Material (FGCM) and in these materials the dimensions of the unit cells can be changed according to sought in the context of the gradient [19].

A work by Ajdari *et al.* [20] studied the in-plane dynamic crushing of regular and irregular honeycombs and honeycombs with a linear density gradient. It was found that at high-velocity crushing, the structures

with a positive linear density gradient absorbed more energy than those without the gradient.

C. Lira and F. Scarpa [21] studied a similar gradient to the one used by Ajdari *et al.* [20], which involved increasing the thickness of the horizontal webs across an auxetic structure - a structure with a negative Poisson ratio, and a honeycomb structure. In their work, it was concluded that the gradient had significant improvements in the auxetic structure rather than the honeycomb in terms of the transverse shear moduli.

X. Zhang *et al.* [22] studied the in-plane properties of a linear density gradient on honeycomb structures under dynamic crushing. The gradients used by the authors consist of dividing a honeycomb structure into four equal horizontal sections. The density of each section is given by the permutation of four different values for the density, which gives rise to four different structures. In their work, it was found that an increase in the cell walls will increase the Plateau stress, but it will also shorten it, conversely, thinner cell walls would decrease the Plateau stress but it would lengthen it. Furthermore, it was found that placing the ”weakest” layer - which is the layer with thinner cell walls - closest to the fixed plate, would reduce the stress transmitted. Lastly, when performing a low-velocity test on the structures, it was found that there is a negligible influence on the crushing and overall stress response between the several arrangements.

X. Lijun and S. Weidong [23] studied the effect of a gradient on lattice structures manufactured through AM. The gradient designed by the authors follows a similar train of thought to what X. Zhang *et al.* [22] designed. The lattice was divided into horizontal slices with different densities, however, this time the slices became progressively thinner as in one structure there was a step-wise gradient and in the other, there was a continuous gradient. Both gradients were able to absorb more energy and were able to achieve a higher Plateau stress than their regular counterpart. Moreover, the continuous gradient was able to surpass by little the step-wise gradient in both the Plateau stress and the energy absorbed.

S. Bates *et al.* [24] studied the compressive behaviour of a Thermoplastic polyurethane (TPU) honeycomb with a step-wise linear gradient. Similar to the work of X. Lijun and S. Weidong [23], the structures in this work follow a linear pattern where the unit cell changes its dimension depending on the layer which is positioned. The layers are ordered with the lower densities on top and the higher densities on the bottom, and the authors decided to study the influence of the number of layers in the structure. It was found that the graded structures had, on average, 11% more energy absorption than their regular counterparts. Also, it was found that a more continuous grading would increase the Plateau stress in the stress-strain curves.

H. Liu [25] studied a honeycomb structure with a micro-architecture submitted to impact loading. The cell walls of the structures are either composed of a tessellation of triangles or hexagons. The authors chose regular structures with the tessellation of hexagons and triangles but also opted to study the impact of a linear variation of the density of the structure with both the triangles and hexagons. It was also

chosen to analyse three types of structures: a regular structure with a base unit cell which is propagated throughout the whole structure; a positive gradient, where a base cell is defined and the remaining cells have their density increased; a negative gradient where the same base cell is defined and the remaining ones have a lower density. The authors expected that an increase in strength was associated with an increase in the refinement of the tessellation *i.e.* the size of the triangles or hexagons used would be smaller and ultimately would increase the density. During the compression of the specimens, the authors found that the weaker sections *i.e.* the sections with lower density, were the first ones to collapse, followed by the ones with lower density and so on. Analysing the specific energy absorbed, it was observed that the hexagons sub-cells absorbed less energy than the triangles. Also the structures with a positive and negative gradient absorbed more energy than the regular counterpart, for lower impact velocities (3 $\sim$ 15 m/s), but for higher impact velocities (40 $\sim$ 60 m/s) the negative gradient had lower specific energy absorbed than the regular one, while the positive gradient kept a specific energy absorbed than the regular structure. Lastly, the authors noted that the deformation modes always followed an I-shape or a V-shape. This nomenclature will be explained in Section 2.2.3, further on.

Lastly, S. Bagewadi and R. Bhagchandani [26] in a recent work, studied the effect of gradient on auxetic structures to improve the energy absorption. In their work, it was found the importance of the filleted corner in the performance of the structures. In the compressive strength and modulus, the filleted structures had a better performance than the other gradient, while in the energy absorption field were behind the structures with variable unit cell dimensions, but by a small margin. This result will be relevant for the results of this work, in Chapter 4.

This work covers the study of several configurations for the repeating units which were the regular hexagons, hexagons with Plateau borders and Lotus, which were previously covered by A. Miranda *et al.* [27], H. Araújo *et al.* [28] and B. Silva *et al.* [19]. However, in the present work, covers these repeating unit, but applied to other gradients.

2.2.2 Relative density

In order to construct a FGCM, there are two lines of thought that can be followed. The first one is: the geometrical dimensions of the repeating unit are defined. Then, a gradient is defined and applied to the repeating units afterwards the relative density is calculated. In the second one: the relative density and gradient are set, and then the required dimensions are calculated according to it.

As it was shown in Section 2.1, the relative density is defined by Equation 2.1. However, if the structure that is being analysed is Two-dimensional (2D), the equation can be further simplified (Equation 2.2).

$$\bar{\rho} = \frac{\rho^*}{\rho_s} \Leftrightarrow \bar{\rho} = \frac{\frac{m^*}{V^*}}{\frac{m_s}{V_s}} \tag{2.2}$$

The m stands for mass, while V stands for Volume. The quantities with $*$ stand for those of the cellular material, and with the subscript s, stands for the quantities of the solid material. Since m^* is the same as m_s and since the thickness of the structure is constant Equation 2.3 can be drawn.

$$\bar{\rho} = \frac{V_s}{V^*} \Leftrightarrow \bar{\rho} = \frac{A_s}{A^*} \tag{2.3}$$

Since the area of the cellular material (A^*) is the same as the total area (A_T) occupied by the material, the equation 2.4 can be written as follows.

$$\bar{\rho} = \frac{A_s}{A_T} \tag{2.4}$$

Equation 2.4 is the general equation that can be applied when a CAD file is available however, further calculations are required to define the relative density when the geometrical dimensions are given and these are presented further in this work.

2.2.3 Mechanical properties

The in-plane properties are those measured when the structure is compressed or tractioned along the direction of the blue arrows in the Figure 2.11. The out-of-plane properties are measured when the structure is compressed or tractioned along the red arrows [1]. This work only focuses on the in-plane properties, hence these will be the only ones discussed in the coming sections.

The compressive in-plane stress-strain curves are characterised by three zones (Figure 2.12), which Gibson & Ashby shown in their work [1].

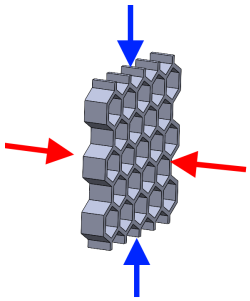

Figure 2.11: In-plane and out-of-plane directions

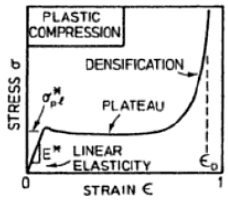

Figure 2.12: Stress-strain curve for the compressive test for an elastoplastic honeycomb. Retrieved from [1].

The compressive curve has an initial linear elasticity up to a critical stress at which the repeating units begin to collapse, then the bent cell walls form *plastic hinges* which will further bend the cell walls. After the critical stress, a Plateau zone is reached until the cell completely collapses and the opposing cell walls come into contact, then a section of high stress is achieved which corresponds to the densification. Before achieving densification, the honeycombs deforms in several modes which were

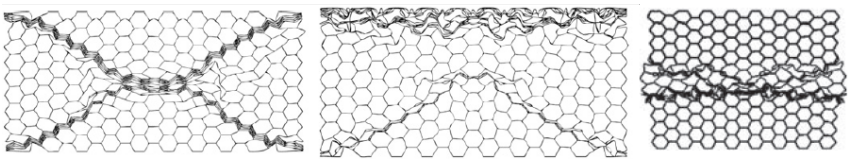

Figure 2.13: Localised deformation modes. [Note: X-, V- and I-shape, from left to right.] Adapted from [20, 22].

studied by Ajdari *et al.* [20] and by Zhang *et al.* [22]. The authors describe these deformation modes as "localised deformation modes" and they can take three shapes: X-, V- and I-shape (Figure 2.13.)

With the data obtained from the compression of a honeycomb structure, it is possible to draw a force-displacement curve similar to the curve found in Figure 2.12. From the data, it is possible to determine the stiffness (K), the energy absorbed (E_a) and the yield stress (σ_y). The stiffness is determined by calculating the linear slope of the linear elasticity zone of the force-displacement curve, the energy absorbed is determined by calculating the area under the force-displacement curve and the yield stress is determined by dividing the yield force, which is the last point in the linear region of the force-displacement curve, by the apparent area of the honeycomb, which is the contact area of the honeycomb with the compression plate. To compare the mechanical properties of different structures, it was used the specific stiffness (Equation 2.5), the specific energy absorbed (Equation 2.6) and the specific yield strength (Equation 2.7), as this take into account the mechanical properties and relative density of the structure. Consequently, the comparison between the mechanical properties of different structures is made under the same conditions.

$$\bar{K} = \frac{K}{\bar{\rho}} \tag{2.5}$$

$$\bar{E}_a = \frac{E_a}{\bar{\rho}} \tag{2.6}$$

$$\bar{\sigma}_y = \frac{\sigma_y}{\bar{\rho}} \tag{2.7}$$

2.3 Additive Manufacturing

AM is the process where a part is produced by adding/binding material layer-by-layer, such as FFF or SLM. Conversely, subtractive manufacturing is the opposite of AM, where the material is removed in order to produce a part, a few examples of the latter are drilling, machining and milling. This section focuses mainly on SLM and an overview of AM.

There are seven types of additive manufacturing techniques defined by the International Organization for Standarization (ISO)/American Society for Testing and Materials (ASTM) 52900:2021 [29]. The

techniques, their appropriate acronym, and a brief description provided below [30].

- **Binder Jetting (BJT)**: AM process in which a liquid bonding agent is selectively deposited to join powder materials;
- **Directed Energy Deposition (DED)**: AM process in which focused thermal energy is used to fuse materials by melting as they are being deposited;
- **Material Extrusion (MEX)**: AM process in which material is selectively dispensed through a nozzle or orifice;
- **Material Jetting (MJT)**: AM process in which droplets of feedstock material are selectively deposited;
- **Powder Bed Fusion (PBF)**: AM process in which thermal energy selectively fuses regions of a powder bed. The PBF methods that resort to lasers are also known as Laser Powder Bed Fusion (L-PBF);
- **Sheet Lamination (SHL)**: AM process in which sheets of material are bonded to form a part;
- **Vat Photopolymerization (VPP)**: AM process in which liquid photopolymer in a vat is selectively cured by light-activated polymerization.

From all of the processes described before, MEX is the most prominent since 3D printing falls within that category and since 2009, it has gained a foothold in the manufacturing market, particularly for polymers [31–33].

The rapid prototyping speed of these manufacturing methods comes at a cost which may be the warpage and cracking of the elements at the base of the structures. This comes from the rapid cooling of the parts, which then in turn produce residual stresses on the surface of the parts [34]. The residual stresses can be reduced by undergoing a heat treatment, such as annealing.

Since the scope of this work focuses on honeycombs manufactured through SLM, the following section will look into the SLM manufacturing method, as well as heat treatment annealing since it will be talked about further on in this work. Also, other conventional ways of manufacturing honeycombs. The heat treatment is an important part of the AM processes and it will be described further on.

2.3.1 Selective Laser Melting

SLM is an additive manufacturing technique which falls under the category of L-PBF, according to the standard ISO 52900-2021 [29]. In this process (Figure 2.14), a layer of the powder material is set over the substrate plate, then a laser beam is shed where it is desired to melt the material. After completing

this step, the substrate plate is lowered such that a newer layer of powder can be laid again, once again the laser will melt the areas which are intended to, and this process is repeated until the whole part is produced.

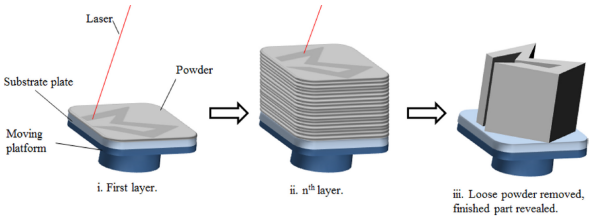

Figure 2.14: Representation of the SLM process. Retrieved from [35].

The patent for this process was first published in 1998 [36], and its initial steps are similar to those of Computer Numerical Control (CNC) machining: one must have a Computer Aided Design (CAD) file which must then be converted into an Standard Triangle Language (STL) file to be later processed by the appropriate software. The powder layers are usually between 20 to 100 μm as this range allows for good powder flowability and an adequate resolution [37]. The chamber where the process occurs has argon or nitrogen as an inert gas to prevent the part's oxidation.

When compared to Selective Laser Sintering (SLS) - another type of PBF manufacturing -, SLM has an advantage since it does not need to remove any support from the substrate. Furthermore, Yap *et al.* [35] state that SLM does not need post-processing such as heat treatment or material infiltration, which is required in SLS to improve the quality of the process, however, a heating treatment can be used to alter the mechanical properties of the material.

As of today, the SLM process is a prototyping manufacturing method, which means it has a short concept-to-prototype time [37], unlike other conventional manufacturing methods, such as material injection or milling. Moreover, unlike FFF, this process requires little to no support, as the "unmelted" powder will work as a support for the part. Thus it is possible to create more complex geometries that were otherwise impossible in conventional manufacturing and in FFF.

Due to the versatility of the process, its applications range from the aeronautical industry to the medical industry. In the medical field, Kruth *et al.* [38] has made a biocompatible metal framework for dental prostheses, which allows the patient to have a prosthesis specifically designed for them and not have to resort to a standard prosthesis which may not suit their needs. Also, in the field of heat exchangers, SLM allows the engineer to create complex cooling channels [39] which increase the heat exchange of the fluids, and thus increasing its efficacy.

2.3.2 Heat treatment: annealing

As it was mentioned before, parts made with SLM often need Heat Treatment (HT) to reduce residual stresses which could lead to the appearance of cracks. Hence it is of the utmost importance to reduce those in order to prevent fractures. Proaño *et al.* [40] present an accurate review of the defects of SLM manufacturing in terms of the material and its consequences in the crack appearance. Furthermore, the authors investigate the effect on the microstructure, the mechanical properties and the crack propagation of SLM-manufactured specimens with no heat treatment and two different annealing processes, one at 250 ℃ for 3h and the other one for 350 ℃ at 10h (Figure 2.15). Before diving into more specific details about the effect of the heating treatment, it is important to define what is an annealing heat treatment. The annealing heating treatment is a process where a structure is heated until a certain temperature via an oven or an oil bath, then kept at a constant temperature for a given time and then cooled down. The cooling down can be either forced or natural, whenever it is not mentioned the cooling process, it is assumed that it was not forced. Figure 2.15 is an example of the variation of the temperature with time for a heat treatment made in an oven and then cooled naturally outside of the oven.

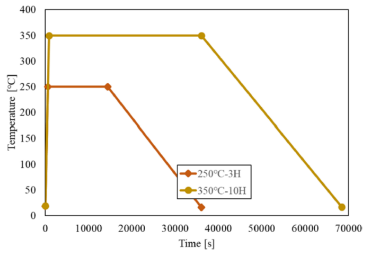

Figure 2.15: Heat treatment graph. Retrieved from [40].

Regarding the effect of the annealing on the properties of the material, the literature indicates that the annealing will increase the elongation before the fracture of the material and thereby the energy absorbed, the Young modulus will decrease and consequently so does the stiffness of the structure, and both the yield strength and ultimate tensile stress are decreased [41]. Lastly, it was also noted that the annealing process has no effect on the surface roughness [40].

2.4 Scientific gap

The literature review of this work covered several types of functionally graded structures and structures with different repeating units. These had a narrow array of structures evaluated or used polymeric materials for the structure. Hence this work aimed to fill the gap in the study of metallic structures manufactured through SLM and it also aimed at presenting a comparison between regular hexagonal honeycombs with different repeating units and different types of gradients.

3

Materials and methods

Contents

This chapter addresses the material used, the manufacturing method of the honeycombs and the CAD design of the structures.

3.1 Materials and manufacturing

All the structures were manufactured with AlSi7Mg0.6 (also designated as EN AC-42200) [42] through SLM according to the standard DIN 1706 [43]. The properties of the material are described in Table 3.1 [42]. The standard EN AC-422000 only provides the density, the Young modulus, the Poisson ratio, the yield strength and the ultimate tensile strength; the remaining amounts were either calculated or obtained from other works. The yield strain was calculated by applying Hooke's Law (Equation 3.1)

$$E = \frac{\sigma}{\epsilon} \tag{3.1}$$

where the *E* stands for Young's modulus, the σ stands for the stress and the ϵ for the strain. Since Young Modulus (59000 MPa) and yield strength (211 MPa) are given, it is clear that the yield strain will be 0.003576 mm/mm.

For the ultimate tensile strain, it is required to calculate the nominal value, as this is the one to be used in the FEA. To calculate such value, the true ultimate tensile strain used was the one found in the literature [3], and then the nominal value is determined by resorting to Equation 3.2.

$$\epsilon_R = ln(1 + \epsilon_N) \tag{3.2}$$

With equation 3.2, the value for the nominal ultimate tensile strain is 0.07251 mm/mm.

Regarding the Poisson ratio, this value is not given by the norm, hence it will be adopted by the same value used in the literature, which is 0.33 [3, 44].

Table 3.1: Material properties

Density[1] [g/cm^3]	Young's Modulus[1] [MPa]	Poisson Ratio	Yield Strength[1] [MPa]	Yield Strain[1] [mm/mm]	Ultimate Tensile Strength[1] [MPa]	Plastic Strain [mm\mm]	
						Nominal	True[1]
2.68	59000	0.33	211	0.003576	375	0.07251	0.07

[1] Values obtained from the data sheet [42]

As for the manufacturing process, the structures were manufactured through SLM, with the machine SLM Solutions 125HL (Figure 3.1), belonging to the École Nationale Supérieure des Mines d'Albi-Carmaux, in France [3, 44, 45]. The machine has a chamber with 125 mm x 125 mm x 75 mm which uses argon as an inert gas for the process. Moreover, said machine has a single Yb laser with a power of 400 W, a maximum speed of 10 m/s, a width range of 70 μm up to 100 μm and a thickness for the

fusion of singular material layers going from 20 μm to 75 μm. In order to reduce thermal stresses, the building platform was kept at a temperature of 150 ℃. The hatch spacing was 170 μm and the layer thickness was 50 μm. For each fabrication, three samples were made on top of each other. At the end of the process, the samples were separated from the building plate and some samples were grinded with SiC paper to remove traces of supports.

Figure 3.1: SLM Solutions 125HL. Retrieved from [46].

Regarding the heating treatment, the structures were heated up to 270 ℃ for 2h in an oven and then cooled down naturally outside of the oven.

3.2 Choice of structures

This work follows the thesis by B. Coelho [3] and as such one of the main focuses of this work is to compare the structures developed in the aforementioned work against the new gradients. The work by B. Coelho studied the in-plane and out-of-plane mechanical properties of structures with different thicknesses and with several gradients. All the configurations have as basis the structures regular hexagonal, Lotus and Plateau.

In order to choose the adequate structures from said work, the specific stiffness and specific energy absorbed of the structures were compared amongst each other.

3.2.1 Decision criteria and chosen structures

The relative density, specific stiffness and specific energy absorbed of the structures to be chosen are shown in Table 3.2.

For this work, it was decided that the regular structures should be also analysed in this work as act as a baseline for the performance of all gradients. Within gradient 1, it was decided to choose variant 1B, as this one has the highest specific stiffness and specific energy absorbed. Within gradient 2, it was

decided to choose the variants 2C and 2D as these are not the absolute best-performing structures, thence these will provide a counterpoint against the other gradients. For gradient 3, it was decided to choose the structures with the highest specific stiffness and highest specific energy absorbed within all variants, hence it was chosen the variants 3A+, 3B+ and 3C- (Figure 3.2).

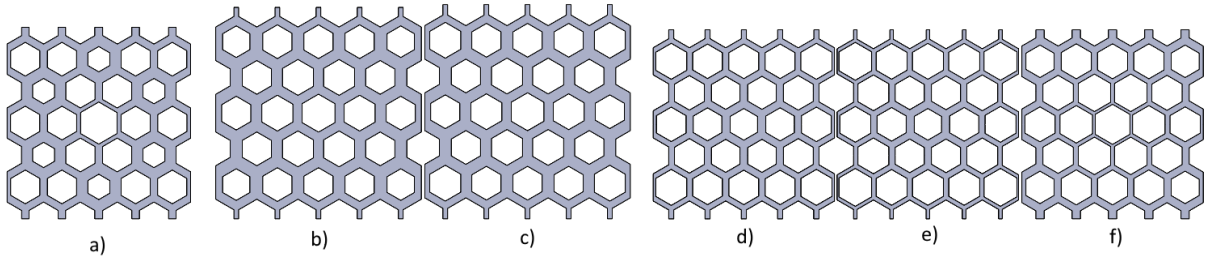

Figure 3.2: Chosen structures [Caption: a) 1B, b) 2C, c) 2D, d) 3A+, e) 3B+, f) 3C-]

Table 3.2: Specific stiffness, specific energy absorbed and relative density of the structures to be chosen. Adapted from [3]

Structure	$\bar{\rho}$	$\bar{K}$	$\bar{E}_a$
L6	0.334	108.6	63.9
L8	0.269	70.7	50.8
L10	0.228	40.1	27.9
1A	0.322	91.2	63.0
1B	0.420	166.9	101.5
2A	0.443	195.1	114.1
2B	0.466	214.0	121.1
2C	0.426	195.1	123.7
2D	0.410	178.9	116.4
3A+	0.323	91.4	85.8
3A-	0.240	57.5	42.3
3B+	0.265	86.3	59.5
3B-	0.298	82.5	55.7
3C+	0.199	49.2	34.0
3C-	0.335	100.3	65.4

3.3 CAD modelling

There are several structures with different variants and configurations that will be studied in this work. A variant refers to a type of gradient, *i.e.* the gradient 4 has the variant 4A, 4B, *etc*; a configuration refers to the type of borders used in the cell, for instance, the structure 4A_Pt is a configuration with lotus borders from the variant A of the gradient 4. Within each variant there are three types of configurations for the

cell borders: *hexagonal*, *hexagonal with Plateau borders*, also referred as Plateau (Pt), and *hexagonal with Lotus borders*, also referred as Lt. The *hexagonal* configuration has a repeating cell with a hexagon, the Plateau configuration has a repeating cell with a hexagon with filleted corners with radius equal to 40% of the length of the inner hexagon (L_1) and the *Lotus* configuration has a circle circumscribed in the hexagon in its cell. In Figure 3.3 an example of all three configurations can be seen.

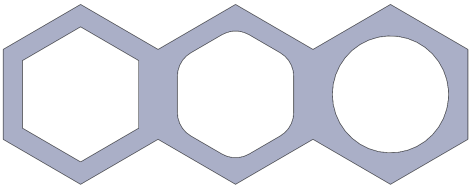

Figure 3.3: Regular hexagon, Plateau borders and Lotus border, from left to right, respectively.

All the honeycombs were designed with the CAD software *SolidWorks 2022* and later on, exported to the software *Siemans NX* for the FEA.

3.3.1 Nomenclature

Throughout this work, a specific nomenclature was used to refer to certain dimensions, below it is provided a list with all the required geometric parameters needed to fully define a structure. Figure 3.4 shows where those dimensions are set. It should be noted that in all of the structures presented in this work, the dimension L_2 is fixed, otherwise, it would not be possible to construct a honeycomb.

- L_1: Length of the inside hexagon;
- L_2: Length of the repeating hexagon;
- e: Wall thickness of the repeating unit;
- t: Wall thickness between two inside hexagons;
- r: Plateau border radius in Plateau border configuration;
- R: Circle radius in Lotus configuration;
- A_T: Total area;
- A_s: Surface area;
- l: length of the structure;
- w: width of the structure;

3.3.2 Relative density equations

In this work, the structures were constructed by one of two methods; by defining the geometrical parameters presented in Section 3.3.1, and then the relative density is calculated, or by imposing a relative

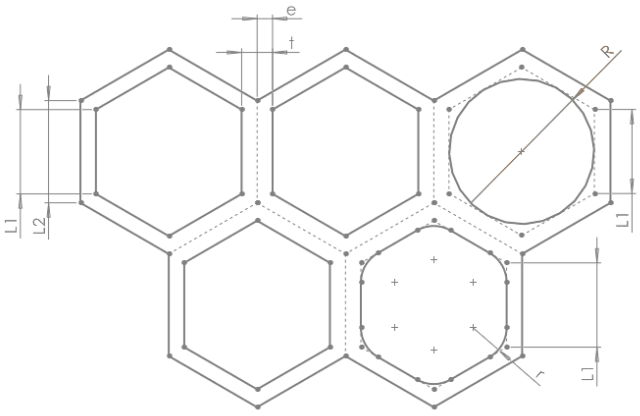

Figure 3.4: Definition of parameters

density and then the geometrical parameters are calculated accordingly. In this section, the calculations for both methods are presented.

Since the structures are based on regular hexagons, it is possible to define all the parameters presented in Section 3.3.1 in terms of L_1 and L_2 and the relative density, therefore it is possible to define the following equations in those terms.

As stated in Section 3.3, the radius of the Plateau borders (r) can be calculated with Equation 3.3.

$$r = 0.4 \times L_1 \tag{3.3}$$

The radius R from the Lotus borders can also be calculated with Equation 3.4

$$R = L_1 cos\left(\frac{\pi}{6}\right) \tag{3.4}$$

The wall thickness of a single cell (e) can be calculated with Equation 3.5.

$$e = \frac{L_2 - L_1}{tan\frac{\pi}{6}} \tag{3.5}$$

The wall thickness of the honeycomb is twice the thickness e, hence t is defined by Equation 3.6.

$$t = 2e \tag{3.6}$$

According to what was stated in Subsection 2.2.2, the relative density of a cellular solid can be calculated with Equation 2.4.

The total area of the solid (A_T) is calculated with Equation 3.7, which is the area of a regular hexagon with side L_2.

$$A_T = \frac{3\sqrt{3}}{2} L_2 \tag{3.7}$$

However, the total area (A_S) depends on the type of border of the structure, hence the equations for the regular hexagons, Plateau borders and Lotus borders are presented Equations 3.8, 3.9 and 3.10.

$$A_{S_{hex}} = \frac{3\sqrt{3}}{2}({L_2}^2 - {L_1}^2) \tag{3.8}$$

$$A_{S_{Pt}} = \frac{3\sqrt{3}}{2}({L_2}^2 - {L_1}^2) + 12\left((0.4L_1)^2\left[\frac{tan(30)}{2} - \frac{\pi}{12}\right]\right) \tag{3.9}$$

$$A_{S_{Lt}} = \frac{3\sqrt{3}}{2}{L_2}^2 - \pi\left(L_1 cos\left(\frac{\pi}{6}\right)\right)^2 \tag{3.10}$$

Combining Equation 2.4 with Equations 3.8, 3.9, 3.10 and 3.7, the following equations can be obtained.

$$\bar{\rho}_{hex} = 1 - \left(\frac{L_1}{L_2}\right)^2 \tag{3.11}$$

$$\bar{\rho}_{Pt} = 1 - \left(\frac{L_1}{L_2}\right)^2\left(1 - \frac{3.84}{3\sqrt{3}}\left(\frac{tan30}{2} - \frac{\pi}{12}\right)\right) \tag{3.12}$$

$$\bar{\rho}_{Lt} = 1 - \left(\frac{L_1}{L_2}\right)^2 \frac{\pi\sqrt{3}}{6} \tag{3.13}$$

These equations are applied whenever it is required to define a structure in terms of L_1 and L_2.

To define a structure with an imposed relative density, it is also required to define the dimension L_2, thus the following equations can be put in terms of the relative density and L_2.

$$L_{1_{hex}} = L_2\sqrt{1 - \bar{\rho}} \tag{3.14}$$

$$L_{1_{Pt}} = L_2\sqrt{\frac{1 - \bar{\rho}}{\frac{3.84}{3\sqrt{3}}\left(\frac{tan30}{2} - \frac{\pi}{12}\right)}} \tag{3.15}$$

$$L_{1_{Lt}} = L_2\sqrt{(1 - \bar{\rho})\frac{6}{\pi\sqrt{3}}} \tag{3.16}$$

It should be noted that despite equations 3.14, 3.16 and 3.15 are said to be only dependent on the relative density, it is necessary that the parameter L_2 to be defined beforehand, otherwise it is not possible to construct a honeycomb, thence all three equations are dependent of the relative density

and on the L_2. It is possible to further work on these equations to obtain an equation which is able to determine the relative density of any kind of configuration which falls within the regular hexagons, hexagons with Plateau borders and Lotus borders. That is because the regular hexagons is a Plateau borders configuration in which the radius of the corners approaches zero, and the Lotus configuration has a radius which is equal to the length L_1. However, to keep this analysis brief and concise this work can be made in future analyses.

As it is possible to construct the configurations in a CAD software without resorting to the equations shown above, a comparison between the results obtained through calculations and through the CAD was made. As the Equations 3.14, 3.15 and 3.16 are obtained with equations 3.11, 3.12 and 3.13, respectively, it is not necessary to validate those. The values chosen for this validation are those from structure 6HPL_-0.05 which will be presented in Section 4.3.

From Table 3.3 it can be seen that the equations are correct and they can be used to define the structures.

Table 3.3: Comparison between the relative density obtained through calculations and through a CAD software.

Configuration	L_2 (imposed)	L_1 (imposed)	$\rho_{calculations}$	ρ_{CAD}
Hexagonal	10	8.06	0.350	0.350
Plateau	10	8.15	0.350	0.349
Lotus	10	8.47	0.350	0.349

3.3.3 Regular structures

These structures were firstly developed by Rua [44], and then used by B. Coelho [3], but only for the regular hexagons. These structures have a base cell which is propagated throughout the whole structure. In order to construct this pattern the dimension L_1, L_2, width, and height must be defined. The values for *r* and *R* must be also defined for the Plateau and Lotus configurations. The thickness of all the regular structures and the gradient structures shown in this work was 12 mm. The parameters regarding the unitary cell and the structure are presented in the Table 3.4.

An example of the configurations of hexagonal, Pt and Lt are presented in Figure 3.5 and Figure 3.6, as well as the structures L6, L8 and L10 to better illustrate the size of all the structures.

3.3.4 Graded structures

Six types of gradients were studied throughout this work. In this section, an explanation of the gradient is given, as well as the geometric parameters of the variations of the gradient and their configurations.

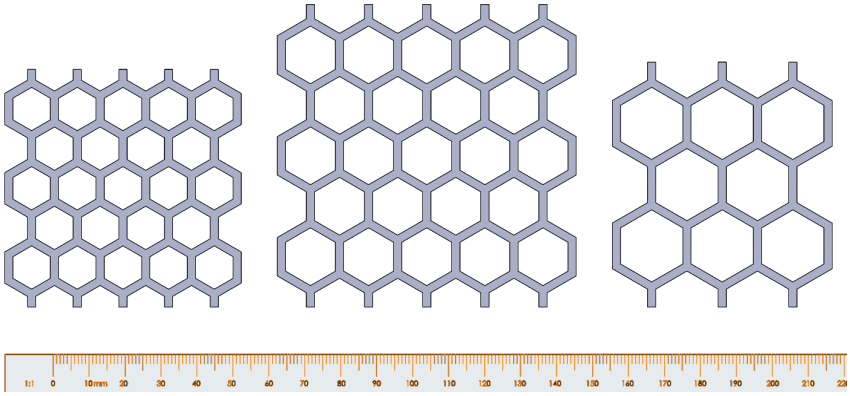

Figure 3.5: Regular structures L6, L8 and L10, from left to right, respectively.

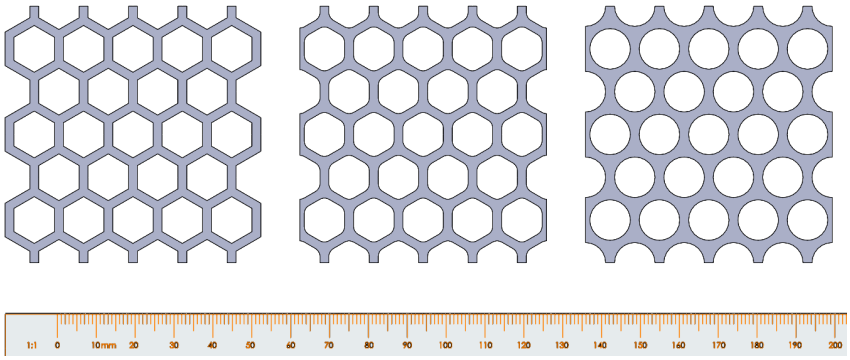

Figure 3.6: Regular structures L6, L6_Pt and L6_Lt, from left to right, respectively.

Table 3.4: Geometric characteristics of the regular honeycombs

Structure	Base cell [mm]				Total Area $[mm^2]$ ([mm] $\times$ [mm])	Solid Area $[mm^2]$	$\bar{\rho}$
	L_1	L_2	r	R			
L6	6	7.33	-	-	4190.690 (65.99 $\times$ 63.50)	1384.77	0.330
L6_Pt			2.4	-		1440.50	0.344
L6_Lt			-	5.20		1646.00	0.393
L8	8	9.33	-	-	7794.23 (84.01 $\times$ 80.84)	1802.95	0.265
L8_Pt			3.2	-		1902.03	0.280
L8_Lt			-	6.93		2267.36	0.334
L10	10	11.33	-	-	7996.21 (87.65 $\times$ 91.22)	3352.30	0.221
L10_Pt			4	-		3445.01	0.237
L10_Lt			-	8.66		3785.24	0.294

Gradient 1: Defined L_1 on certain cells

The gradient 1 is built by defining the L_1 in some cells. The pattern can be explained by looking at Figure 3.7. In the first gradient, the centre cell has an L_1 of 10 mm and the remaining cells have an L_1 of 8 mm. However, the cells whose centres are coincident with the concentric circle will have an L_1 of

6 mm. This variant is denoted as *1B*. The geometrical characteristics of the configurations used with gradient 1 are shown in Table 3.5.

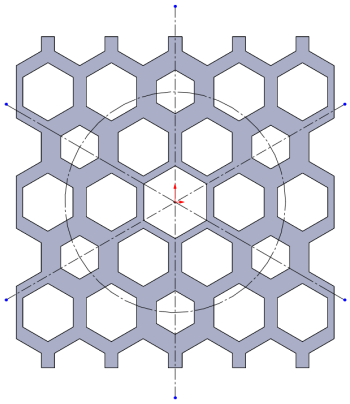

Figure 3.7: Cell arrangement of gradient 1.

Table 3.5: Characteristics of structures with gradient 1.

Structure	Base cell [mm]				Total Area $[mm^2]$ ([mm] $\times$ [mm])	Solid Area $[mm^2]$	$\bar{\rho}$
	L_1	L_2	r	R			
1B	10	10.15	-	-	7996.21 (87.65 $\times$ 91.22)	3352.30	0.419
1B_Pt			4	-		3445.01	0.431
1B_Lt			-	8.66		3785.24	0.473

Gradient 2: Fixed variation of L_1 with different L_1 in the corner cell

For the second gradient, the L_1 of the centre cell is fixed and then the L_1 of the other cells varies according to the cells in its vicinity. The pattern follows what can be seen in Figure 3.8. In said figure, the colour of the cells represents a given L_1, *i.e.* all cells with the colour red have the same L_1.

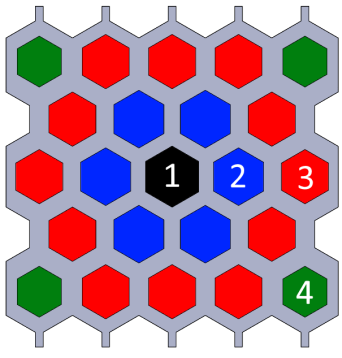

Figure 3.8: Cell arrangement of gradient 2 [Caption: 1 - largest L_1, 3 - smallest L_1; 4 - has an imposed L_1].

The black cell (1) has its L_1 defined, the blue cells (2) has an L_1 equal to the one of the black cell, plus a defined increment, and the red cells are the same as the blue cells but the increment is twice the one given to the blue ones. The green cells have their L_1 defined similarly to what was done with the black cells. The variants used in this work are the *2C* and *2D*. Both patterns have the same L_1 for the centre cell (9mm), the same increment (-0.5mm), but the *2C* pattern has an L_1 for the corner cells of 7.5mm and for the *2D* is 8.5mm. Once again, each variant have the three configurations that were mentioned beforehand and their characteristics are shown in Table 3.6.

Table 3.6: Characteristics of structures with gradient 2.

Structure	Corner Cells L_1 [mm]	Base cell [mm] L_1	L_2	r	R	Total Area $[mm^2]$ ([mm] × [mm])	Solid Area $[mm^2]$	$\bar{\rho}$
2C	7.5	9	11.33	-	-	9880.96 (98.15 × 100.67)	4448.27	0.450
2C_Pt				3.6	-		4558.46	0.461
2C_Lt				-	7.79		4964.69	0.502
2D	8.5			-	-	10011.86 (98.51 × 102.00)	4297.40	0.429
2D_Pt				3.6	-		4407.07	0.440
2D_Lt				-	7.79		4829.42	0.482

Gradient 3: Variation of cell length with R-parameter

The third gradient is a radial gradient where the L_1 of a given cell changes according to its distance to the centre of the structure.

In the structures, it can be drawn several concentric circles where the centre of some cells are coincident with any concentric circle (Figure 3.9). Figure 3.10 has coloured the cells that have the same L_1 for a better understanding of the concept.

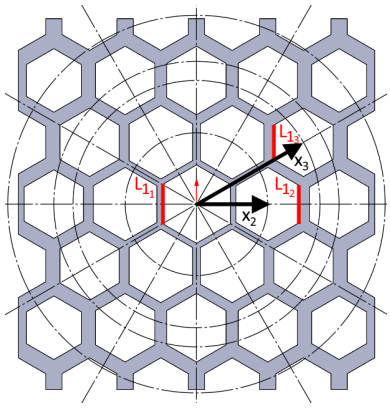

Figure 3.9: Symmetry lines and concentric circles in a structure with gradient 3.

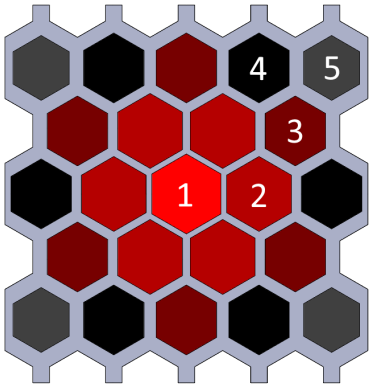

Figure 3.10: Coloured cells with the same L_1. [Caption: 1 - largest L_1, 5 - smallest L_1]

The gradient varies according to the distance of the centre of the repeating unit to the centre of the structure. The distance of a repeating unit's centre to the structure's centre is denoted as x_i and L_{1_i} is the length L_1 of the repeating cell *i* and the variation of L_1 follows Equation 3.17.

$$L_{1_i} = L_{1_1} + R \times x_i \tag{3.17}$$

Where L_{1_1} depends on the initial length given to the centre cell. The rate at which the L_1 changes is defined by the R-parameter [3].

Table 3.7 briefly presents all the characteristics of the structures with gradient 3, including the different configurations that were studied.

Table 3.7: Characteristics of structures with gradient 3.

Structure	R-Parameter	Base cell [mm]				Total Area $[mm^2]$ ([mm] $\times$ [mm])	Solid Area $[mm^2]$	$\bar{\rho}$
		L_1	L_2	r	R			
3A+	0.0217	7.5	10	-	-	7794.23 (86.60 $\times$ 90)	2501.97	0.321
3A+_Pt				3	-		2610.42	0.335
3A+_Lt				-	6.50		2994.68	0.384
3B+	0.0310	7.5		-	-		2083.01	0.267
3B+_Pt				3	-		2195.47	0.282
3B+_Lt				-	6.50		2614.72	0.335
3C-	-0.0371	9.5		-	-		2482.77	0.319
3C-_Pt				3.8	-		2588.27	0.332
3C-_Lt				-	8.23		2977.27	0.382

Gradient 4: Linear gradient along the specimen

Gradient 4 is a structure that uses a linear pattern along the axis of compression. It resorts to Equation 3.17 to define the change of L_1 of each cell along the structure. Hence for these structures, the first line has a set L_1 of 7mm and then the increments will be defined by the equation 3.17 and the R-parameter set.

There will be three variations of the gradient 4 - A, B and C - each one with a different R-parameter. These structures can be seen in Figure 3.11. All of these variations have their corresponding configuration with regular hexagons, hexagons with Plateau borders and Lotus borders (Figure 3.12).

The characteristics of the gradient 4 structures are presented in Table 3.8.

Gradient 5: Three types of configurations in one structure

For the fifth gradient, it was decided to have the regular hexagons, the hexagons with Plateau borders and Lotus configurations within the same sample. It was defined that there would be another type of

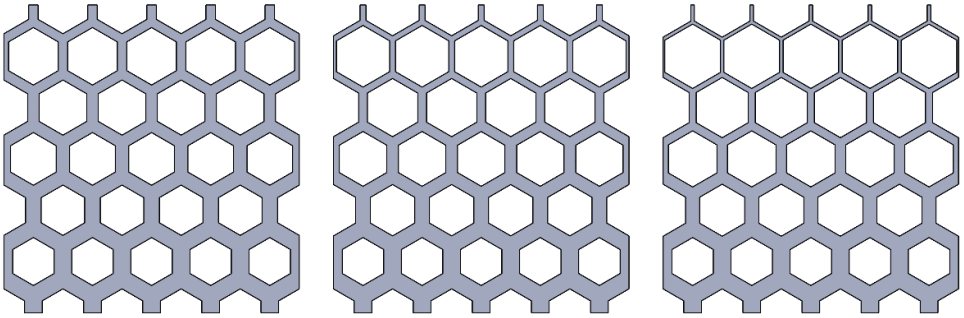

Figure 3.11: Structures 4A, 4B, 4C, from left to right, respectively.

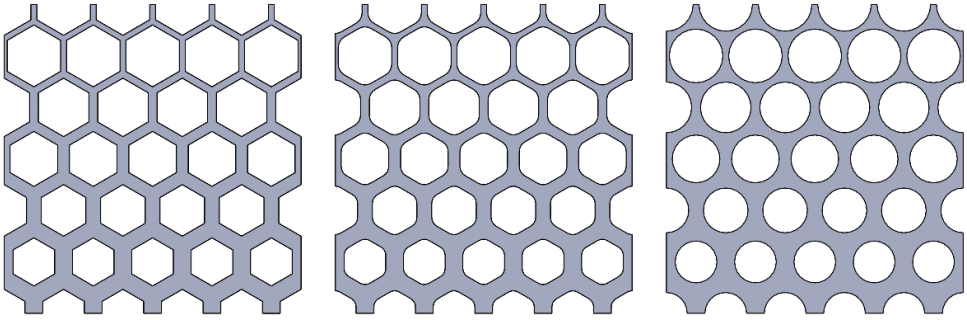

Figure 3.12: Structures 4B, 4B_ Pt, 4B_ Lt, from left to right, respectively.

Table 3.8: Characteristics of structures with gradient 4.

Structure	R-Parameter	Base cell [mm]				Total Area $[mm^2]$ ([mm] $\times$ [mm])	Solid Area $[mm^2]$	$\bar{\rho}$
		L_1	L_2	r	R			
4A	0.0233	7	10	-	-	7794.23 (86.60 $\times$ 90)	3150.75	0.404
4A_Pt				2.8	-		3242.98	0.416
4A_Lt				-	6.06		3583.06	0.460
4B	0.0333			-	-		2760.46	0.354
4B_Pt				2.8	-		2860.43	0.367
4B_Lt				-	6.06		3229.10	0.414
4C	0.0400			-	-		2487.92	0.319
4C_Pt				2.8	-		2593.31	0.333
4C_Lt				-	6.06		2981.94	0.383

repeating unit, a macro repeating unit. The macro repeating unit is made up of repeating units of the same configuration - *i.e.* a macro repeating unit may only have Lotus repeating units, or any other type of configuration, as it can be seen in Figure 3.13.

In order to keep the structure similar to the structures that were presented so far, it was defined that each macro repeating unit has two rows of repeating units whilst keeping the same width as previous structures (Figure 3.13). Furthermore, the relative density of each macro repeating unit was set to be equal to 0.35.

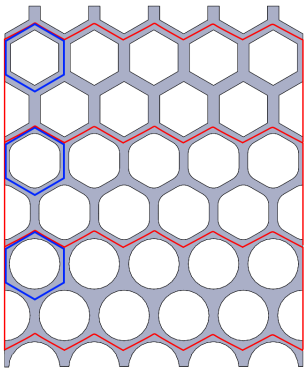

Figure 3.13: Macro repeating units. [Caption: Blue - Repeating unit; Red - Macro]

As there are three types of configurations - regular hexagonal, hexagonal with Plateau borders and Lotus -, three arrangements were chosen: Hexagonal-Plateau-Lotus (HPL), Lotus-Hexagonal-Plateau (LHP) and Plateau-Lotus-Hexagonal (PLH) (Figure 3.14).

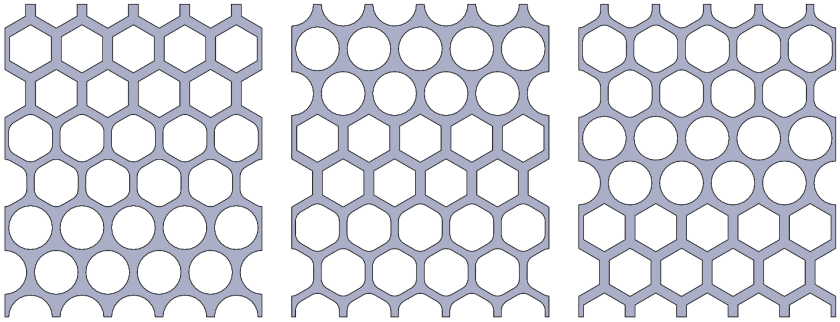

Figure 3.14: Structures 5HPL, 5LHP and 5PLH, from left to right, respectively.

These structures use a notation, where ”H” will stand for regular hexagonal, ”P” for Plateau and ”L” for Lotus. Hence the structure 5HPL is the structure with the fifth gradient and has a regular hexagonal macro repeating unit on top, a Plateau in the middle and a Lotus at the bottom. Their characteristics can be seen in Table 3.9.

Table 3.9: Characteristics of structures with gradient 5.

Structure	Base cell [mm]				Ttotal Area $[mm^2]$	Solid Area $[mm^2]$	$\bar{\rho}$
	L_1	L_2	r	R	([mm] $\times$ [mm])		
5HPL	H=8.06				9093.27	3033.38	0.334
5LHP	Pt=8.51	10	3.4	7.34		2996.03	0.329
5PLH	Lt=8.47				(86.60 $\times$ 105)	2996.67	0.329

Gradient 6: Linear gradient along the specimen

The sixth and final gradient follows the same pattern as the fifth one however, instead of fixing the relative density of the macro repeating units, their relative density varied linearly.

In order to study the effect of this change, this variation in the relative density was applied to the structure 5HPL. It was set that the macro repeating unit would have a relative density of 0.35, the Plateau would have 0.3 and the Lotus would have 0.25. It was decided this way, as the Lotus configuration has a higher relative density than the Plateau configuration which in turn has a higher relative density than the regular hexagons. The variation of 0.05 of the relative density was chosen so that each macro repeating unit would not become isolated pores or that the cell wall would become thin enough to not sustain higher loads. For this gradient, the nomenclature for the structures was the number of the gradient, followed by the letters of the arrangement and then the numbers of the relative density of each macro repeating unit. So the gradient "6HPL_-0.05" was the one that was described previously. The structure can be seen in Figure 3.15 and its characteristics are in Table 3.10.

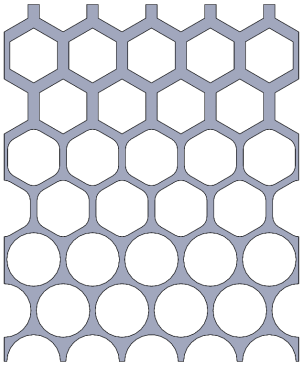

Figure 3.15: Structures 6HPL_-0.05

Table 3.10: Characteristics of structures with gradient 6.

Structure	Base cell [mm]				Total Area $[mm^2]$	Solid Area $[mm^2]$	$\bar{\rho}$
	L_1	L_2	r	R	([mm] $\times$ [mm])		
	H=8.06				9093.27		
6HPL_-0.05	Pt=8.83	10	3.5	7.87		2564.41	0.282
	Lt=9.09				(86.60 $\times$ 105)		

3.4 Numerical

It is essential to have an accurate simulation of the compression tests so that the results obtained correspond to reality. The numerical simulations present results for the perfect case, and as there are

always imperfections in the real world it is expected that the analysis would always be an overestimation of the experimental results. In order to predict the stresses and displacements along the structures and some other mechanical parameters, finite element method software was used. In this work, the software chosen was the *Simcenter Nastran* from Siemens NX (NX). All of the FEA presented in this work were made on an Asus TUF Dash F15 laptop, with an i7-12650H Central Processing Unit (CPU) and 16GB of Random Access Memory (RAM).

3.4.1 Numerical simulation files

The software Simcenter Nastran requires 3 files to perform the analysis. Those are the *.part* which include the CAD of the part, the *.fem* in which the mesh and material assignment was done and the *.sim* where the boundary conditions are set. The simulation is ran and the post-processing of the simulation is made. In this topic, it is explained what is required in each file.

Part file

In the *.part* file, it is necessary to either create the CAD part or import the *.step* file from a previously made geometry. For this work, the geometry was drawn in SolidWorks 2022 and subsequently imported to NX as *.step* file. In NX, the required part is imported and then two rectangular blocks are added to simulate the compression plates and finally, the whole CAD is split in four through its symmetry planes, as shown in Figure 3.16.

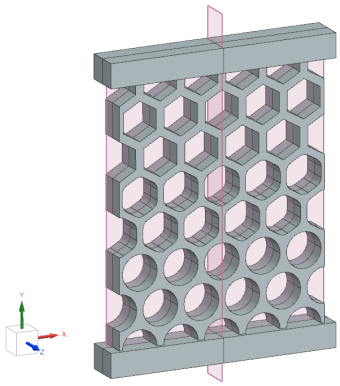

Figure 3.16: *NX .part* file. [Note: The pink planes are aligned with the X-Y plane and the Y-Z plane.]

The ”plates” were made with a sketch and then extruded with the command *Extrude* and the geometries were split using the command *Split Body* and using the plane in pink in Figure 3.16. It is crucial to split the bodies in such a way as this simulates the preload given to the part and without it, the simulation could not provide accurate results.

Fem file

In the *.fem* file, the mesh mating was done, as well as the mesh of the geometries and lastly the material assignment. Firstly, it is needed to make the *Mesh Mating*. This command allows the split bodies to have coincident nodes between parts of the bodies and the coincident nodes will always stay together. This command is needed since the bodies in the simulation was divided into four parts each, then upon making the mesh, it is necessary that the nodes on the coincident faces are superposed. Thus the *mesh mating* option binds the superposed nodes from each part. Therefore, the four parts of each body must be selected and then select OK in the *Mesh Mating* window (Figure 3.17). After doing the mesh mating on both compression plates and the specimen, the mesh has to be created. For so, the *3D Swept Mesh* window is opened (Figure 3.18), and the type of element is chosen, for this work the type of element chosen was the CHEXA8. Then it is set the mesh size and a ”mesh collector” is created. The mesh size used was 1.1 mm and in Section 3.4.2 this choice is explained.

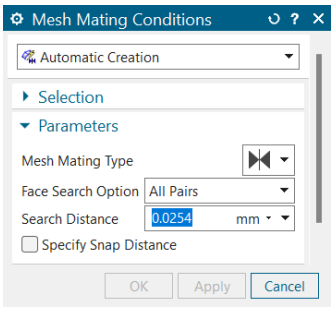

Figure 3.17: *Mesh Mating* window.

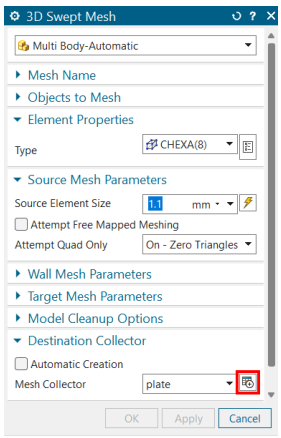

Figure 3.18: *3D Swept Mesh* window.

To create a new mesh collector, the button with a red box in Figure 3.18 must be pressed and then the window shown in Figure 3.19 is open. Then, the button with a red box around it in Figure 3.19 must be pressed to assign a new material. Following these commands, the material list (Figure 3.20) will be opened. In order to create the material of the specimen, the button with a red box in Figure 3.20 must be pressed.

Afterwards, the window in Figure 3.21 is opened and it is necessary to input the material density, Young Modulus, Poisson coefficient and the material engineering curve. For the latter, selecting the option highlighted by the red box is required and selecting ”Elastoplastic: Stress-strain total strain” is required. This last option is required since the simulation must include the plastic deformation of the specimen. For the engineering curve of the material, the button highlighted with a red circle in Figure 3.21 must be selected, followed by the option ”Table” to insert said properties. On the newly opened window which will be the one in Figure 3.22, in the highlighted red box, the option ”Strain” must be

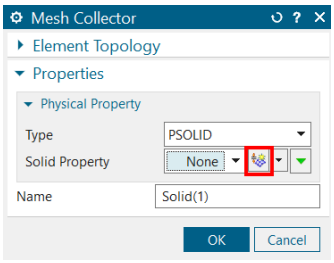

Figure 3.19: Mesh collector window.

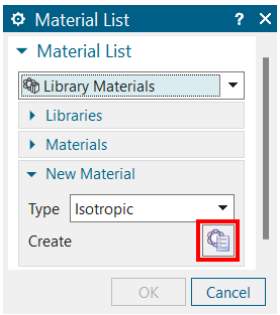

Figure 3.20: Material list.

chosen.

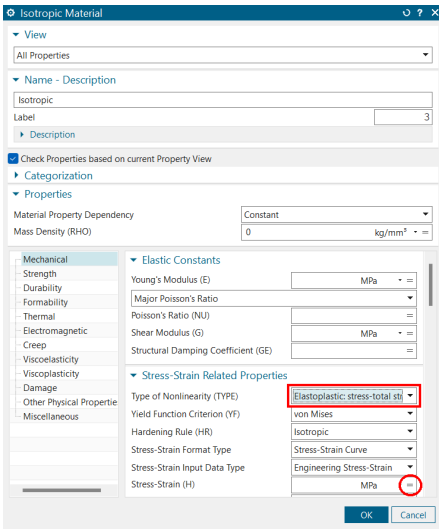

Figure 3.21: Material properties.

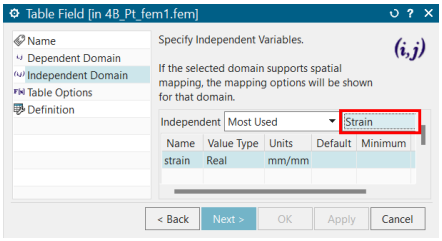

Figure 3.22: Table field of the engineering curve.

Afterwards, upon selecting the ”Definition” folder on the left menu, the values for the engineering curve can be put as seen in Figure 3.23. With this, the mesh and material of the specimen were fully defined.

For the compression plates, the procedure was the same up to the step where a new material was created. On the ”Material list”, one must select the option to see the materials in the NX library (Figure 3.24) and choose the appropriate material. In this thesis, the material chosen for the plate was the *AISI_Steel_Maraging* from the *Simcenter Nastran* library, as this material has a Young Modulus much higher than the one of AlSi7Mg0.6. This is important to ensure that the compression plates do not deform, and thus do not absorb any energy from the compression, this way the energy absorption would be solely made by the specimen compressed.

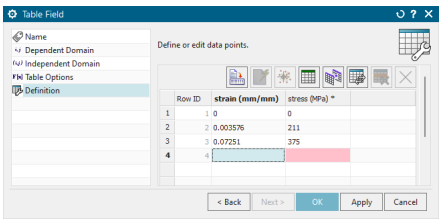

Figure 3.23: Engineering curve definition.

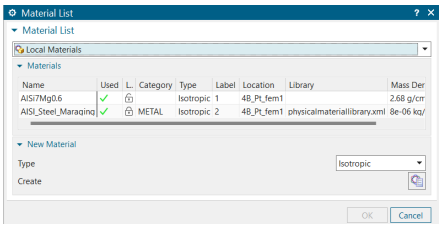

Figure 3.24: Material list from NX.

Sim file

The *.sim* file is the one where the boundary conditions are set, the simulation parameters are set according to what was found in Section 3.4.2 and in 3.4.3. Upon finishing the steps detailed in the previous subsection, a *.sim* file was created which was based on the *.fem* file previously made.

Firstly it is needed to set the solver which was used. For this thesis, the solver used was the *SOL401 Multi-Step Linear* (Figure 3.25) as this one simulates the elastic and plastic compression of a specimen. Afterwards, it is necessary to define the output of the simulation and some other parameters for the simulation to provide accurate results.

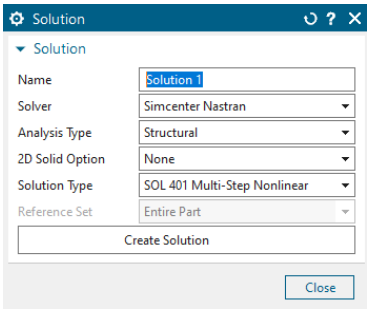

Figure 3.25: Solver selection

After defining the parameters of the solver, the contact regions of the simulation are set. Those are the top and bottom surfaces of the compression plates, denoted ”top” and ”bottom” in the simulation, respectively. The top and bottom of the specimen were denoted ”top hc” and ”bottom hc” in the simulation, respectively. Those regions can be seen in Figure 3.26 and Figure 3.27 highlighted in red.

All of the regions have to be defined as surface type ”FLEX” as the solver SOL401 does not allow for regions to be defined as perfectly rigid (Figure 3.28).

After selecting the regions it is mandatory to define the type of contact between the plates. For such, the option *Surface-to-surface contact* is chosen as it simulates the sliding between the specimen and the plate and it allows the user to set the friction coefficient desired. Hence, in the window in Figure 3.29 a pair of surfaces in contact have to be chosen - for instance, the surface ”top” and ”top hc” - and then the friction coefficient is defined in the appropriate box. For this thesis, the friction coefficient used in all

Figure 3.26: Region selected of the plates [Caption: 1 - top; 2 - bottom]

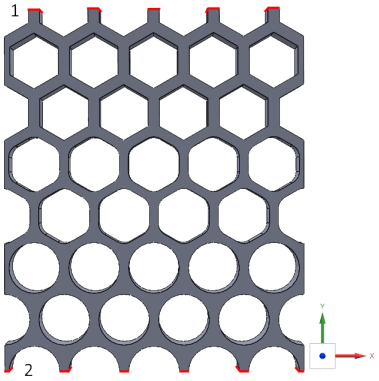

Figure 3.27: Region selected of the honeycombs [Caption: 1 - top hc; 2 - bottom hc]

simulations was 0.2, as a sheet of Teflon was placed between the plate and the specimen to decrease the coefficient of friction and to avoid damaging the surface of the compression plates.

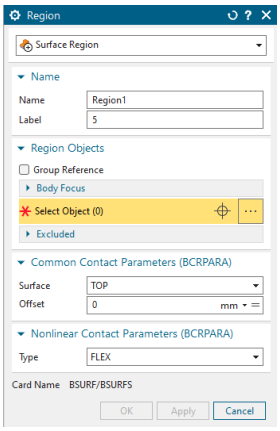

Figure 3.28: Region definition.

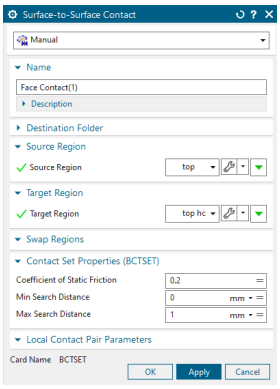

Figure 3.29: Contact type between surfaces.

In the experiment, there was a preload acting upon the specimens to avoid them to slide at the beginning of the compression. Such preload was simulated in the Finite Element Method (FEM) software with a restriction in two degrees of freedom of the specimen, those being the translation axes in which the specimen will not be compressed. For these simulations, it was defined that the compression axis - the axis in which the specimen will be compressed - would be the y-axis. In the window shown in Figure 3.30, one must choose the correct face to be constrained and the edge to be excluded to work as intended. As a representative example of this constraint, in Figure 3.31, the constraint was applied for the z-axis and the face selected is the one highlighted in red and the edge that must be excluded in the blue one. The excluded edge must always be the one in the centre of the specimen.

Another constraint which is required for the simulation is the one regarding the movement of the upper plate. For this work, it was defined that in the simulation the upper plate would have a displacement

of 4mm. Hence, when applying such constraint, it is necessary to open the *Enforced displacement constraint* window, select the top surface of the top plate and then, on the *DOF2*, which is the y-axis, type ”-4” to define the compression displacement (Figure 3.32).

Finally, the last constraint required is the fixed constraint for the bottom plate. To apply this constraint, it is necessary to open the *Fixed Constraint* window and select the bottom faces of the bottom plate in the simulation.

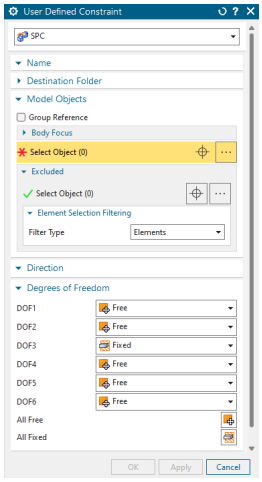

Figure 3.30: *Preload* constraint in the z-axis window.

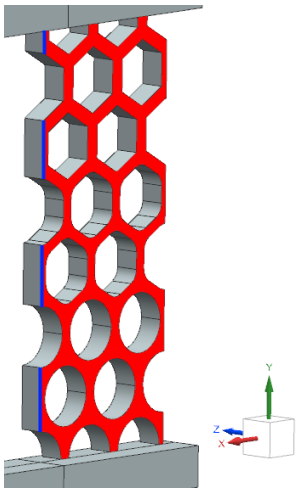

Figure 3.31: Preload constraint. [Caption: Red - Constrained face; Blue - Excluded edge.]

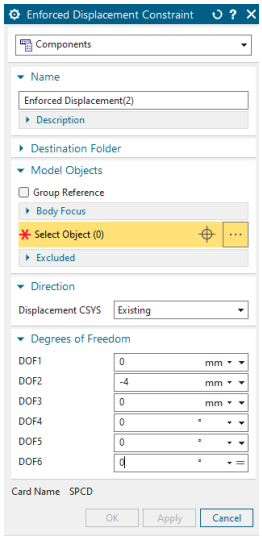

Figure 3.32: Displacement constraint.

Lastly, before starting the simulation it is required to select three boxes from the menu ”Edit solution”. The boxes ”Large Displacements”, ”Large Strains” and ”Material Nonlinearity” shown in Figure 3.33 must be selected in order for the solution to take into account the nonlinearity of the material’s engineering curve. Then, right-clicking in the ”sub-case” box, the editing menu must be opened such that the total time of the compression and the number of increments are indicated (Figure 3.34).

Lastly, what is needed to run the simulation is to click on the button *Solve* and wait for the machine to complete the simulation.

The output of every simulation was a spreadsheet which had the force of every node of the compression plates at any given time step. To obtain the force applied to the structure at a given time step, it was required to sum the force of every node one on compression plate, and then the value is obtained.

3.4.2 Mesh convergence analysis

A FEA can be as precise as one wishes however, an increase in precision will imply an increase in the computation time and an in file size. Therefore it is mandatory to define a set of parameters that allow

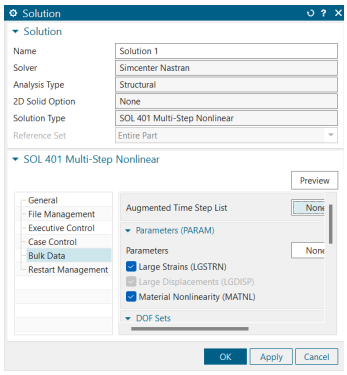

Figure 3.33: Solution ”edit” menu.

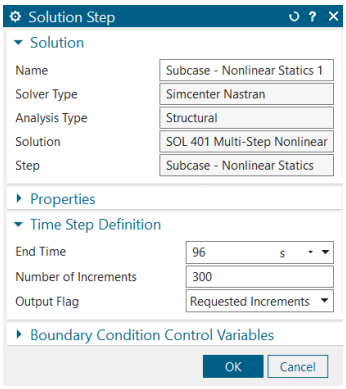

Figure 3.34: Time and increments menu.

the simulation to have a high precision whilst having low computational time [47].

In *Simcenter Nastran*, the two main parameters that determine the precision and the computational time of the simulation are the mesh size and the number of increments.

The mesh size determines the size of an element, which in turn, determines the distance between two connected nodes. The mesh size is defined by a distance which describes the maximum distance between two nodes. Decreasing the mesh size will increase the number of nodes - and the number of elements - in the analysis which in turn, will increase the precision of the simulation, however, the computational time will also increase as well as the file size [48].

For the convergence analysis, ideally one should do a convergence analysis for each structure. However, for the sake of simplicity and due to time constraints, the convergence analysis was made in one structure, and then the results were applied to the remaining structures. The structure used for the convergence analysis was the L6_Lt as it has the fewest stress concentrations. It is important to choose a structure with few stress concentrations, as these often have high stress variations while making the analysis which then may skew the results. In order to understand if there is a convergence in the results, three nodes were selected to assess the convergence (Figure 3.35).

These nodes were chosen as they evaluate the behaviour of the structure on the edge of the repeating unit (node 1), in the middle of the strut (node 2) and in the contact between the structure and the plates (node 3). For each node, its von Mises stress and its displacement was evaluated. The von Mises stress was chosen as it is the main result to look at in an FEA and the displacement of the nodes is also used, since they corroborate the results obtained through the von Mises stress and because the immediate output of an FEA is the displacement of the nodes [48, 49].

To choose an appropriate mesh, one must start with a coarse mesh, and then refine the mesh until an accurate result is obtained whilst maintaining a low computational time. Therefore, the mesh converges when the variation of the results of a given mesh is less than 5% than the results on the previous mesh. With these parameters defined the results obtained for the mesh convergence analysis are shown in

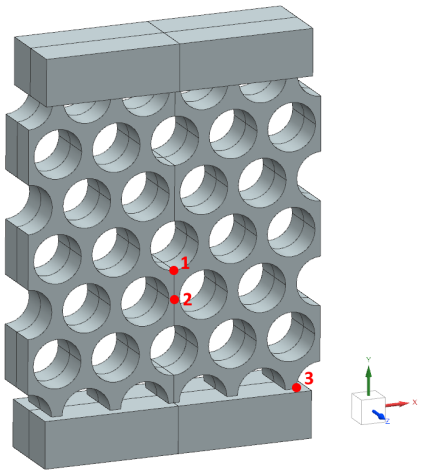

Figure 3.35: Control nodes for the mesh convergence analysis of structure L6_Lt

Table 3.11 and Figure 3.36, shows a graphical representation of the percentual variation

Table 3.11: Mesh convergence analysis values for the von Mises stress. [Note: the green line indicates the chosen mesh size.]

Element size [mm]	Number of elements	Number of nodes	Computing time [s]	von Mises stress [MPa]			Error [%]		
				Node 1	Node 2	Node 3	Node 1	Node 2	Node 3
2.5	2408	4290	259	277.30	252.39	248.72	-	-	-
2	4536	7476	517	389.12	240.8	241.29	40.325	4.592	2.987
1.5	8744	13419	1223	347.32	238.85	246.92	10.742	0.810	2.333
1.3	14010	20383	1774	292.19	232.09	247.92	15.873	2.830	0.405
1.2	15710	22649	2050	297.19	230.25	256.33	1.711	0.793	3.392
1.1	18950	26653	2795	284.1	228.13	255.53	4.405	0.921	0.312
1	27408	37154	3728	269.75	226.73	248.66	5.051	0.614	2.689

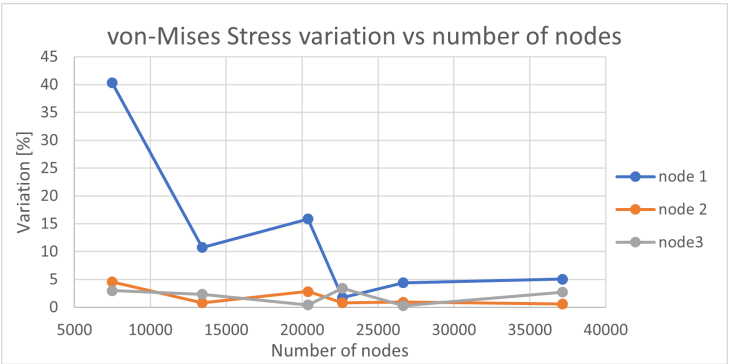

Figure 3.36: von Mises stress percentage variation

As it can be seen, for an element size of 1.2mm, the variation of the von Mises stress is less than 5% however, for an element size of 1.1mm, the variation is also lower than 5% for only an increase of, approximately, 24% of the simulation time. Hence, it was chosen an element size of 1.1mm as the

increase in the computing time was counterbalanced by the increase in the precision of the simulation.

To further assess if the mesh size chosen is appropriate, one may look at the displacement of the selected nodes and, once again, check where the variation is less than 5%. Table 3.12 shows the values for the displacement with their respective variation, and Figure 3.37 shows a graph of that variation.

Table 3.12: Mesh convergence analysis values for the displacement. [Note: the green line indicates the chosen mesh size.]

Element size [mm]	Number of elements	Number of nodes	Computing time [s]	Displacement [mm]			Error [%]		
				Node 1	Node 2	Node 3	Node 1	Node 2	Node 3
2.5	2408	4290	259	0.42	0.43	0.042	-	-	-
2	4536	7476	517	0.43	0.41	0.052	2.123	3.472	23.810
1.5	8744	13419	1223	0.44	0.41	0.082	0.462	0.48	57.692
1.3	14010	20383	1774	0.43	0.41	0.081	0.690	1.193	1.220
1.2	15710	22649	2050	0.43	0.42	0.073	0.463	2.415	9.877
1.1	18950	26653	2795	0.44	0.42	0.07	0.230	0.000	1.370
1	27408	37154	3728	0.43	0.424	0.08	0.230	0.000	1.351

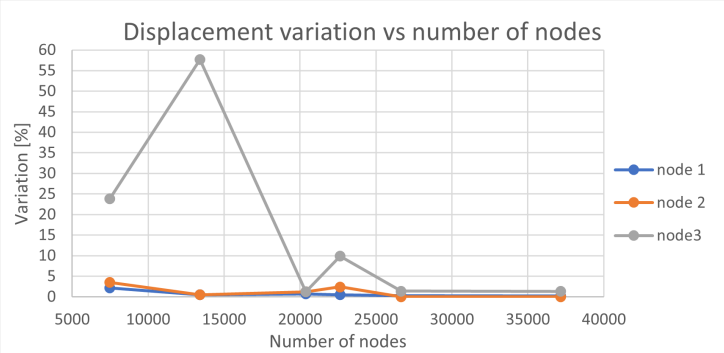

Figure 3.37: Displacement percentage variation

As it can be seen, For a mesh size of 1.1mm, the variation of the displacement on all nodes is less than 5%, hence the choice was an appropriate one.

3.4.3 Increment convergence analysis

The numerical analysis resorts to an implicit analysis and the force-displacement curve, which is obtained with this analysis, is dependent on the number of outputs given by the numerical simulation. The number of points in the curve is controlled by the number of outputs of the simulation, which in turn is controlled by the number of increments. A higher number of increments presents a force-displacement curve with more points, and vice-versa, however, a large number of increments will increase the computational time of the numerical simulation. Since the plastic deformation of the structures was analysed in this work, it is important to choose an appropriate number of increments such that the precision of the

force-displacement curves is appropriate and the computational time is reduced.

Similarly to what was done in Section 3.4.2, the number of increments is defined as ”converged” when the percentage variation of one simulation to the previous is less than 5% on all three nodes. This was assessed for both the von Mises stress and the displacement of the nodes. Table 3.13 and Table 3.14 display the results for this analysis and it should be noted that for 10 increments the result is below the 5% threshold, however, this would later produce force-displacement curves with only 10 points, which consequently, would affect the calculations for the relevant mechanical properties. Hence the three values considered were the 100, 300 and 500 increments.

Table 3.13: Increment convergence analysis values for the von Mises stress. [Note: the green line indicates the chosen number of increments.]

Number of increments	Number of elements	Number of nodes	Computing time [s]	von Mises stress [MPa]			Error [%]		
				Node 1	Node 2	Node 3	Node 1	Node 2	Node 3
5	8744	13419	34	331.07	239.45	257.99	-	-	-
10			63	331.05	239.51	256.60	0.006	0.025	0.539
50			277	331.47	239.05	250.52	0.127	0.192	2.369
100			563	331.51	238.94	248.78	0.0120	0.046	0.695
300			1120	331.52	238.85	246.92	0.003	0.038	0.748
500			2464	331.52	238.85	246.92	0.000	0.000	0.000

Table 3.14: Increment convergence analysis values for the displacement. [Note: the green line indicates the chosen number of increments.]

Number of increments	Number of elements	Number of nodes	Computing time [s]	Displacement [mm]			Error [%]		
				Node 1	Node 2	Node 3	Node 1	Node 2	Node 3
5	8744	13419	34	0.43	0.42	0.06	-	-	-
10			63	0.43	0.42	0.07	0.000	0.240	3.125
50			277	0.43	0.42	0.08	0.231	0.240	16.667
100			563	0.44	0.42	0.08	0.23	0.24	2.597
300			1120	0.44	0.42	0.08	0.000	0.000	3.797
500			2464	0.44	0.42	0.08	0.000	0.000	0.000

From the three options for the number of increments mentioned beforehand, the one which was chosen was the 300 increments, as it has better precision than 100 increments, but it does not increase the computation time enough to justify a lower number.

3.5 Friction coefficient analysis

The friction coefficient is a crucial parameter in the simulations, thus it must be tuned appropriately. This parameter affects the stress distribution of the structures and the deformation, thence a brief analysis of this parameter was made.

In the experimental testing, a sheet of Teflon was placed between the specimen and the compression plates, to ensure the friction coefficient is reduced and that the compression plates was not damaged. Hence, according to what was gathered in the literature [25, 50], a coefficient of 0.2 is the most appropriate starting point for this analysis. In order to assess its accuracy, two other coefficients were analysed: 0.11 and 0.29. For this assessment, the structure L6_Lt was used, under the same assumptions referred to in Section 3.4.2. To determine if the friction coefficient is the most appropriate, the specific stiffness and the specific energy absorbed for a displacement of 1.5mm were used. The stiffness is calculated by determining the slope of the linear region, and the energy absorbed is the area under the force-displacement curve up to a displacement of 1.5mm. To obtain the specific quantities, they were divided by the relative density of the structure.

The data can be seen in Table 3.15, and it can be noted that the discrepancy between the highest friction coefficient and the lowest one is 2.1 % for the specific stiffness and 0.8% for the specific energy absorbed. These discrepancies indicate that the friction coefficient has little influence on the specific stiffness and specific energy absorbed, for the range presented in this work. Thus it would be correct to assume a friction coefficient of 0.2 in the FEA of this work since it has little influence on the parameters evaluated and it maintains a consistency with previous works.

Table 3.15: Specific stiffness and specific energy absorbed for different friction coefficients.

Friction coefficient	$\bar{K}$ [kN/mm]	$\bar{E}_a$ at 1.5 mm [J]
0.11	83.86	44.22
0.2	85.16	44.50
0.29	85.71	44.59

Comparison with a previous thesis

Since in the previous work [3] the numerical analysis was made with the FEM software *Abaqus* and in this work the software Siemens NX is used, it is important to compare the results from one analysis to ensure that the accuracy and precision are maintained such that there is continuity between both works.

The FEA from both this and the previous work have the same boundary conditions, such as the lower plate being a fixed element, the friction coefficient being the same, the upper plate moving with a constant velocity, and the preload being simulated on the specimen. The major differences between both analyses are the cross-head speed of the upper plate which in this work was 2.5 mm/min, the mesh size of the specimen and the number of increments, which depend on the convergence analysis made and the computational power available.

For this comparison, it was chosen to compare the structure L6 under the simulation made for this work. In both simulations, the structure is the same, the preload of the machine is simulated in both

simulations, the compression plates had a Young Modulus several orders of magnitude above one of the materials compressed, the friction coefficient is 0.2 for both simulations and the material properties are the same. The force-displacement curves obtained from the different analyses are shown in Figure 3.38.

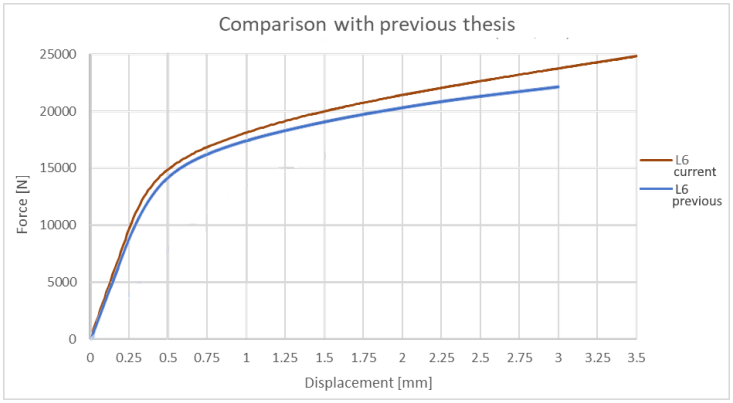

Figure 3.38: Comparison between the results with Abaqus and NX. [Caption: Blue - Abaqus; Brown - NX]

From Figure 3.38, it can be seen that in the linear region, there is a small discrepancy between both curves and in the plastic region this discrepancy is maintained. Still, there is a good matching between both curves which indicates that there is continuity between both works.

3.6 Experimental

The experimental methodology is essential in an investigation since it assesses the accuracy of the numerical analysis and provides insight into whether the numerical analysis might not predict certain effects. Furthermore, it is presented the methodology of the data processing such that the validity of the calculations made can be easily verified by anyone else.

This chapter covers the preparation of the samples, followed by the testing that was made on the specimens, as well as their corresponding standards, and finally looks into the method used for the data analysis.

3.6.1 Sample manufacturing

The samples come with excesses and burrs that need to be removed in order for the samples to be eligible for testing. The burrs were removed in an Iciar-DBA FU 1S milling machine Figure 3.39 with a 70mm face mill, wherein each facing 0.2mm was removed in each passage of the tool (Figure 3.40).

This operation is repeated on both sides of the sample in order to keep the samples as close as possible to each other, and the facing was made until most burrs are removed from the surface and until

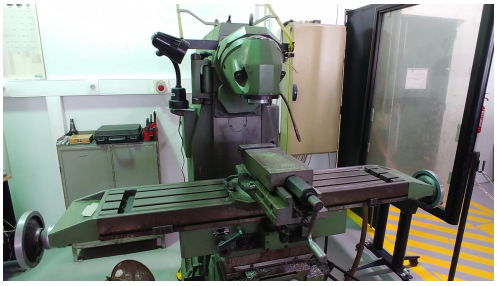

Figure 3.39: Iciar-DBA FU 1S milling machine.

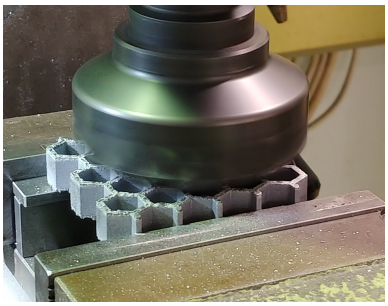

Figure 3.40: Facing operation of one sample.

the specimen has a thickness of 12.0mm with symmetric tolerance of 0.2mm. The before and after the facing operations can be seen in Figure 3.41(a) and Figure 3.41(b)

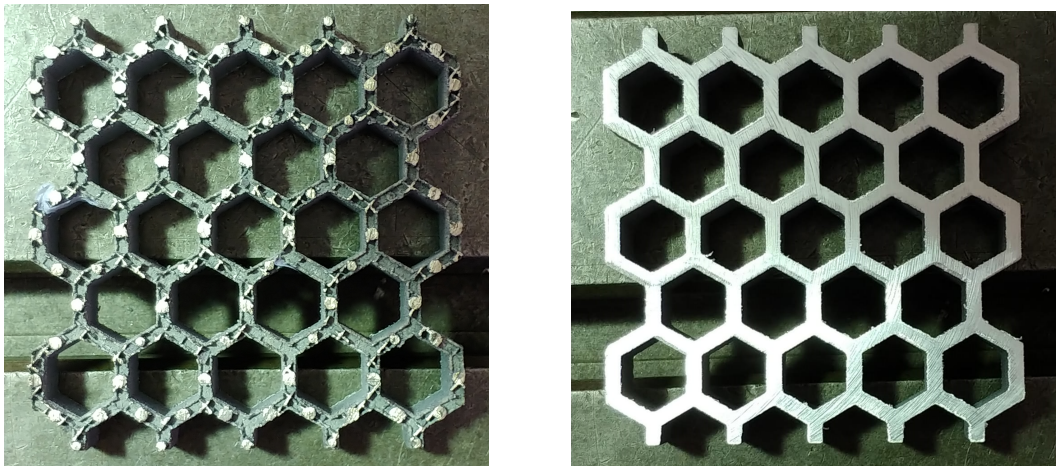

(a) **(b)**

Figure 3.41: Sample before and after the facing operation, from left to right, respectively.

3.6.2 Uniaxial compression testing

The test chosen to evaluate the properties of the structures was a compression test; the standard chosen to follow the guidelines was the ISO 13314:2011 [51] since it is the standard for the mechanical compression of cellular, porous materials. The testing of a specimen was made with a cross-head speed of 2.5mm/min and it will compress the specimens until a fracture occurs, or until the maximum force of the load cell is achieved. Following the standard, three trials were carried out for each variation of the structure, with and without heating treatment. Also, it should be noted that the testing did not achieve the densification of the structure due to the mechanical properties of the material used.

The machine used to perform the compression was an Instron 3369 (Figure 3.42(a)) with a maximum load cell of 50kN and with adequate plates for the compression tests (Figure 3.42(b)). For each sample,

a sheet of Teflon was placed between the plate and the sample to avoid damaging the plates and reducing the friction coefficient.

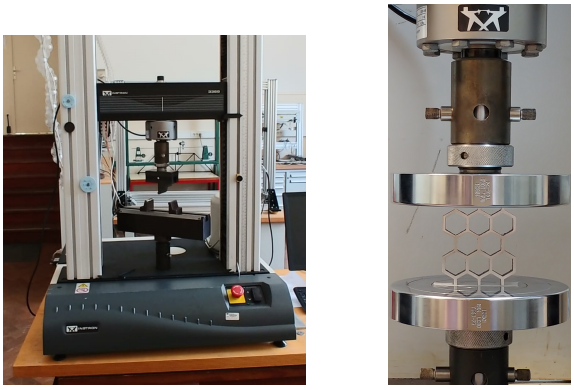

(a) (b)

Figure 3.42: Machine and compression plates. [Caption: (a) Instron 3369 universal mechanical testing machine; (b) Compression plates mounted on the machine.]

3.6.3 Data processing

The *Instron Bluehill Universal* software allows for the user to extract a *.CVS* file after a trial is made, then one can use the data from the exported file in an Excel spreadsheet.

From the spreadsheet, it is obtained the force-displacement curve of the structure. From this curve it is possible to determine the stiffness (K), energy absorbed (E_a) and yield strength (σ_y). The stiffness of the structure is obtained by calculating the slope of the linear region of the force-displacement graph, the slope was calculated by doing a linear interpolation of the points in the elastic zone. However, a major obstacle when calculating the slope with linear interpolation is to define which points should be used in the interpolation. To overcome this obstacle, the coefficient of determination (R^2) of the linear interpolation was used as a criterion to define which set of points should be used [52]. The criteria to choose the set of points for the interpolation were the following: more than 2 points must be chosen and the R^2 of the interpolation must be greater than 0.9999, to ensure the interpolation is precise.

As for the energy absorbed, this quantity will be calculated by determining the area under the curve of the force-displacement graph. For that, the trapezoidal rule [53] was applied between two points, and then the sum of all the parcels until the fracture point shows the energy absorbed.

The yield strength is calculated by dividing the yield force, which is the last point in the elastic region of the force-displacement curve, by the projected area of the structure onto the compression plate.

To obtain the specific values, these must be divided by the relative density of each structure.

4

Results and discussion

Contents

In this chapter covers the numerical and experimental data, together with its discussion and a comparison between the simulations and the experiments. The validity of the numerical results are also assessed.

Under this section, the force-displacement curves were presented, and then a table with the specific stiffness, the specific energy absorbed by the structures, the specific yield strength and the maximum von Mises stress for a given displacement of the structures are also presented. It should be noted that the numerical and experimental values are always presented, except for the maximum von Mises stress, since it is not possible to determine it experimentally. Moreover, the specific energy absorbed was calculated for a displacement of 1.5mm, in order to compare all structures under the same condition. The maximum von Mises stress presented was also for a displacement of 1.5mm for the sake of consistency.

For this analysis, the gradients were divided into 3 categories, regular, radial gradients and linear gradients. The regular ones are the L6, L8 and L10 structures; the radial ones are the gradients 1 to 3; and the linear ones are the gradients 4 to 6. Lastly, a performance analysis of the structures is presented.

4.1 Regular structures

Three variants of the regular structures were studied - L6, L8 and L10 - where all of them had the same thickness of 12mm. Besides these variants, the three configurations for the borders of the cells were also studied - regular hexagons, Plateau and Lotus. It was decided that, in order to assess the validity of the numerical results, the experimental trials were to be made on regular structures and then compared with the numerical results.

Addressing the validity of the numerical simulation it can be seen in Table 4.1 the results as discrepancy between the numerical and experimental results. Also, Figure 4.1 compares the numerical and experimental force-displacement curves. It was decided to compare the specific mechanical properties of the structures to retain coherence throughout the work.

Table 4.1: Numerical and experimental data.

Structure	$\bar{\rho}$	$\bar{K}$ [kN/mm]		$\bar{E}_a$ at 1.5 mm [J]		$\bar{\sigma}_y$ [MPa]	
		Num	Exp	Num	Exp	Num	Exp
L6	0.334	138.91	65.42 $\pm$ 2.77	81.23	55.66 $\pm$ 0.91	44.42	36.08 $\pm$ 5.34
L8	0.269	90.54	55.59 $\pm$ 0.67	65.02	50.48 $\pm$ 0.38	30.13	28.83 $\pm$ 0.26
L10	0.228	50.43	35.02 $\pm$ 0.33	34.91	28.55 $\pm$ 0.21	18.71	24.92 $\pm$ 0.25

Table 4.1 and Figure 4.1, show some discrepancy between the experimental and the numerical data, however, this difference decreases as the relative density decreases and as the dimension L_1

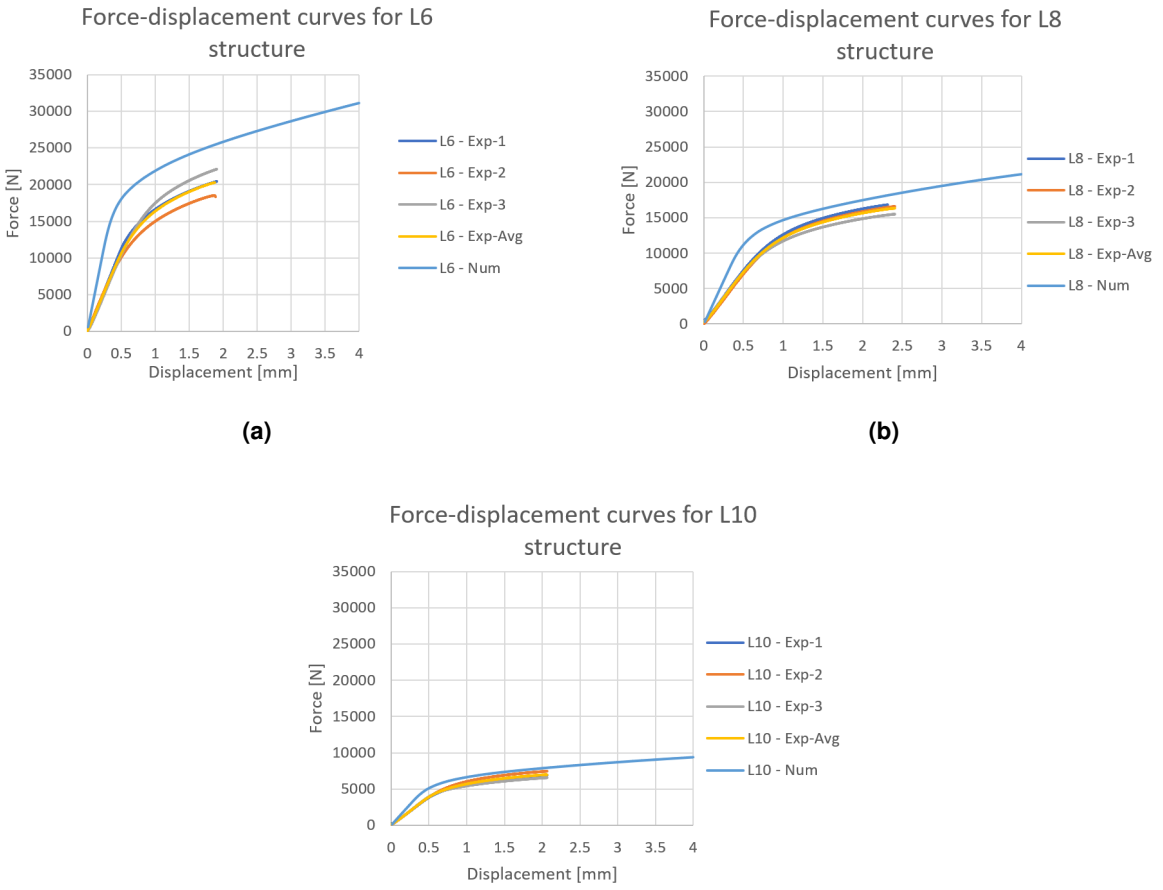

Figure 4.1: Experimental and numerical force-displacement curves for the structures a) L6, b) L8, and c) L10. [Caption: FEM - Numerical results; Exp - Experimental results; Avg - Average.]

increases. Moreover, the numerical force-displacement curves are always above the experimental ones, this is expected as the numerical model assumes the material is homogeneous and isotropic, and the geometrical imperfections of the manufacturing method are not accounted for [54]. Hence the numerical simulation would always be an overestimation of the experimental results. Considering this, the discrepancy between the numerical and experimental analysis may come mainly from the anisotropy and the imperfections of the structure [55, 56]. The anisotropy can be explained by the fact that the SLM process creates pores inside the structure [3] which, at high stresses, could have been the main contributing factor to the appearance of cracks. These inclusions affect the structure's mechanical properties, making the experimental results deviate from the numerical ones. Furthermore, the surface of the structures was very rough, allowing for the appearance of more stress concentrations on the surface, thus easing the appearance and propagation of cracks. According to the literature review, it was possible to conclude that the numerical results were a good approximation of the experimental ones [23, 25, 26, 57, 58].

Still, the discrepancy between both results can be decreased by including defects of the structure in the numerical simulation [56].

Table 4.2: Results of the regular structures.

Structure	$\bar{\rho}$	$\bar{K}$ [kN/mm]		$\bar{E}_a$ at 1.5mm [J]		$\bar{\sigma}_y$ [MPa]		σ_{max} at 1.5mm [MPa]
		Num	Exp	Num	Exp	Num	Exp	
L6	0.334	138.91	65.42	81.23	55.66	44.42	36.08	430.34
L6_Pt	0.344	173.62	-	96.99	-	58.19	-	409.96
L6_Lt	0.393	216.13	-	113.58	-	72.27	-	469.87
L8	0.269	90.54	55.59	65.02	50.48	30.13	28.83	573.15
L8_Pt	0.280	118.80	-	82.85	-	41.02	-	499.59
L8_Lt	0.334	169.41	-	110.59	-	58.36	-	672.07
L10	0.228	50.43	35.02	34.91	28.55	18.71	24.92	579.09
L10_Pt	0.237	68.17	-	45.30	-	27.17	-	565.37
L10_Lt	0.294	107.49	-	64.55	-	42.63	-	644.23

Table 4.2 presents the results of the Numerical (Num) and the Experimental (Exp) data of the given structures. In Table 4.2 there is a clear trend where the Lotus borders have the highest specific stiffness, highest specific energy absorbed and the highest specific yielding stress, and the regular hexagonal borders have the lowest specific stiffness, specific energy absorbed and specific yielding stress. Also, as the relative density increases, so does the specific stiffness, specific energy absorbed and specific yielding stress.

For the sake of simplicity and to keep the explanation concise, it was only covered the stress distributions and the force-displacement graphs of variant L6. The graphs and distributions of the variants L8 and L10 were put in Appendix A.

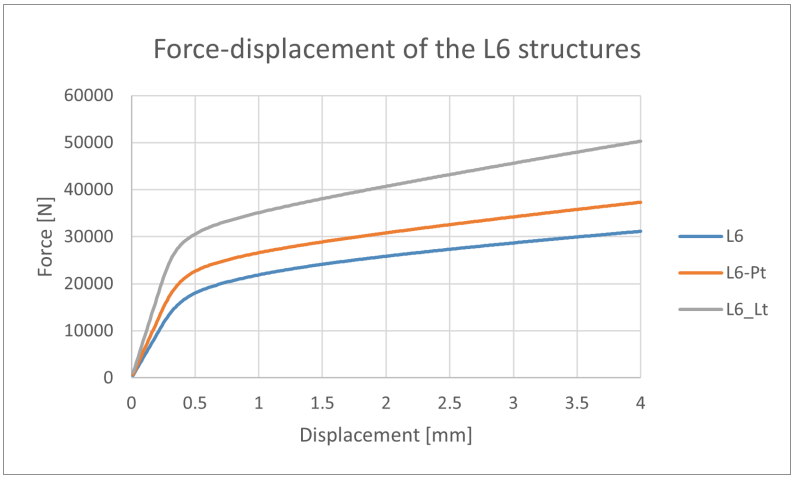

Figure 4.2: Force-displacement numerical curves of the variants of the L6 structure

Figure 4.2 shows that the Lotus configuration increased the specific stiffness by 55.6% when compared to the regular hexagons and the Plateau configuration showed an increase of 25.0%. In the specific energy, the Lotus showed an increase of 39.8%, while the Plateau had an increase of 19.4%. Lastly, the specific yield stress in the Lotus is 62.7% higher than the regular hexagons and the Plateau is 31.0% greater than the regular hexagons. These trends can be seen for the L8 and L10 variations, additionally, as the L_1 increases, the percentage increase of the Lotus and Plateau configuration when compared to the regular hexagons, is further increased. Hence for a given displacement, the Lotus configuration was able to withstand a higher force than the Plateau configuration which in turn was able to withstand a higher force than the regular hexagons configuration. The force-displacement curves of the remaining structures are shown in Appendix A.

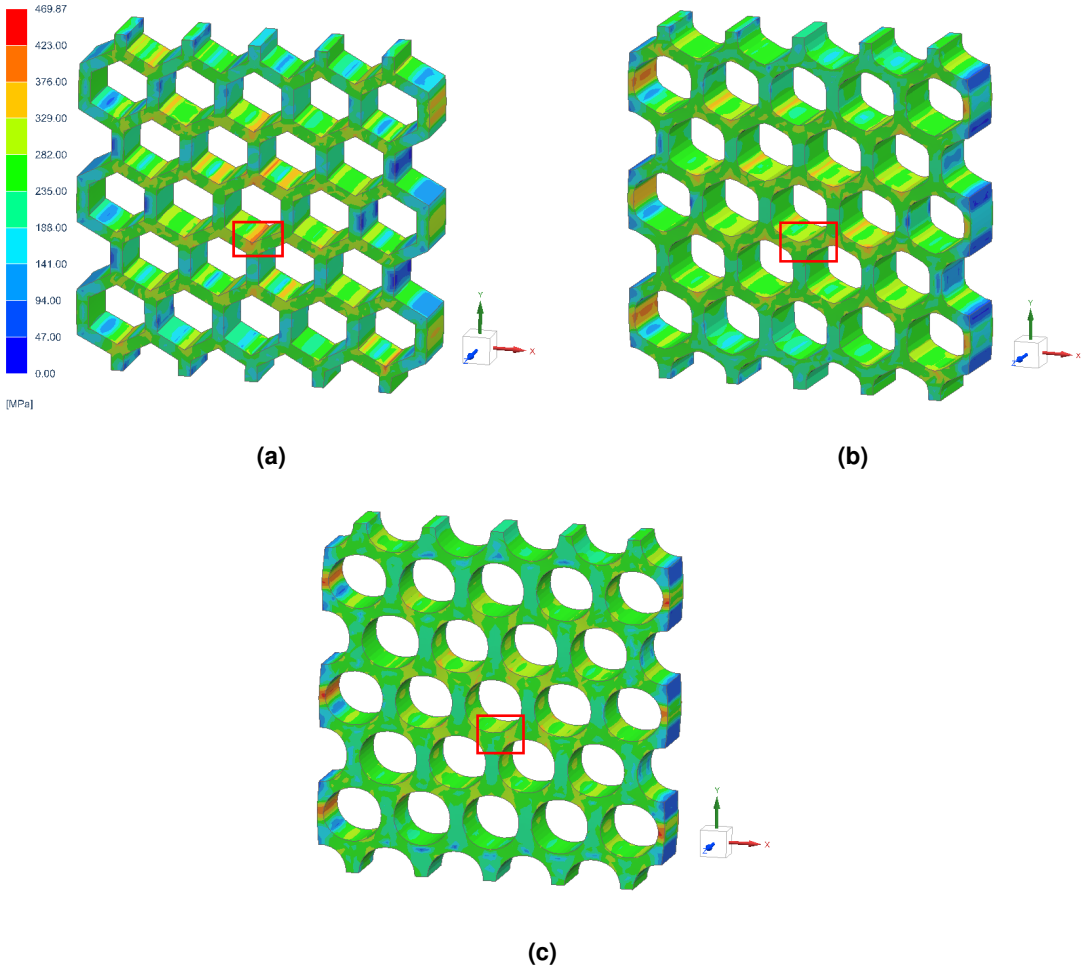

Figure 4.3: von Mises stress of the structures: (a) L6, (b) L6_Pt and (c) L6_Lt, with a red box signalling the triple junction of the cell walls. [Note: all the figures use the scale in Figure 4.3(a).]

Comparing the stress distribution of the three configurations for a displacement of 1.5mm, it is clear that all structures have a homogeneous stress distribution (Figures 4.3(a), 4.3(b) and 4.3(c)). However,

in the junction of three cell walls, the regular hexagons have a higher stress gradient when going across the cell wall, than the Plateau or Lotus configurations (red box in Figures 4.3(a), 4.3(b) and 4.3(c)). When the plastic deformation was achieved, a higher the stress gradient across the cell wall, would make it more prone to fracture. This is effectively seen in the regular hexagon configuration which withstands less force than the Plateau configuration, which in turn withstands less force than the Lotus configuration.

Comparing the structures L6, L8 and L10, the information in Table 4.2 shows that the structure with the highest specific stiffness, specific energy absorbed and specific yield stress was the L6 and the one with the lowest parameters was the L10. The variation L8 showed a decrease of 34.8% in the specific stiffness, 20.0% in the specific energy absorbed and 32.2% in the specific yield stress, when compared to the L6. The structure L10 showed a decrease of 63.7% in the specific stiffness, 57.0% in the specific energy absorbed and 57.9% in the specific yield stress when compared to the L6.

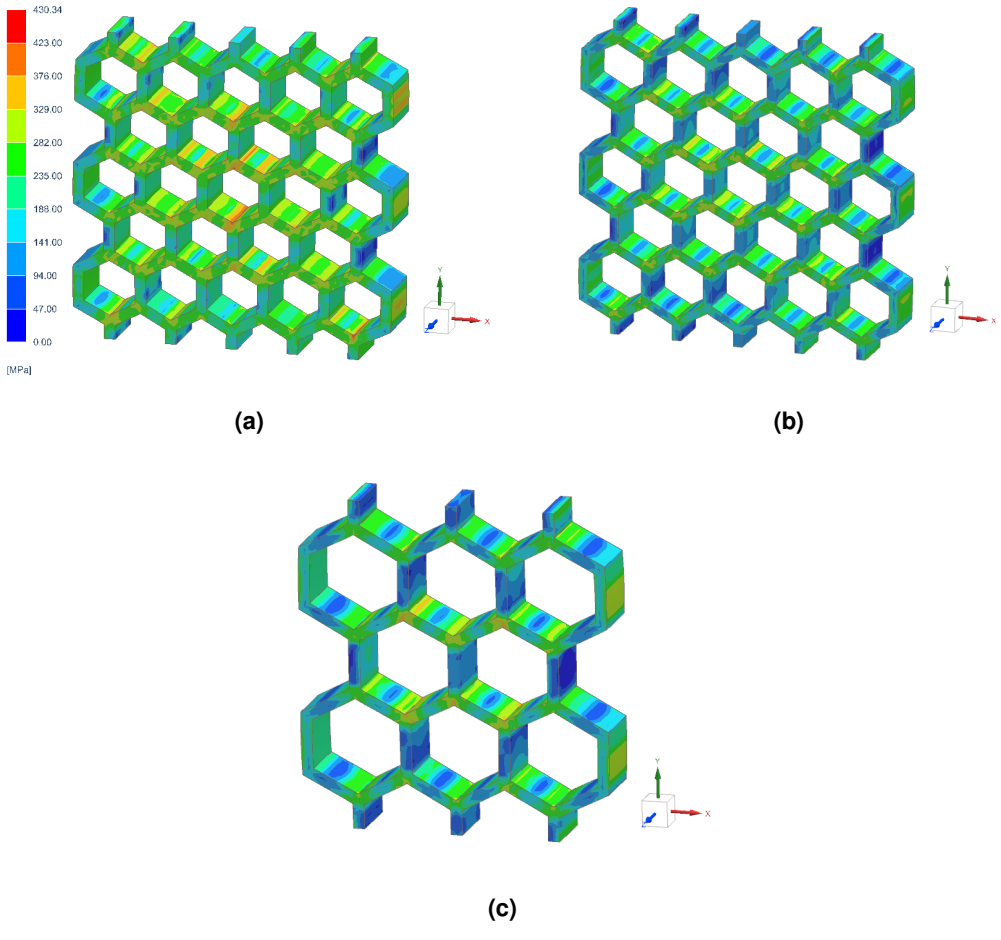

Figure 4.4: von Mises stress of the structures L6, L8 and L10.[Note: all the figures use the scale in Figure 4.4(a)]

The graph in Figure 4.1 shows the force-displacement for these structures. The stress distribution of the three structures (Figure 4.4(a), 4.4(b) and 4.4(c)) shows that the stress distribution is even throughout

the structure and the fracture occurred where three cell walls meet.

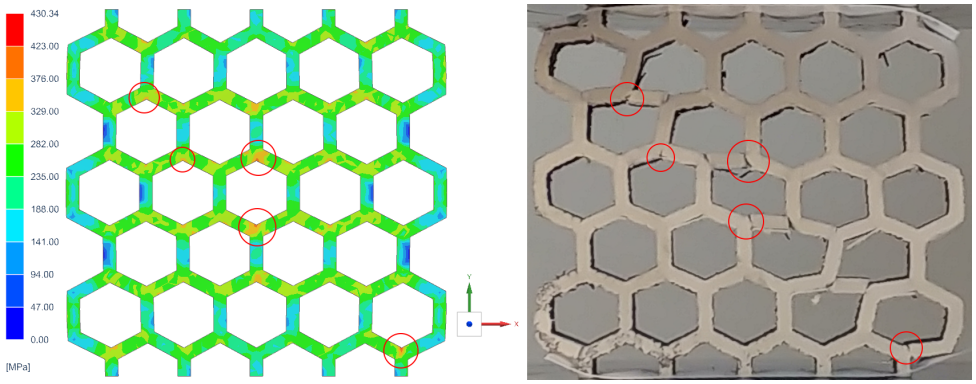

Figure 4.5: Numerical and experimental compression of the L6 specimen with the high-stress regions and fracture points signalled with a red circle, from left to right, respectively.

From the images obtained in the experiments, it can be seen that the numerical simulation predicted accurately where the fracture would occur. For instance, in Figure 4.5 there is a comparison between the stress distribution of the structure and its fracture point during testing. It can be seen that fracture only occurred in points where three cell walls meet, which are the points where the stress was higher according to the FEA. The fracture occurred due to the fact that a crack appeared and then it propagated as the force applied increased.

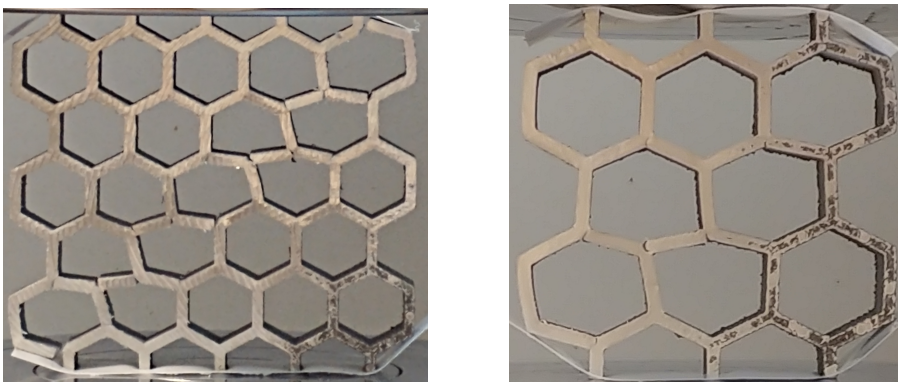

(a) **(b)**

Figure 4.6: Fractured L8 (a) and L10 (b) specimen under an imposed displacement of 4 mm.

The fractured points of specimens L8 and L10 were also predicted by the numerical simulations for the same aforementioned reason. Comparing Figures 4.6(a) and 4.6(b) with Figures 4.4(b) and 4.4(c), respectively, it can be seen that the numerical simulations can predict the fractures that would occur.

It was also studied in this work the influence of heat treatment on the mechanical properties of the structures, namely those that are under the scope of this work: the specific stiffness, the specific energy

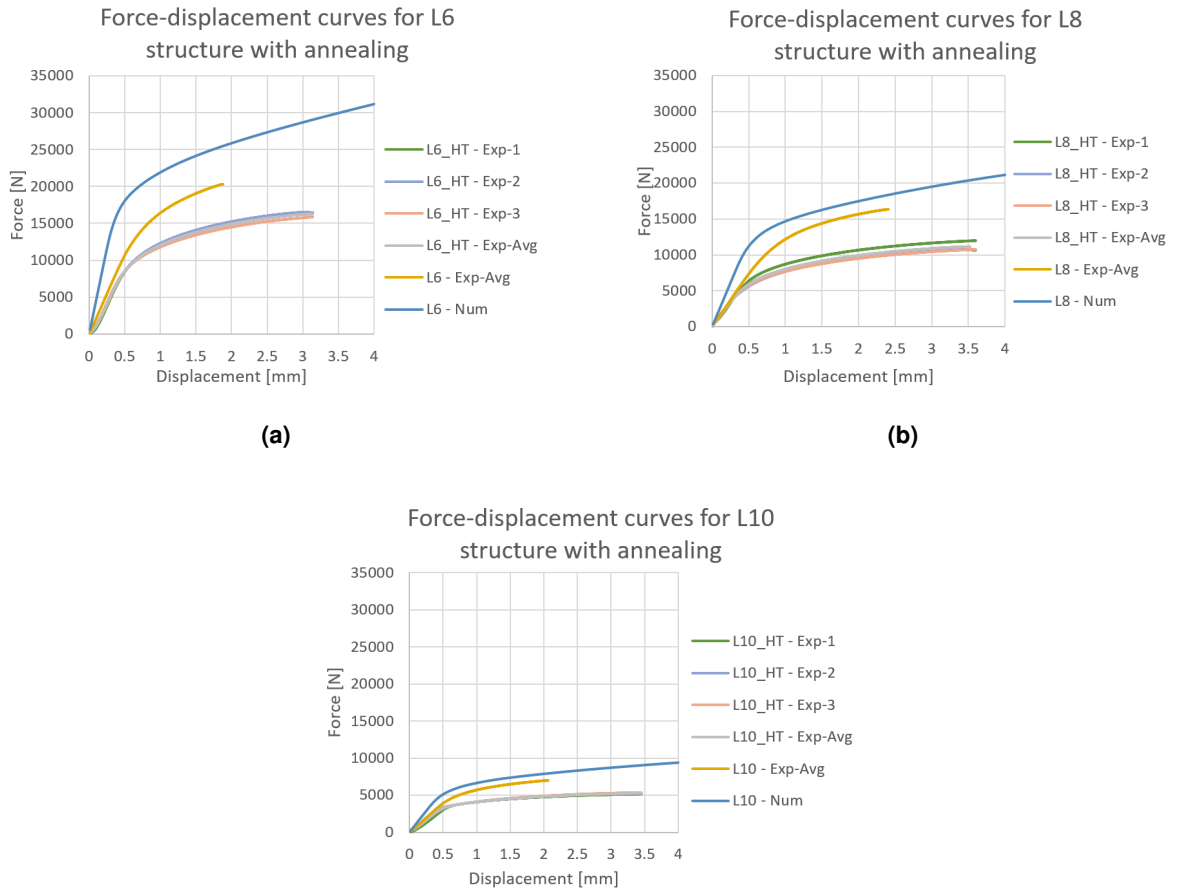

Figure 4.7: Numerical and experimental force-displacement curves with and without heat treatment for the structures a) L6, b) L8, and c) L10. [Caption: FEM - Numerical results; Exp - Experimental results; Avg - Average; HT - Heat treatment.]

absorbed and the specific yield strength.

Three specimens of each structure - L6, L8 and L10 - were subjected to an annealing heat treatment at 270 ℃ for 2h and then they were cooled in open air. The average force-displacement curve of the three trials can be seen in Figure 4.7. From the graph in Figure 4.7 and the data in Table 4.3 it was clear that the annealing had an influence on the mechanical properties of the structures: the specific stiffness and specific yield stress were reduced and the specific energy absorbed before fracture was increased. In other terms, the stiffness was reduced and the ductility was increased. The current FEA model cannot predict the influence of the heat treatment since it would require changing the material properties and for that, it would be needed to do further testing on the material which underwent this particular annealing.

Comparing the mechanical properties of the specimens with and without the heat treatment, Table 4.3 shows the data for the experimental specimens with and without heat treatment. It can be seen

Table 4.3: Experimental results with and without heat treatment.

Structure	$\bar{\rho}$	$\bar{K}$ [kN/mm]		$\bar{E}_a$ at 1.5 mm [J]		$\bar{\sigma}_y$ [MPa]		Energy absorbed before fracture [J]	
		No HT	HT	No HT	HT	No HT	HT	No HT	NT
L6	0.334	65.42 ± 2.77	61.51 ± 1.14	55.66 ± 2.48	41.36 ± 0.49	18.71 ± 5.34	25.87 ± 0.04	25.88 ± 1.42	38.89 ± 0.67
L8	0.269	55.59 ± 0.67	49.24 ± 3.60	50.48 ± 1.15	36.25 ± 1.46	40.81 ± 0.26	15.41 ± 2.46	27.43 ± 0.87	30.52 ± 1.56
L10	0.228	35.02 ± 0.33	31.21 ± 1.30	28.55 ± 0.64	21.31 ± 0.37	16.06 ± 0.26	16.06 ± 1.00	10.72 ± 0.41	16.81 ± 0.22

that the specific stiffness was reduced by around 6% to 13% when compared with the experimental with and without the heating treatment. The specific yield strength was also reduced by between 15% to 25%. Due to these decreases, the specific energy absorbed for a displacement of 1.5mm was decreased between 34% to 39%, but the specific energy absorbed before fracture was increased between 16% to 39%. Thereby confirming that the annealing heat treatment does, in fact, decrease the stiffness of the structure, but increases the ductility.

Lastly, the maximum von Mises stress in the structures, can be seen when comparing the regular hexagon configuration with the Plateau, the maximum stress is reduced in the Plateau configuration due to the rounded hexagons edges which reduce the stress concentrations, as it can be seen in Figure 4.3(a) and 4.3(b). However, the Lotus configuration has a higher maximum von Mises stress than the regular hexagons configuration (Table 4.2) and that is due to the cell walls on the sides of the structure which are thinner than the inner cell walls as these repeating units do not have another repeating unit to double the cell wall thickness. Even so, the inner cell walls have a lower stress than the other configurations whilst sustaining a higher force. The stress distributions of the remaining structures are shown in Appendix A.

A final remark regarding the deformation of the specimens. All of the specimens that were compressed in the experiment had a ”localised deformation mode” which falls within the ones shown in Section 2.2.3. In Figure 4.8 it was drawn a white line in the localised deformations of the specimens, and it can be seen that the deformations were either tilted I-shaped or V-shaped. These deformation modes could also be seen in the heat-treated experimental specimens (Figure 4.9).

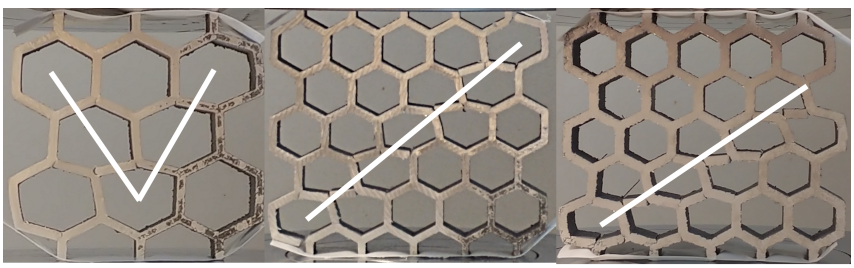

Figure 4.8: Localized deformation modes in the specimens with a white line indicating the deformation mode. [Caption: from left to right, L10, L8 and L6]

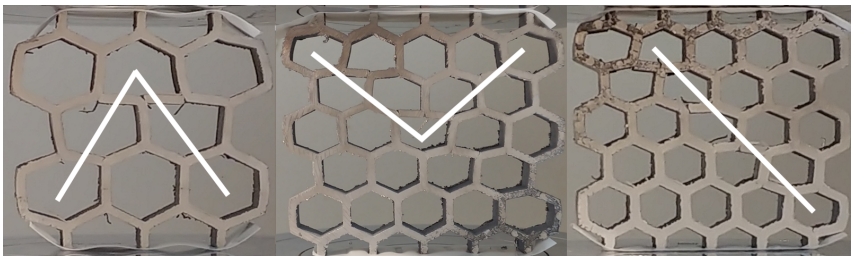

Figure 4.9: Localized deformation modes in the specimens with heat treatment with a white line indicating the deformation mode. [Caption: from left to right, L10_HT, L8_HT and L6_HT]

4.2 Radial gradient structures

Following the regular structures, this section covers the structures with a radial gradient which are the gradients 1, 2 and 3.

As it was seen with the regular structures when looking at the results of the several configurations within one variant, there was a trend with the variation of the specific stiffness, specific energy absorbed and specific yield stress: the Lotus configuration has the highest specific stiffness, specific energy absorbed and specific yield stress and the regular hexagons has the lowest values. The results are shown in Table 4.4.

Table 4.4: Results for the gradients 1, 2 and 3.

Structure	$\bar{\rho}$	$\bar{K}$ [kN/mm]	$\bar{E}_a$ at 1.5mm [J]	$\bar{\sigma}_y$ [MPa]	σ_{max} at 1.5mm [MPa]
1B	0.419	162.13	99.70	40.81	418.56
1B_Pt	0.431	194.58	115.17	48.99	454.72
1B_Lt	0.473	241.00	137.36	60.64	427.81
2C	0.450	199.73	127.66	36.02	519.55
2C_Pt	0.461	229.01	143.30	41.34	534.19
2C_Lt	0.502	270.65	167.23	48.91	513.04
2D	0.429	181.10	117.81	42.80	443.03
2D_Pt	0.440	210.04	133.07	49.63	451.43
2D_Lt	0.482	251.53	156.04	49.07	496.01
3A+	0.321	122.81	86.67	39.11	403.83
3A+_Pt	0.335	155.78	106.74	49.63	414.68
3A+_Lt	0.384	202.63	131.25	64.56	451.82
3B+	0.267	86.86	59.72	24.38	425.46
3B+_Pt	0.282	117.09	77.61	32.83	442.18
3B+_Lt	0.335	166.38	106.45	46.69	406.84
3C-	0.319	102.00	65.89	24.77	473.74
3C-_Pt	0.332	131.78	81.85	32.00	550.46
3C-_Lt	0.382	184.17	109.59	44.68	532.34

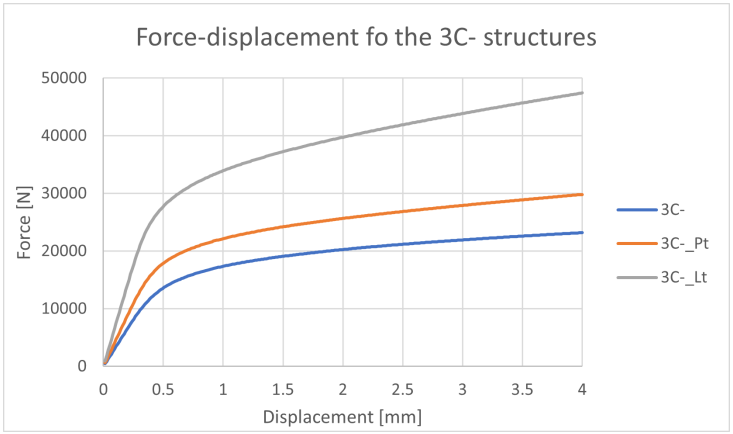

Figure 4.10: Force-displacement graph for the structures with gradient 3C-

For this analysis, was used the variation ”C-” from gradient 3 in order to keep this analysis concise. From Table 4.4, it can be seen that the configuration with the Lotus borders has the highest specific mechanical properties, while the regular hexagons have the lowest ones when comparing the configuration within a variant. Within variant 3C-, the Lotus configuration has a specific stiffness 80.6% greater than its regular hexagon counterpart. Also, the specific energy absorbed and the specific yield strength are 66.3% and 80.3% greater than the regular hexagon configuration. These differences are better illustrated in the force-displacement graph in Figure 4.10

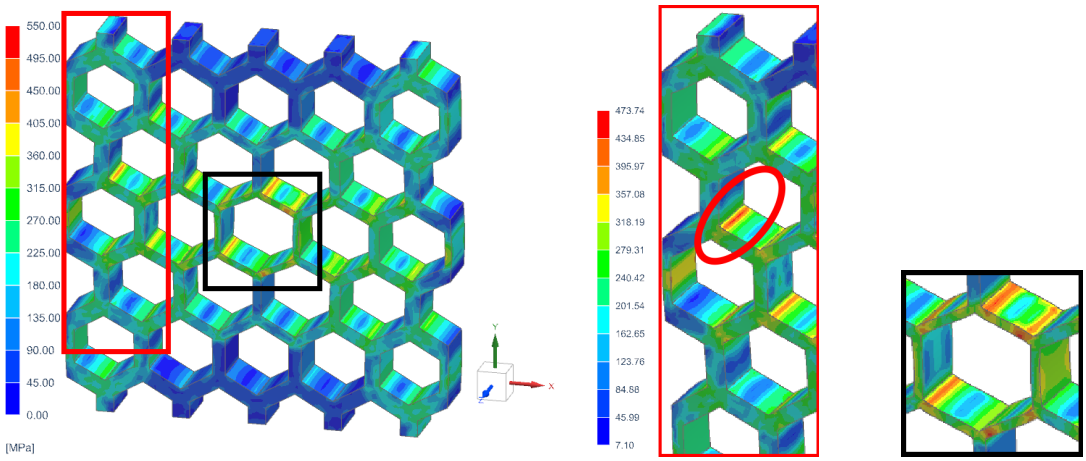

Figure 4.11: Stress concentrations in the structure 3C-. [Caption: (a) von Mises stress on the structure 3C- for a displacement of 1.5mm; (b) Maximum stress area with a red oval signalling the maximum stress; (c) Central cell of the structure.] [Note: (b) and (c) share the same scale, in order to accentuate the stress concentrations]

Looking at the stress distribution of the structure 3C- with regular borders, in Figure 4.11(a) the stress distribution shows that the gradient has an effect since the lower stresses are in sections where the

thickness of the cell wall is greater and the stress is higher where the thickness is thinner. Also, looking at the stress distribution, it shows that the maximum stress occurs on the left side of the structure over a line which is highlighted by a red oval in Figure 4.11(b). This indicates that there is a stress concentration in those points, which goes with what was said in the previous section: the stress concentrations will occur at the junction of three cell walls. Moreover, since this concentration occurs near a non-filleted corner, which can further lead to crack propagation, in structures which have filleted corners such as the Plateau or Lotus configurations, these stress concentrations were mitigated. Furthermore, the central cell has sections near its corners with stress in the range of 318 MPa to 434 MPa (Figure 4.11(c)) which could lead to a crack appearance and then its propagation.

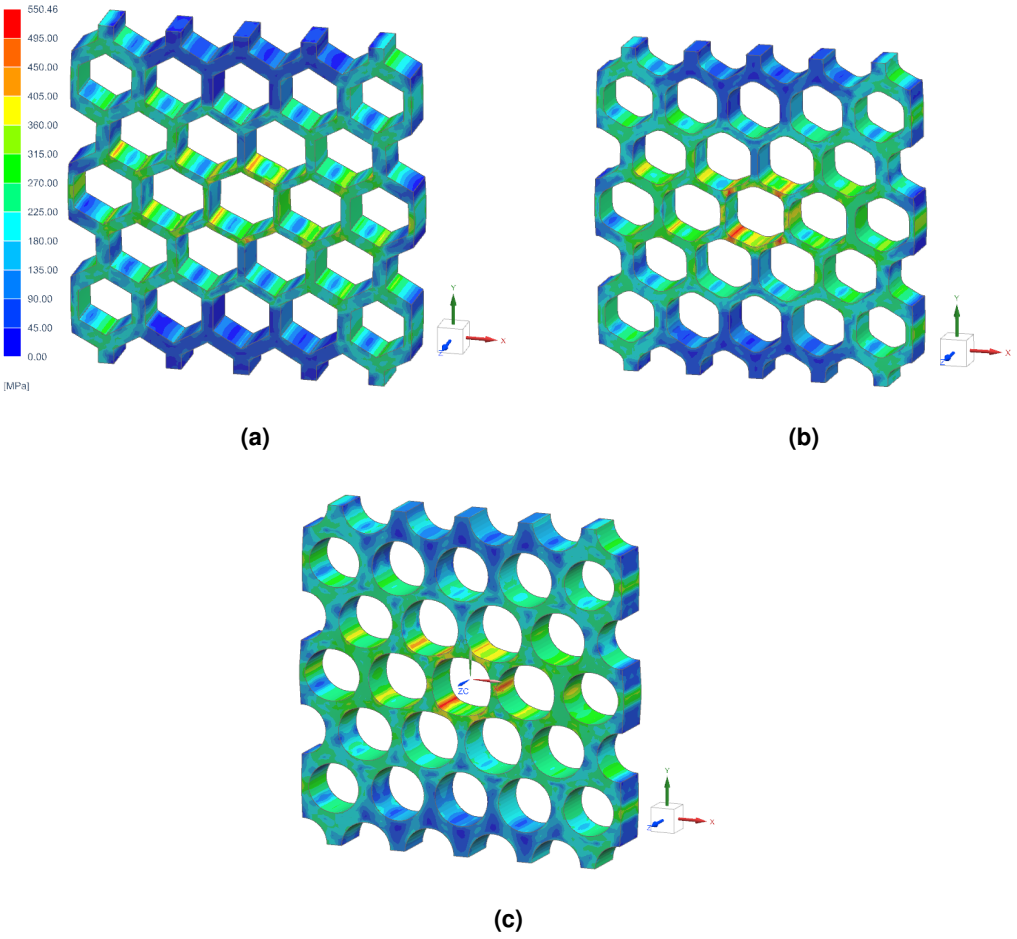

Figure 4.12: von Mises stress of the structures (a) 3C-, (b) 3C-_Pt and (c) 3C-_Lt. [Note: all the figures use the scale in (a).]

Moving to the Plateau and Lotus configurations of the variant 3C-, Figure 4.12(b) shows that there is a clear influence of the borders in the stress distribution. In Figure 4.12(a), the stress concentrations have been reduced to the ones on the central cell, and the whole structure maintains its stress distribution in the same range as the previous variation. Moreover, as it can be seen from the graph in Figure 4.10,

the Plateau border variation sustains a higher force than the one with regular hexagonal borders. Then, looking at the stress distribution of the structure 3C-_Lt (Figure 4.12(c)), once again it can be seen that the stress distribution of the majority of the structure falls, within the range of the 180 $\sim$ 315 MPa. Like the 3C-_Pt structure, the stress concentrations are localised within the central cell and due to the shape of the Lotus borders the chance of creating a crack is smaller when compared to the regular hexagons variant. Also, it can be seen that the stress is lower in cell walls whose thickness is greater and that the increase in the relative density due to the configuration of the repeating units has an influence on the stress distribution as the Lotus configuration is able to maintain a stress distribution similar to the regular hexagons despite withstanding a higher force.

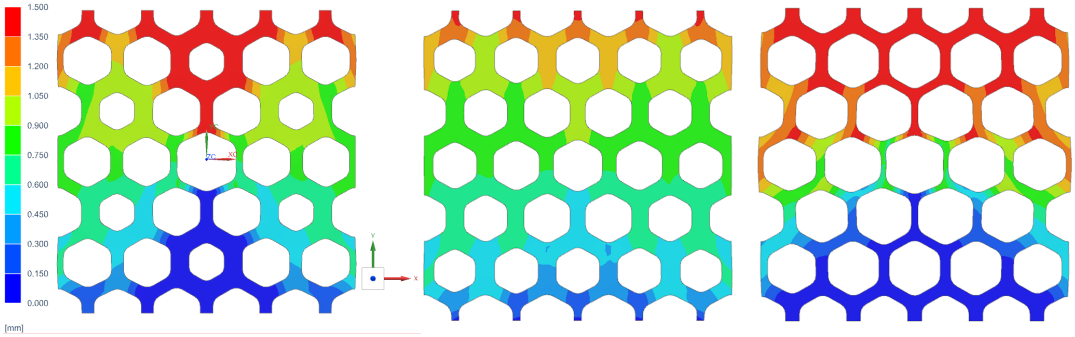

Figure 4.13: Deformation of structures 1B_Pt, 2C_Pt and 3C-_Pt, from left to right, respectively, for 1.5mm of displacement

Also, the gradient has an effect on the deformation of the structure. As it can be seen in Figure 4.13, the thicker cell walls had lower deformation than those with thinner cell walls. This effect is more clear in gradient 1B_Pt in Figure 4.13.

The remaining structures follow what was described for this particular variant, more specifically: the high specific stiffness, specific energy absorbed and specific yield stress of the Lotus configuration when compared to the other configurations; the decrease in the stress distribution of thicker cell walls; and the mitigation of stress concentrations with filleted corners (Plateau and Lotus configuration). The force-displacement curves, stress distributions and deformation distributions of the remaining structures can be seen in Appendix A.

4.3 Linear gradient structures

Moving to the linear gradients, these are the gradients, 4, 5 and 6, the specific mechanical properties can be seen in Table 4.5.

The data shows that gradient 4 follows the trend that was pointed out in Sections 4.1 and 4.2; the specific stiffness, specific energy absorbed and specific yield stress decrease as the relative density

Table 4.5: Results for the gradients 4, 5 and 6.

Structure	$\bar{\rho}$	$\bar{K}$ [kN/mm]	$\bar{E}_a$ at 1.5mm [J]	$\bar{\sigma}_y$ [MPa]	σ_{max} at 1.5 mm [MPa]
4A	0.404	148.31	86.58	34.02	554.03
4A_Pt	0.416	183.34	105.25	42.15	516.68
4A_Lt	0.460	232.61	129.97	53.56	437.63
4B	0.354	78.72	40.15	16.04	636.61
4B_Pt	0.367	112.40	57.11	22.86	680.91
4B_Lt	0.414	169.32	86.17	34.56	598.89
4C[1]	0.319	33.40	5.46	5.12	466.62
4C_Pt	0.333	56.50	23.08	8.66	716.51
4C_Lt	0.383	115.43	49.53	17.74	707.04
5HPL	0.334	143.52	108.23	51.27	388.29
5PHL	0.329	147.43	110.55	52.65	407.85
5LPH	0.329	147.11	112.16	52.65	392.91
6HPL_-0.05	0.282	109.26	78.09	37.73	435.67

[1]the FEA could only perform to a displacement of 0.693 mm.

decreases. Furthermore, the Lotus configuration once again excels in all variants when compared with the regular hexagons and Plateau configuration.

Comparing the structures 4A, 4B and 4C, it can be seen that a decrease in the relative density, also decreases the specific stiffness, specific energy absorbed and specific yield stress. More specifically, 4B has a specific stiffness 46.9% lower than 4A, and 4C is 77.5% lower than 4A. Looking at the specific energy, 4B has a specific energy absorbed 53.6% lower than 4A and 4C is 93.6% lower. Lastly, the specific yield strength in 4B is 52.9% lower than 4A and 4C is 85.0% lower than 4A. The graph in Figure 4.14 shows these differences.

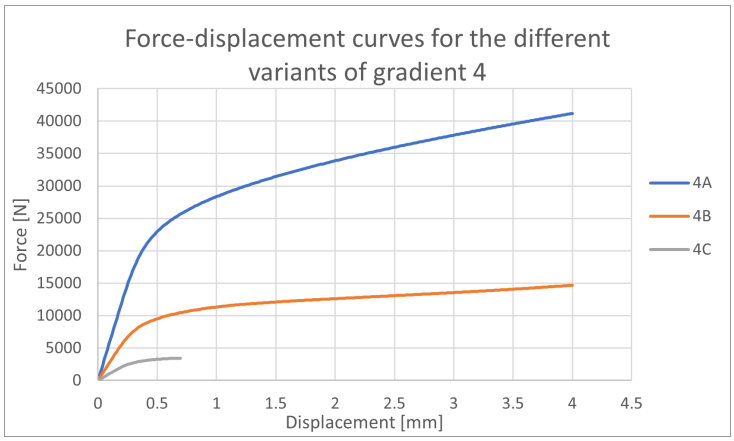

Figure 4.14: Force-displacement curves for several variants of gradient 4.

Looking at the stress distributions, it can be seen that the stress is levelled depending on the L_1 of

the cell. In Figures 4.15(a) and 4.15(b), it can be seen that the stress along a horizontal line of repeating cell, the stress is contained within a given range. For instance, in Figure 4.15(a), on the top row of repeating units, the stress is within the range of 330 MPa to 554 MPa, whilst the middle line row is in the range of 110 MPa to 385 MPa.

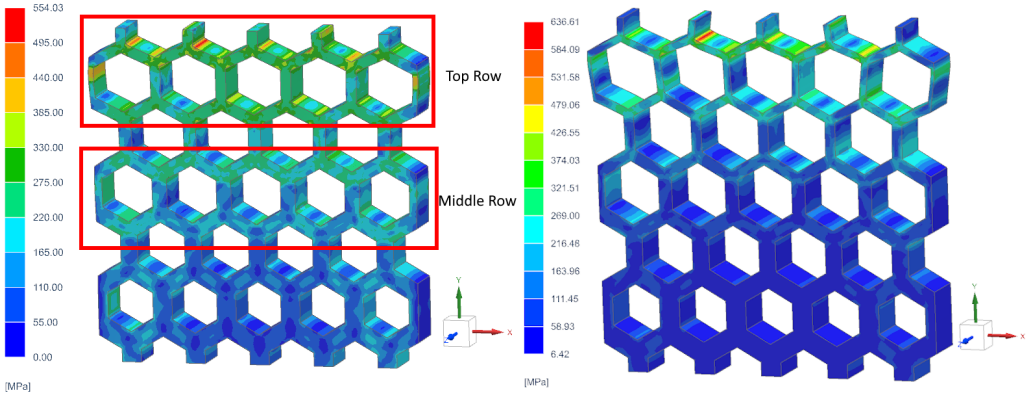

(a)

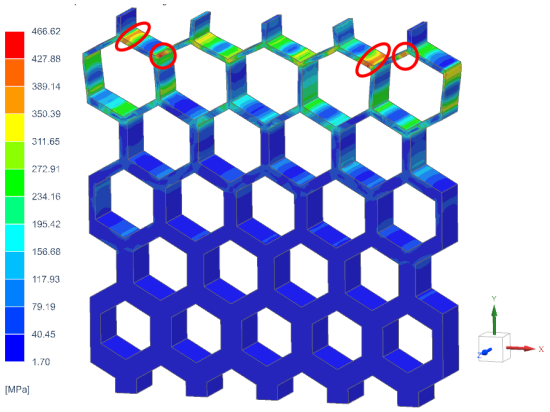

(b)

Figure 4.15: von Mises stress of the structures with gradient (a) 4A and 4B, from left to right, (b) and 4C. [Note: In (a) the red rectangles indicate the top row and the middle row of cells and in (b) the red circles and ovals indicate the high-stress regions.]

As the gradient changes the L_1 from each row more drastically, meaning the gradient becomes steeper, the stress concentrations in the triple junctions become more evident. For instance, in structure 4A (Figure 4.15(a) - left) the stress distribution indicates that the maximum stress was 554.03 MPa in a stress concentration at a triple cell wall junction. In structure 4B, (Figure 4.15(a) - right) the same stress concentration was 638.61 MPa and in structure 4C (Figure 4.15(b)), the FEA could not go further than 0.693mm of displacement and the stress concentration hold a value of 466.62 MPa which was higher than the material's ultimate tensile strength (375 MPa). Additionally, it can be seen that in structure 4A, the stress was more evenly spread than in structures 4B and 4C, which further proves the influence

of the thickness of the cell walls in the stress distribution. Looking at the effect of the repeating cell configuration, the same pattern that was observed in Section 4.1 and 4.2, was observed once again. The stress distributions of the different configurations show that the Plateau configuration decreased the stress concentration and the Lotus configuration further reduced those events. Also, taking the 4A, 4A_Pt and 4A_Lt into consideration, the Lotus variation showed an average increase of 55% on the three specific mechanical properties when compared to the regular hexagons counterpart, while the Plateau configuration only showed an average increase of 21% on the three specific mechanical properties.

Moving into the results of the configurations of a given variant and taking variant 4A as an example (Table 4.5) it can be seen that within the same pattern that was observed in Section 4.1 and 4.2. The Lotus configuration has the highest specific stiffness and specific energy absorbed, followed by the Plateau configuration and lastly by the regular hexagon configuration. Their stress distributions can be seen in Figure 4.16.

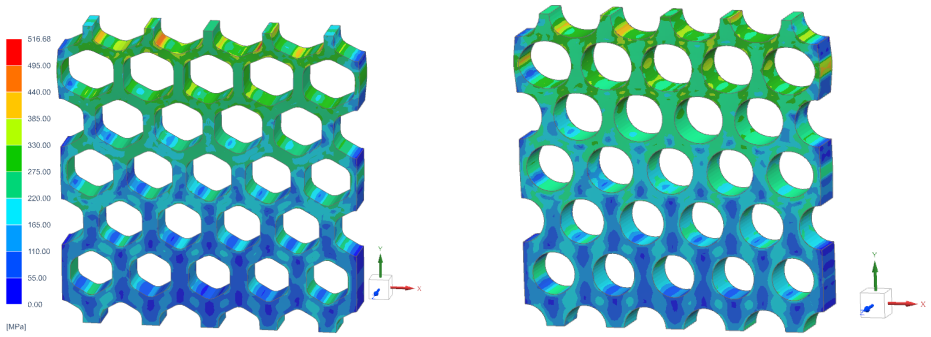

Figure 4.16: von Mises stress of the structures with gradient (a) 4A_Pt and (b) 4A_Lt.

Moving into the structures with gradients 5 and 6, these two gradients were compared since it is relevant to check the variation of the relative density of gradient 6 with the constant relative density of gradient 5.

From Table 4.5 it can be seen that the three variants of gradient 5 are very similar on all the specific mechanical properties. The relative density, specific stiffness, specific energy absorbed and specific yield strength have a variation of 5% among the several variations of gradient 5, which leads to the conclusion that the permutation of the macro repeating unit within a structure has little effect on the specific mechanical properties of the structure. Moreover, upon looking at the stress distribution of the three structures in Figure 4.17 it can be seen that the similarities continue. However, as it was found by X.Zhang *et al.* [22], by placing the weakest element in the outcome plate, an improvement in the specific mechanical properties was found. In this case, by placing the regular hexagons closer to the fixed compression plate, there is a slight increase in the mechanical properties of the structure. The

macro repeating unit is the weakest as it has the thinnest cell wall thickness.

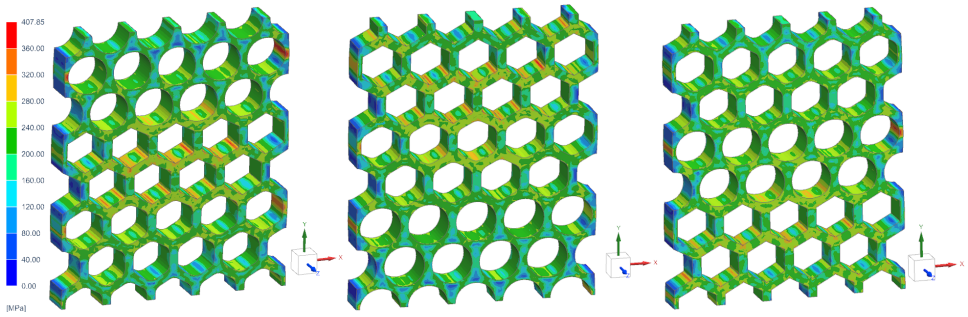

Figure 4.17: von Mises stress of the structures 5HPL, 5LHP and 5PLH, from left to right, respectively.

As it can be seen in all images the peak stress occurs near the edges of the cells with the regular hexagon borders. Yet the most meaningful result that can be taken from these structures is their deformation distribution (Figure 4.18). The deformation of the structures shows that the regular hexagons suffer more deformation, followed by the Plateau cells and then the Lotus ones. This comes from the fact that the Lotus cell has a higher relative density, thus a higher stiffness and therefore requires more force to be deformed than the Plateau or the regular hexagons. Knowing this these gradients can be used to control the deformation of the structure depending on the needs of the application.

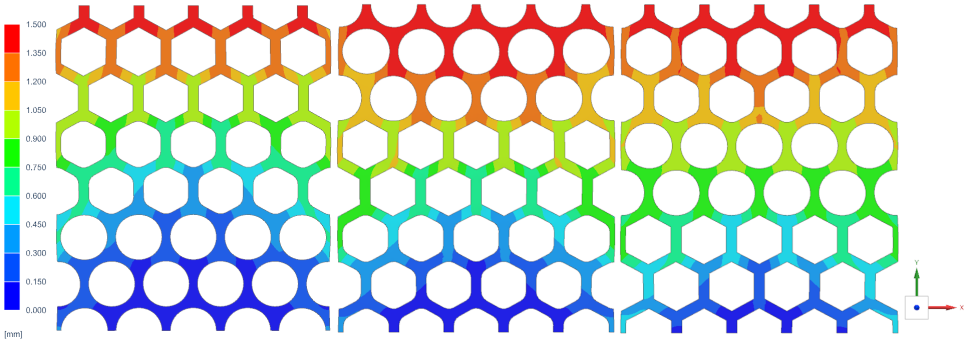

Figure 4.18: Deformations of the structures 5HPL, 5LHP and 5PLH, from left to right, respectively.

When comparing the structure 6HPL_-0.05 (Figure 4.19) to those with gradient 5, it can be seen that the 6HPL_-0.05 has a specific stiffness 23.9% lower than the gradient 5 structures, a decrease of 27.9% in the specific energy absorbed and a decrease of 26.4% in the specific yield stress. Due to the nature of the gradient 6, the Lotus repeating unit has thinner cell walls than the Plateau macro repeating units and the regular hexagon macro repeating units, therefore it is not unexpected that the Lotus macro repeating units have higher stresses than the rest of the structure and thereby a larger deformation. It can be seen that the stress concentrations occur near the triple junctions of the cell walls. Lastly, it can be said that the variation of the relative density in 6HPL_-0.05 was steep enough to decrease the specific mechanical properties. This phenomenon was seen with gradient 4, where a steeper gradient

(4C) would produce lower specific mechanical properties, while a less steep gradient had higher specific mechanical properties.

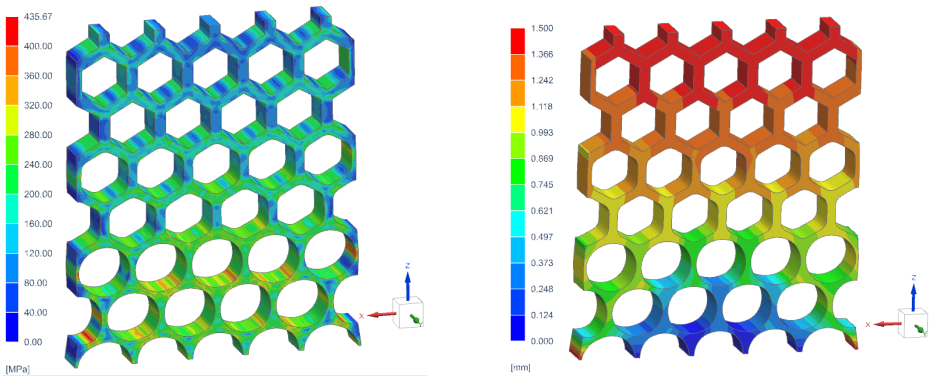

(a) **(b)**

Figure 4.19: von Mises stress and deformation of structure 6HPL_-0.05, from left to right, respectively.

4.4 Performance analysis

Whenever a wide array of solutions is presented, it is necessary to have a method to rank the solutions from the best to worst such that the most appropriate solution can be found. In this work, the performance of the structures studied was evaluated by their specific mechanical properties, and for that an adimensional index was used to compare all the structures on equal footing.

The index used to compare all solutions was the Geometric Efficiency Index (GEI), an index first developed by J. Berger *et al.* [59] and then proposed by D. Bhate *et al.* [6]. This index is calculated by dividing the mechanical property of the structure by the same mechanical property of a dense block with the same functional dimensions of the honeycomb structure. An example of a equation for this index is the GEI for the stiffness (Equation 4.1).

$$GEI_K = \frac{\frac{K^*}{K_s}}{\frac{\rho^*}{\rho_s}} \tag{4.1}$$

In Equation 4.1, K^* is the stiffness of the structure, K_s is the stiffness of a block with the same functional dimensions to the structure, ρ^* is the density of the structure and ρ_s is the density of block with equal dimensions to the structure. The ratio between ρ^* and ρ_s is the relative density which was introduced in Section 2.1. This index is the most appropriate for this analysis because it takes into account the relative density and the mechanical properties of the structure and its outcome makes it possible to rank the efficiency of the structure on a scale of 0 to 1, where 1 is the best-performing structure and 0 is the worst-performing one. Another advantage of this index is that it can be applied

to the remaining mechanical properties of the structures - energy absorbed (Equation 4.2) and yield strength (Equation 4.3).

$$GEI_{E_a} = \frac{\frac{{E_a}^*}{E_{a_s}}}{\frac{\rho^*}{\rho_s}} \tag{4.2}$$

$$GEI_{\sigma_y} = \frac{\frac{{\sigma_y}^*}{\sigma_{y_s}}}{\frac{\rho^*}{\rho_s}} \tag{4.3}$$

It should be noted that the GEI for the energy absorbed was one the for the energy absorbed for a displacement of 1.5mm in order to maintain the consistency in this work.

The K_s, E_{as} and σ_{y_s} were determined by performing a FEA on blocks with the same fucntional dimensions as the structures in this work. The parameters of the analysis were the same as described in Section 3.4 and the data was obtained with the same method described in subsection 3.6.3. The properties of the blocks will be presented in Appendix B.

The values of the GEI_K, GEI_{E_a} and GEI_{σ_y} are presented in the Table 4.6 and a chart with the GEI values of the three properties is presented in Figure 4.20.

Table 4.6: Geometry Efficiency Index for the specific stiffness and specific energy absorbed for all structures.

Structure	GEI_K	GEI_{E_a}	GEI_{σ_y}	Structure	GEI_K	GEI_{E_a}	GEI_{σ_y}
L6	0.196	0.513	0.248	3B+	0.124	0.302	0.125
L6_Pt	0.245	0.613	0.324	3B+_Pt	0.167	0.393	0.168
L6_Lt	0.305	0.718	0.403	3B+_Lt	0.237	0.538	0.239
L8	0.128	0.344	0.144	3C-	0.145	0.333	0.127
L8_Pt	0.168	0.438	0.197	3C-_Pt	0.188	0.413	0.164
L8_Lt	0.240	0.585	0.280	3C-_Lt	0.263	0.554	0.229
L10	0.079	0.240	0.096	4A	0.216	0.448	0.178
L10_Pt	0.106	0.311	0.140	4A_Pt	0.267	0.544	0.221
L10_Lt	0.168	0.443	0.219	4A_Lt	0.339	0.672	0.281
1B	0.228	0.292	0.191	4B	0.115	0.208	0.084
1B_Pt	0.273	0.338	0.229	4B_Pt	0.164	0.295	0.120
1B_Lt	0.339	0.403	0.283	4B_Lt	0.247	0.446	0.181
2C	0.284	0.587	0.171	4C	0.049	0.028	0.027
2C_Pt	0.326	0.659	0.196	4C_Pt	0.082	0.119	0.045
2C_Lt	0.386	0.769	0.232	4C_Lt	0.168	0.256	0.093
2D	0.258	0.542	0.203	5HPL	0.246	0.601	0.292
2D_Pt	0.299	0.612	0.235	5LHP	0.253	0.614	0.300
2D_Lt	0.358	0.717	0.280	5PLH	0.252	0.623	0.299
3A+	0.175	0.438	0.201	6HPL_-0.05	0.187	0.433	0.215
3A+_Pt	0.222	0.540	0.254				
3A+_Lt	0.289	0.664	0.331				

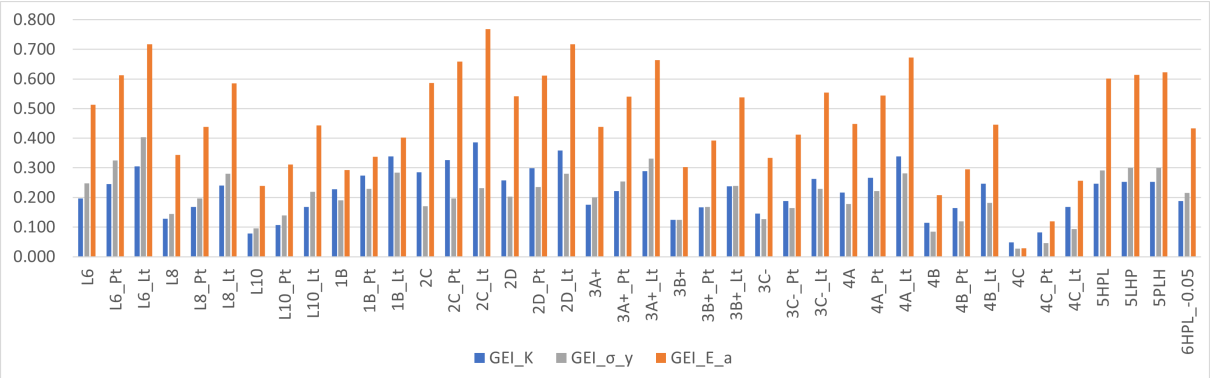

Figure 4.20: GEI of the stiffness, energy absorbed and yield strength.

As it can be seen in Figure 4.20, the gradient with the highest GEI_K was the 2C_Lt, the one with the highest GEI_{σ_y} is the L6_Lt and the one with the highest GEI_{E_a} is the 2C_Lt. Within the regular structures, the variant with the highest GEI values was the L6_Lt; in the radial gradients, the structure 2C_Lt has the highest GEI_K and GEI_{E_a}, but the structure 3A+_Lt has the highest GEI_{σ_y}; in the linear gradients, the structure 4A_Lt has the highest GEI_K and GEI_{E_a}, and the structure 5PLH has the highest GEI_{σ_y}. Comparing the structures amongst each other, the Lotus configurations obtain the highest values in the GEI within all gradients, followed by the Plateau and then the regular hexagons. From the regular structure, L6, L8 and L10, it was seen that a decrease in the L_1 increases the GEI on all three parameters. Looking at gradient 3, it was seen that a less steep gradient produced a higher GEI, as the variant 3A+ has a less steep gradient and has higher GEI values than the 3B+ variant with a steeper gradient. This phenomenon was also seen in the linear gradient 5, where variant 4A has higher GEI values and it has a less steep gradient.

The linear gradient 5 was able to obtain a GEI_{E_a} higher than most of the regular hexagons and Plateau configurations, but the structure 6HPL_-0.05 had lower GEI values than the gradient 5 variant, this might come from the large variation in the relative density of the macro repeating units.

With this analysis, it can be stated that the gradients of the honeycombs can be modelled to the needs and requirements of its application. Taking the regular structures as the baseline for the performance of the honeycombs, it can be seen that the radial gradients had a higher specific stiffness and specific energy absorption. Still, they lack the specific yield strength, which is where the linear gradients excel. Furthermore, the gradient can be used to control the deformation which could then be used to control the fracture of the specimen, as it was seen with the gradients 3 and 5, where the thinner cell walls would deform first, and hence more likely to fracture first.

Lastly, as the purpose of the honeycombs is to increase the mechanical properties whilst reducing weight, a graph of the GEI, against the relative density is represented in Figures 4.21, 4.22 and 4.23 to understand the relationship between the performance of the gradient and its relative density, which

is directly related to the weight of the structure. Despite the dispersion of the results in Figures 4.21, 4.22 and 4.23, a general trend can be seen, as the relative density increases, so does the GEI of the respective mechanical property. This trend goes in line with the findings of previous papers, where an increase in the relative density of the structure corresponded into an increase of the mechanical properties of the structure [20–26]

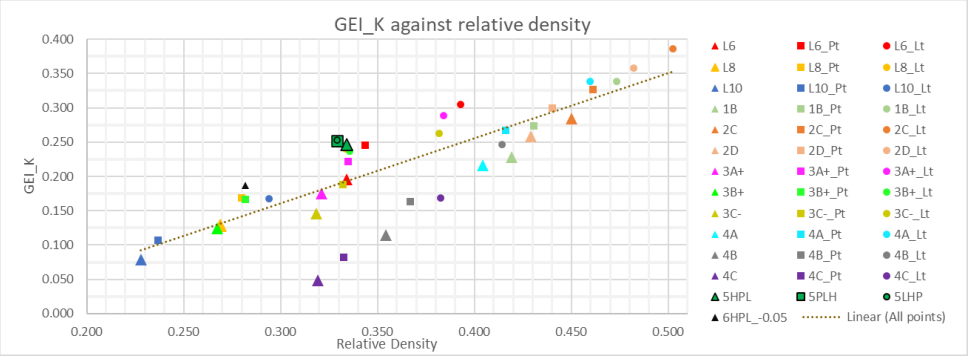

Figure 4.21: GEI of the stiffness against the relative density.

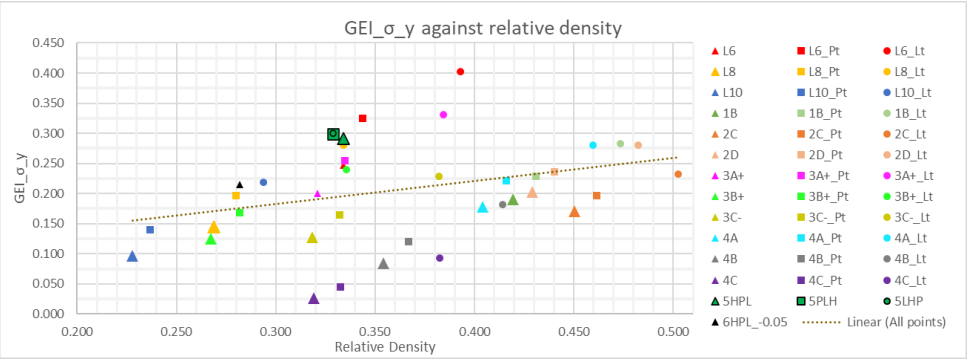

Figure 4.22: GEI of the yield strength against the relative density.

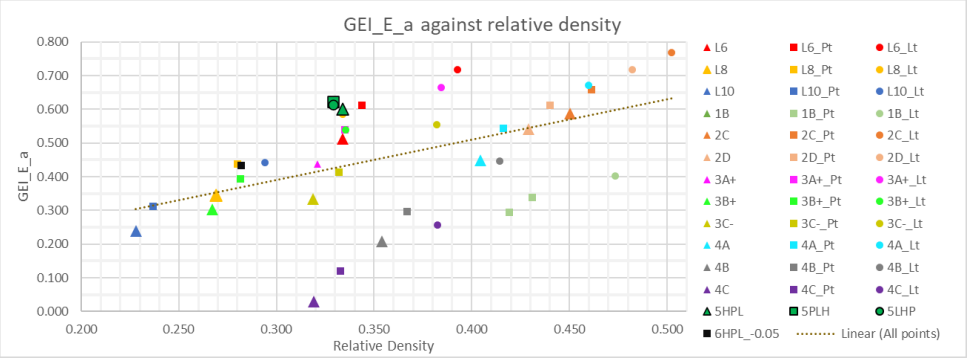

Figure 4.23: GEI of the energy absorbed against the relative density.

5

Conclusion

Contents

5.1 Conclusions

In this work it was aimed to assess the influence of several gradients on the mechanical properties of the structures, and the influence of the variation of the repeating unit on those properties. It was also a goal to assess the efficacy of the gradients studied, and the accuracy of the FEA in predicting the mechanical properties of the structures. For the latter, experimental work was carried out to assess the influence of a heat treatment on the mechanical properties of the structures. The experimental works were made on the regular structures, and the FEA were made on all the structures.

In this work, three major types of gradients were applied: regular, radial and linear. Besides these gradients, it was also studied the influence of three types of cell units: regular hexagons, regular hexagons with Plateau borders, and Lotus borders. All the gradients had these three configurations. The regular structures had no gradient, hence the L_1 was constant on all repeating units. The radial gradient affected the L_1 in a radial direction, and the dimension would vary according to the position of the unit cell in regard to the central unit cell of the structure. The linear gradient varied the L_1 of the unit cell according to the distance of the unit cell to a row of unit cells. Within the regular structures, three structures with different L_1 were used. Within the radial structures, three types of gradients were studied: one which the L_1 would be imposed according to the distance of the unit cell to the centre of the structure; another in which the L_1 would be added an increment depending on the structures in its vicinity; and a last one whose L_1 would depend linearly on the distance of the unit cell to the centre of the structure. There was also three types of linear gradients: one which the L_1 would depend linearly on the vertical distance of a unit cell to the bottom row of unit cells; another one which had three clusters of different type of cell unit, and three permutations of the cells units were studied, also it was studied on the previous permutation with a linear gradient on the relative density.

All of the structures were subjected to a compression test to evaluate their stiffness, energy absorbed and yield strength. Through the FEA it was possible to determine these parameters and maximum stress, together with the distribution of stresses and deformations.

Upon looking at the results obtained with the FEA, it was possible to find that the structures with higher relative density have higher specific stiffness, specific energy absorbed and specific yield stress. For instance, in the regular honeycombs the Lotus repeating unit displayed an increase in the specific stiffness by 55.6% when compared to the regular hexagons and 25.0% when compared to the Plateau units. In terms of specific energy absorbed, the Lotus had an increase of 39.8% and 19.4% when compared to the regular hexagons and Plateau units, respectively. In terms of the specific yield strength, the Lotus displayed an increase of 62.7% and 31.0% when compared to the regular hexagons and Platau units, respectively. This pattern was observed across all the gradients and it happened due to the higher relative density of the Lotus configuration and from its lack of sharp edges, they are capable of withstanding higher forces than the other configurations. From the stress distributions, it was possible to

find out that the regular hexagons structures had more stress concentrations than the other two configurations. These stress concentrations would appear in the junction of three cell walls, which is where the fracture would occur in the experimental testing. The Plateau configuration mitigated these stress concentrations and would allow the structure to withstand higher forces. For instance, the structure L6 had a maximum stress of 430.34 MPa and the Plateau counterpart, L6_Pt, had a maximum stress of 409.96 MPa, whilst sustaining a force of around 29000N for a displacement of 1.5 mm, while the L6 only sustained 24000 N for the same displacement. The Lotus configuration would further enhance the mechanical properties when compared to the Plateau configuration, for example, the specific energy absorbed of the structure L6_Pt is 96.99 J, while L6_Lt was 113.58 J. In terms of the deformation of the structure, the Lotus configuration had the lowest deformation of the three configurations, while the regular hexagons had the highest when subjected to an equal force. Looking at the several gradients analysed, it could be seen that the gradient 2C_Lt had the highest specific energy absorbed (167.23 J) and the highest specific stiffness (270.65 kN/mm), while the structure L6_Lt had the highest specific yield strength (72.27 MPa). In the regular gradients, the structures with the higher relative densities had the highest specific mechanical properties and the lowest maximum stresses, whilst withstanding higher forces. In the radian gradient, the same pattern was observed, but it could be further noted that the structures whose gradient was less steep, meaning the variation of the L_1 was relatively small, had better results than those with steeper gradients, *i.e.* the structure 3A+_Lt had a less steep gradient than structure 3B+_Lt and 3C-_Lt, and had higher specific mechanical properties. In the linear gradient, the relationship between the relative density and the mechanical properties was, once again, observed. Also, the structures whose gradient was less steep (4A), had better mechanical properties than those with a steeper gradient (4C). It was also found with gradient 5, that changing the location of repeating units has little effect on the mechanical properties, however, the location of the ”weakest” repeating unit in the fixed-end plate, would increase slightly the mechanical properties. With the fifth gradient, it was also possible to compare the deformation of the repeating unit, and it was found that the regular hexagons deform the most while the Lotus deform the least. Lastly, the sixth gradient showed a decrease in all the mechanical properties, but it paved the way for further improvements with this gradient since it allows localising the larger deformations.

Regarding the experimental testing, it was found that an increase in the relative density results in an increase in the specific mechanical properties. Also, it was found that the numerical model matches the experimental testing, as it can predict the force-displacement curves and the numerical curves are always above the experimental ones. The latter is a very important point since the numerical model assumes that the structures are perfect, meaning the material is isotropic, there are no residual stresses and there are no voids within the structures which may weaken them. As the manufacturing method creates a very rough surface, it provides an environment that promotes crack propagation, also the

manufacturing method creates inclusions within the structure which later will further promote the crack propagation. All of these factors contribute to the disparity between the numerical and experimental results, yet they can be considered satisfactory for the reasons mentioned above.

Also, with the experimental results it was found that as the relative density decreased, the discrepancy between the numerical and experimental results also decreased. Besides these comparisons, it was also tested specimens which underwent an annealing. The results showed an increase in the ductility and a decrease in the stiffness of the structures, meaning the specific stiffness and specific yield stress decreased, but the displacement before fracture and energy absorbed before fracture increased.

In order to compare all the structures on equal footing and assess which structure has the most efficiency in mechanical terms, the GEI was applied to the stiffness, energy absorbed and yield strength. It was found that the structure 2C_Lt has the highest GEI_K and GEI_{E_a}, while the structure L6_Lt has the highest GEI_{σ_y}. In the performance analysis, it was also found a pattern where the GEI for the three mechanical properties increase as the relative density increases.

To conclude, with this work, it was possible to develop a numerical model that fits the experimental testing and which produced similar results to the previous thesis, hence the continuity of this work is assured. It was possible to find that as the relative density increases, so do the specific mechanical properties of the structure, but it is possible to develop a structure according to the needs of the situation. Furthermore, it was found that structures with steeper gradients underperform, while less steeper gradients show a better performance. It was also possible to develop a gradient where it is possible to localise the major deformations. Lastly, the annealing increases the ductility of the structures while decreasing the stiffness.

5.2 Future work

No work will ever be truly complete where all possible considerations are taken, hence some suggestions regarding future investigations and work will be left in this section.

- Derive a single equation that can define the regular hexagons, hexagons with Plateau borders and Lotus borders, to create structures with variable cell configuration;
- Perform compression trials to the point where the densification of the structure can be achieved, with a machine which can withstand such forces;
- Perform blast trials to assess the energy absorption;
- Use other materials that rely on the same manufacturing method but maintaining the same structures;
- Apply the honeycombs from this work to a real-life example and further improve the gradients;

- Use other numerical methods such as the meshless methods for the numerical analysis, in order to reduce the computing time whilst maintaining accuracy.

Bibliography

[1] L. J. Gibson and M. F. Ashby, *Cellular solids: Structure and properties*. Cambridge University Press, 1997.

[2] B. Castanie, C. Bouvet, and M. Ginot, "Review of composite sandwich structure in aeronautic applications," *Composites Part C: Open Access*, vol. 1, p. 100004, 2020. [Online]. Available: https://www.sciencedirect.com/science/article/pii/S2666682020300049

[3] B. C. Coelho, "Modeling and Characterization of Honeycomb Structures with Density Gradient Produced by Additive Manufacturing Technologies," Master's thesis, Instituto Superior Técnico, November 2022. [Online]. Available: https://fenix.tecnico.ulisboa.pt/cursos/memat/dissertacao/846778572213791

[4] A. Lagorce-Tachon, T. Karbowiak, D. Champion, R. D. Gougeon, and J.-P. Bellat, "Mechanical properties of cork: Effect of hydration," *Materials Design*, vol. 82, pp. 148–154, 2015. [Online]. Available: https://www.sciencedirect.com/science/article/pii/S0261306915002812

[5] A. Sharir, M. M. Barak, and R. Shahar, "Whole bone mechanics and mechanical testing," *The Veterinary Journal*, vol. 177, no. 1, pp. 8–17, 2008. [Online]. Available: https://www.sciencedirect.com/science/article/pii/S1090023307003292

[6] D. Bhate, C. Penick, L. Ferry, and C. Lee, "Classification and selection of cellular materials in mechanical design: Engineering and biomimetic approaches," *Designs*, vol. 3, no. 1, p. 19, Mar 2019. [Online]. Available: http://dx.doi.org/10.3390/designs3010019

[7] J. Møller and D. Stoyan, "Stochastic geometry and random tessellations," *Tessellations in the sciences: virtues, techniques and applications of geometric tilings*, 10 2009.

[8] S. D'Agostino, "Voronoi tessellations and scutoids are everywhere," January 2019, accessed on 2023-07-27 at 16h09. [Online]. Available: https://blogs.scientificamerican.com/observations/voronoi-tessellations-and-scutoids-are-everywhere/

[9] L. Xu and D. Mould, “A procedural method for irregular tree models,” *Computers Graphics*, vol. 36, no. 8, pp. 1036–1047, 2012, graphics Interaction Virtual Environments and Applications 2012. [Online]. Available: https://www.sciencedirect.com/science/article/pii/S0097849312001410

[10] Accessed on 2023-07-12 at 11h51. [Online]. Available: https://www.vonhagens-plastination.com/pages/medical-teaching-specimens/von-hagens-plastination.php/productPost_04_toInquiryList?numberProductDescription=HB7006

[11] Accessed on 2012-07-12 at 11h32. [Online]. Available: https://www.pexels.com/photo/cracked-dry-land-4068167/

[12] J. Mason, E. Lazar, R. MacPherson, and D. Srolovitz, “Geometric and topological properties of the canonical grain growth microstructure,” *Physical Review E*, vol. 92, 07 2015.

[13] D. Pereira, F. P. Alves, L. Reis, M. Leite, A. M. Deus, M. Sardinha, and M. F. Vaz, “Cellular lattice cores of sandwich panels fabricated by additive manufacturing: Effect of dimensions and relative density on mechanical behaviour,” *Proceedings of the Institution of Mechanical Engineers, Part L: Journal of Materials: Design and Applications*, vol. 237, no. 5, pp. 1188–1201, 2023. [Online]. Available: https://doi.org/10.1177/14644207221138003

[14] A. Pais, J. L. Alves, R. N. Jorge, and J. Belinha, “Multiscale homogenization techniques for tpms foam material for biomedical structural applications,” *Bioengineering*, vol. 10, no. 5, p. 515, Apr 2023. [Online]. Available: http://dx.doi.org/10.3390/bioengineering10050515

[15] K. Yeranee and Y. Rao, “A review of recent investigations on flow and heat transfer enhancement in cooling channels embedded with triply periodic minimal surfaces (tpms),” *Energies*, vol. 15, no. 23, p. 8994, Nov 2022. [Online]. Available: http://dx.doi.org/10.3390/en15238994

[16] S. A. Naghavi, M. Tamaddon, A. Marghoub, K. Wang, B. B. Babamiri, K. Hazeli, W. Xu, X. Lu, C. Sun, L. Wang, , and et al., “Mechanical characterisation and numerical modelling of tpms-based gyroid and diamond ti6al4v scaffolds for bone implants: An integrated approach for translational consideration,” *Bioengineering*, vol. 9, no. 10, p. 515, September 2022.

[17] J. Feng, J. Fu, X. Yao, and Y. He, “Triply periodic minimal surface (tpms) porous structures: from multi-scale design, precise additive manufacturing to multidisciplinary applications,” *International Journal of Extreme Manufacturing*, vol. 4, no. 2, p. 022001, mar 2022. [Online]. Available: https://dx.doi.org/10.1088/2631-7990/ac5be6

[18] M. F. Ashby, T. Evans, N. Fleck, J. W. Hutchinson, H. N. G. Wadly, and L. J. Gibson, *Metal Foams: A Design Guide*. Butterworth Heinemann: Oxford, 2000.

[19] B. G. Silva, F. Alves, M. Sardinha, L. Reis, M. Leite, A. M. Deus, and M. F. Vaz, "Functionally graded cellular cores of sandwich panels fabricated by additive manufacturing," *Proceedings of the Institution of Mechanical Engineers, Part L: Journal of Materials: Design and Applications*, vol. 236, no. 9, pp. 1814–1828, 2022. [Online]. Available: https://doi.org/10.1177/14644207221084611

[20] A. Ajdari, H. Nayeb-Hashemi, and A. Vaziri, "Dynamic crushing and energy absorption of regular, irregular and functionally graded cellular structures," *International Journal of Solids and Structures*, vol. 48, no. 3, pp. 506–516, 2011. [Online]. Available: https://www.sciencedirect.com/science/article/pii/S0020768310003720

[21] C. Lira and F. Scarpa, "Transverse shear stiffness of thickness gradient honeycombs," *Composites Science and Technology*, vol. 70, no. 6, pp. 930–936, 2010. [Online]. Available: https://www.sciencedirect.com/science/article/pii/S0266353810000667

[22] X. chun Zhang, L. qiang An, and H. min Ding, "Dynamic crushing behavior and energy absorption of honeycombs with density gradient," *Journal of Sandwich Structures & Materials*, vol. 16, no. 2, pp. 125–147, 2014. [Online]. Available: https://doi.org/10.1177/1099636213509099

[23] L. Xiao and W. Song, "Additively-manufactured functionally graded ti-6al-4v lattice structures with high strength under static and dynamic loading: Experiments," *International Journal of Impact Engineering*, vol. 111, pp. 255–272, 2018. [Online]. Available: https://www.sciencedirect.com/science/article/pii/S0734743X17304852

[24] S. R. Bates, I. R. Farrow, and R. S. Trask, "Compressive behaviour of 3d printed thermoplastic polyurethane honeycombs with graded densities," *Materials Design*, vol. 162, pp. 130–142, 2019. [Online]. Available: https://www.sciencedirect.com/science/article/pii/S0264127518308256

[25] H. Liu, E. T. Zhang, G. Wang, and B. F. Ng, "In-plane crushing behavior and energy absorption of a novel graded honeycomb from hierarchical architecture," *International Journal of Mechanical Sciences*, vol. 221, p. 107202, 2022. [Online]. Available: https://www.sciencedirect.com/science/article/pii/S0020740322001266

[26] S. S. Bagewadi and R. K. Bhagchandani, "Effect of gradient structure on additively manufactured auxetic and hybrid auxetic structure for energy absorption applications," *Proceedings of the Institution of Mechanical Engineers, Part L: Journal of Materials: Design and Applications*, vol. 237, no. 8, pp. 1739–1751, 2023. [Online]. Available: https://doi.org/10.1177/14644207231155750

[27] A. Miranda, M. Leite, L. Reis, E. Copin, M. F. Vaz, and A. M. Deus, "Evaluation of the influence of design in the mechanical properties of honeycomb cores used in composite panels," *Proceedings of the Institution of Mechanical Engineers, Part L: Journal of Materials: Design and Applications*, vol. 235, no. 6, pp. 1325–1340, 2021. [Online]. Available: https://doi.org/10.1177/1464420720985191

[28] H. Araújo, M. Leite, A. R. Ribeiro, A. M. Deus, L. Reis, and M. F. Vaz, "The effect of geometry on the flexural properties of cellular core structures," *Proceedings of the Institution of Mechanical Engineers, Part L: Journal of Materials: Design and Applications*, vol. 233, no. 3, pp. 338–347, 2019. [Online]. Available: https://doi.org/10.1177/1464420718805511

[29] ISO/ASTM, "Additive manufacturing — General principles — Fundamentals and vocabulary," International Organization for Standardization/American Society for Testing and Materials, International Standard ISO/ASTM 52900:2021, 2021.

[30] A. Bhatia and A. K. Sehgal, "Additive manufacturing materials, methods and applications: A review," *Materials Today: Proceedings*, vol. 81, pp. 1060–1067, 2023, international Virtual Conference on Sustainable Materials (IVCSM-2k20). [Online]. Available: https://www.sciencedirect.com/science/article/pii/S2214785321032995

[31] Grand View Research, "Additive Manufacturing Market Size, Share Trends Analysis Report By Component, By Printer Type, By Technology, By Software, By Application, By Vertical, By Material, By Region, And Segment Forecasts, 2022 - 2030," July 2023, accessed on 2023-07-13 at 18h12. [Online]. Available: https://www.grandviewresearch.com/industry-analysis/additive-manufacturing-market#

[32] Precedence Research, "Machining Market (By Type: Lathe Machines, Laser Machines, Milling Machines, Grinding Machines, Winding Machines, Welding Machines, Others; By End-Use: Automotive, Aerospace Defense, Construction Equipment, Power Energy, Industrial, Others) - Global Industry Analysis, Size, Share, Growth, Trends, Regional Outlook, and Forecast 2023-2032," July 2023, accessed on 2023-07-13 at 18h00. [Online]. Available: https://www.precedenceresearch.com/machining-market

[33] R. Jones, P. Haufe, E. Sells, P. Iravani, V. Olliver, C. Palmer, and A. Bowyer, "Reprap – the replicating rapid prototyper," *Robotica*, vol. 29, no. 1, p. 177–191, 2011.

[34] Y. Lu, S. Wu, Y. Gan, T. Huang, C. Yang, L. Junjie, and J. Lin, "Study on the microstructure, mechanical property and residual stress of slm inconel-718 alloy manufactured by differing island scanning strategy," *Optics Laser Technology*, vol. 75, pp. 197–206, 2015. [Online]. Available: https://www.sciencedirect.com/science/article/pii/S0030399215002108

[35] C. Y. Yap, C. K. Chua, Z. L. Dong, Z. H. Liu, D. Q. Zhang, L. E. Loh, and S. L. Sing, "Review of selective laser melting: Materials and applications," *Applied Physics Reviews*, vol. 2, no. 4, p. 041101, 12 2015. [Online]. Available: https://doi.org/10.1063/1.4935926

[36] W. Meiners, K. Wissenbach, and A. Gasser, "Shaped body especially prototype or replacement part production," *DE Patent*, vol. 19, 1998.

[37] A. T. Clare, P. R. Chalker, and S. Davis, “Selective laser melting of high aspect ratio 3d nickel–titanium structures two way trained for mems applications,” *International Journal of Mechanics and Materials in Design*, vol. 4, p. 181–187, 2007.

[38] J.-P. Kruth, B. Vandenbroucke, and J. V. Vaerenbergh, “Digital manufacturing of biocompatible metal frameworks for complex dental prostheses by means of sls/slm,” pp. 139–145, 2005.

[39] M. Wong, S. Tsopanos, C. Sutcliffe, and I. Owen, “Selective laser melting of heat transfer devices,” *Rapid Prototyping Journal - RAPID PROTOTYPING J*, vol. 13, pp. 291–297, 10 2007.

[40] B. Proaño, H. Miyahara, K. Morishita, T. Matsumoto, H. Sakai, H. Noguchi, and S. Hamada, “Annealing effects on fracture process and tensile strength of non-combustible mg products fabricated by selective laser melting,” *Theoretical and Applied Fracture Mechanics*, vol. 120, p. 103411, 2022. [Online]. Available: https://www.sciencedirect.com/science/article/pii/S0167844222001598

[41] N. T. Aboulkhair, I. Maskery, C. Tuck, I. Ashcroft, and N. M. Everitt, “The microstructure and mechanical properties of selectively laser melted alsi10mg: The effect of a conventional t6-like heat treatment,” *Materials Science and Engineering: A*, vol. 667, pp. 139–146, 2016. [Online]. Available: https://www.sciencedirect.com/science/article/pii/S0921509316304890

[42] SLM Solutions, “Al-alloy alsi7mg0,6 / en ac-42200 material data sheet,” SLM Solutions Group AG, Tech. Rep., 2013.

[43] DIN, “Aluminium and aluminium alloys - castings - chemical composition and mechanical properties; german version en 1706:2010,” Deutsches Institut für Normung, Tech. Rep., 2013.

[44] T. V. Rua, “Out-of-Plane Compression Behaviour of Honeycomb Structures with Mass Gradient Produced by Additive Manufacturing Technologies,” Master’s thesis, Instituto Superior Técnico, September 2021. [Online]. Available: https://fenix.tecnico.ulisboa.pt/cursos/memec/dissertacao/1691203502344099

[45] A. de Jesus Valado Miranda, “Desenvolvimento, caracterização e modelação de novos conceitos no projecto de honeycombs usados em painéis compósitos,” Master’s thesis, Instituto Superior Técnico, November 2019. [Online]. Available: https://fenix.tecnico.ulisboa.pt/homepage/ist181571/dissertacao

[46] EKZO, “SLM 125HL,” accessed on 2023-09-01 at 13h54. [Online]. Available: https://www.3dprintekzo.be/products-services/3d-printers/slm-125hl/

[47] J. N. Reddy, *An introduction to the finite element method*. McGraw-Hill, Inc., 1993.

[48] K.-J. Bathe, *Finite Element Procedures*. Prentice-Hall, Inc., 1996.

[49] Siemens, “Multi-step nonlinear user’s guide,” Siemens, Tech. Rep., 2017.

[50] X. chun Zhang, C. chao An, Z. feng Shen, H. xiang Wu, W. gang Yang, and J. pan Bai, “Dynamic crushing responses of bio-inspired re-entrant auxetic honeycombs under in-plane impact loading,” *Materials Today Communications*, vol. 23, p. 100918, 2020. [Online]. Available: https://www.sciencedirect.com/science/article/pii/S2352492819318781

[51] ISO, “Mechanical testing of metals - ductility testing - compression test for porous and cellular metals,” International Organization for Standarization, Tech. Rep. ISO 13314:2011, 2011.

[52] S. A. Glantz, B. K. Slinker, and T. B. Neilands, *Primer of Applied Regression Analysis of Variance*. McGraw-Hill, 2016.

[53] K. E. Atkinson, *An Introduction to Numerical Analysis*. John Wiley & Sons, 1989.

[54] K. Kempen, L. Thijs, J. Humbeeck, and J.-P. Kruth, “Mechanical properties of alsi10mg produced by selective laser melting,” *Physics Procedia*, vol. 39, p. 439–446, 12 2012.

[55] M. Xu, D. Liu, P. Wang, Z. Zhang, H. Jia, H. Lei, and D. Fang, “In-plane compression behavior of hybrid honeycomb metastructures: Theoretical and experimental studies,” *Aerospace Science and Technology*, vol. 106, p. 106081, 2020. [Online]. Available: https://www.sciencedirect.com/science/article/pii/S127096382030763X

[56] L. Liu, P. Kamm, F. García-Moreno, J. Banhart, and D. Pasini, “Elastic and failure response of imperfect three-dimensional metallic lattices: the role of geometric defects induced by selective laser melting,” *Journal of the Mechanics and Physics of Solids*, vol. 107, pp. 160–184, 2017. [Online]. Available: https://www.sciencedirect.com/science/article/pii/S0022509616307608

[57] Z. Zheng, X. Jin, Y. Bai, Y. Yang, C. Ni, W. F. Lu, and H. Wang, “Microstructure and anisotropic mechanical properties of selective laser melted ti6al4v alloy under different scanning strategies,” *Materials Science and Engineering: A*, vol. 831, p. 142236, 2022. [Online]. Available: https://www.sciencedirect.com/science/article/pii/S0921509321015008

[58] H. Niknam and A. Akbarzadeh, “Graded lattice structures: Simultaneous enhancement in stiffness and energy absorption,” *Materials Design*, vol. 196, p. 109129, 2020. [Online]. Available: https://www.sciencedirect.com/science/article/pii/S026412752030664X

[59] J. B. Berger, H. N. G. Wadley, and R. M. McMeeking, “Mechanical metamaterials at the theoretical limit of isotropic elastic stiffness,” *nature*, vol. 543, pp. 533–537, 2017. [Online]. Available: https://www.nature.com/articles/nature21075

A

Force-displacement curves, stress and deformation distributions

This appendix presents the force-displacement curves of all the simulations made in this work, and also with the experimental results obtained. The stress distributions that were not shown in this work are presented as well.

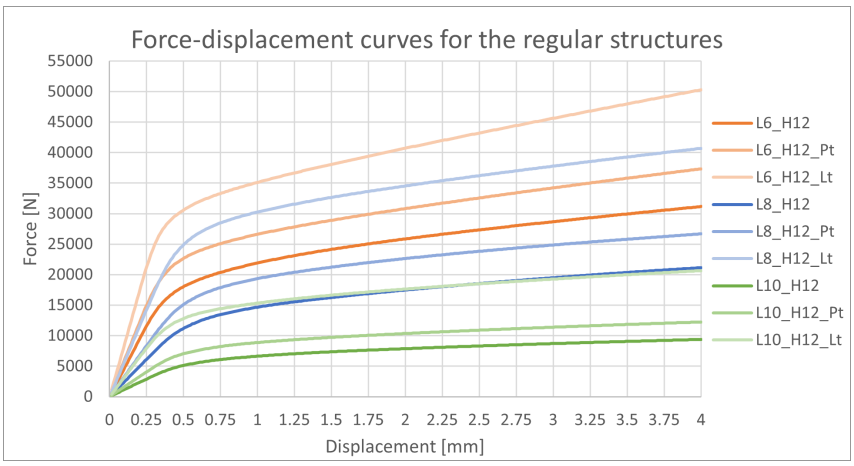

Figure A.1: Force-displacement curves for the L6, L8 and L10 structures.

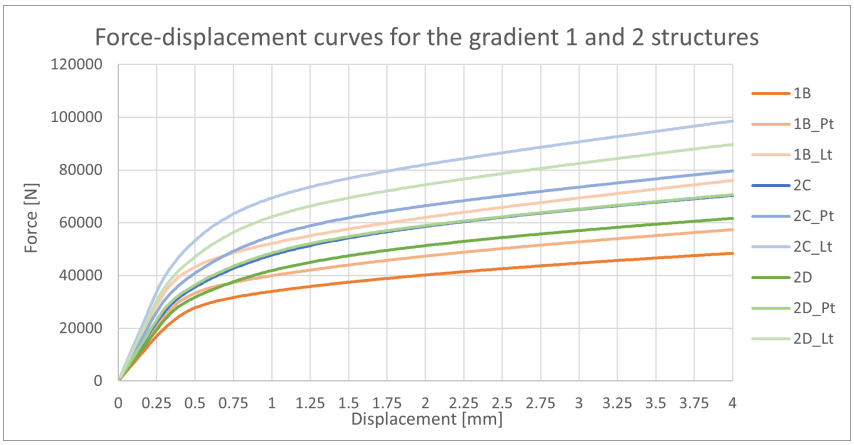

Figure A.2: Force-displacement curves for the gradient 1 and 2 structures.

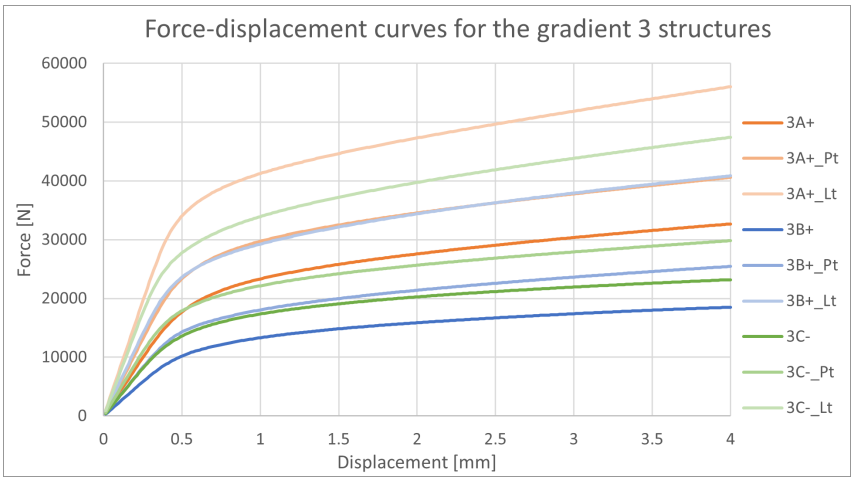

Figure A.3: Force-displacement curves for the gradient 3 structures.

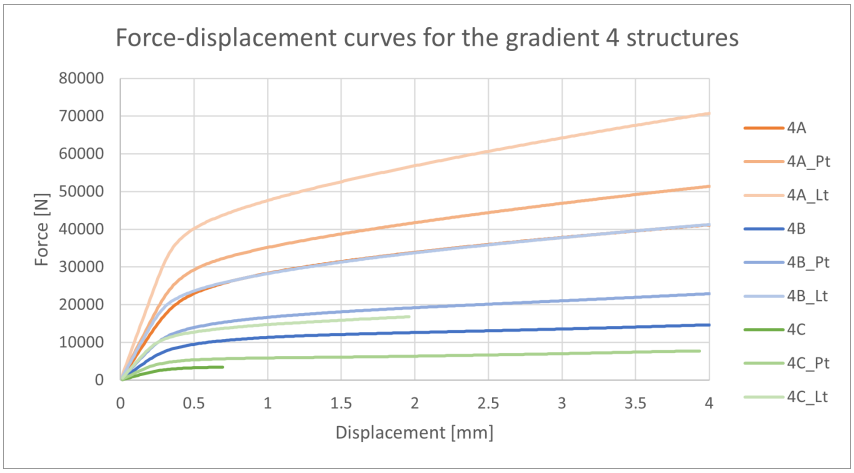

Figure A.4: Force-displacement curves for the gradient 4 structures.

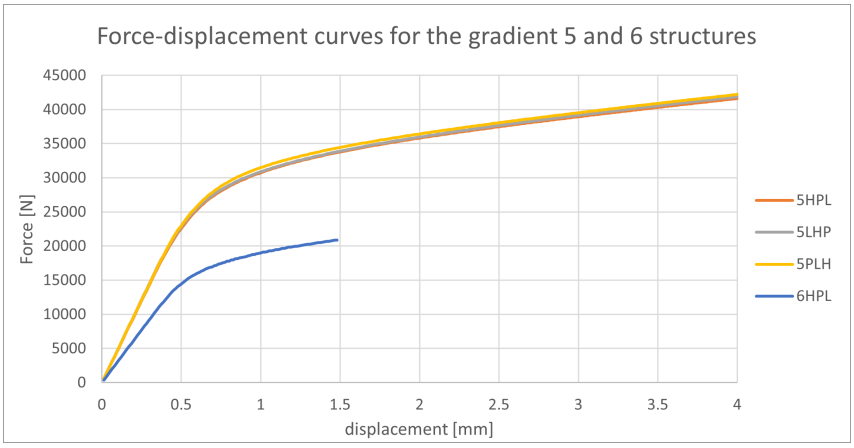

Figure A.5: Force-displacement curves for the gradient 5 and 6 structures.

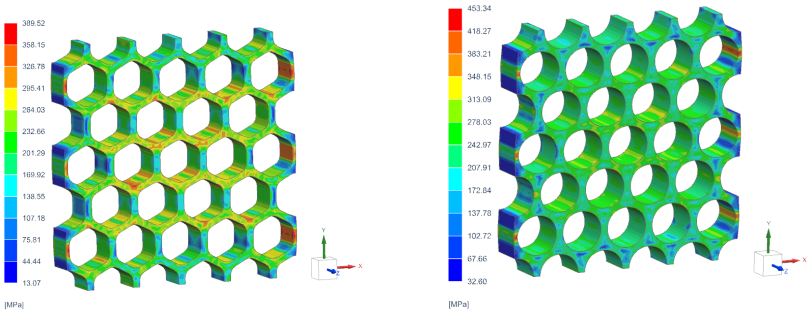

(a) **(b)**

Figure A.6: von Mises stress of the (a) L8_Pt and (b) L8_Lt.

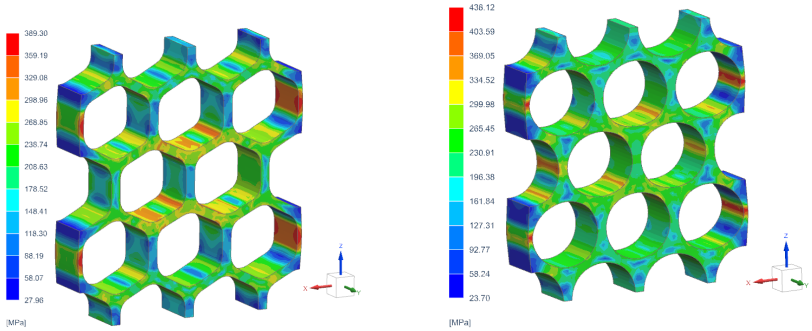

(a) **(b)**

Figure A.7: von Mises stress of the (a) L10_Pt and (b) L10_Lt.

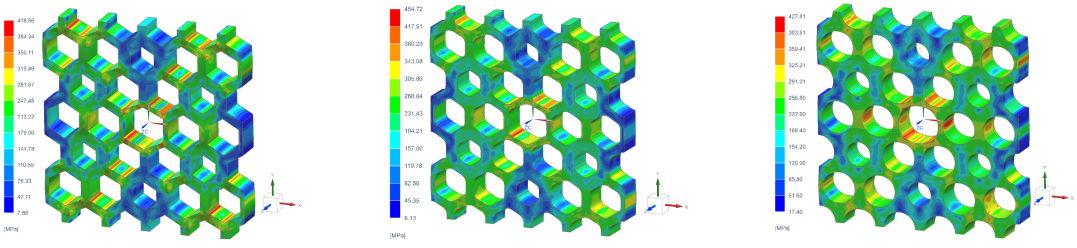

(a) **(b)** **(c)**

Figure A.8: von Mises stress of the (a) 1B, (b) 1B_Pt and (c) 1B_Lt.

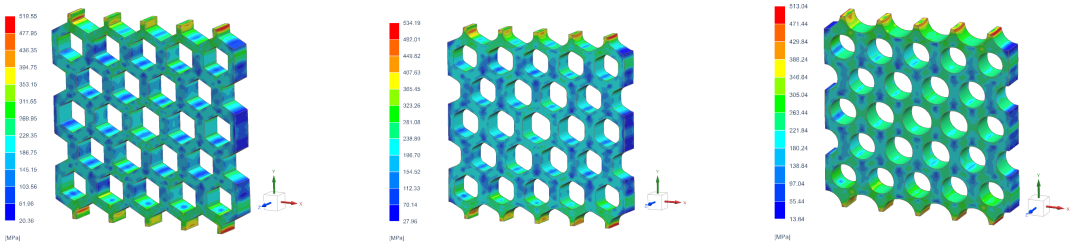

(a) (b) (c)

Figure A.9: von Mises stress of the (a) 2C, (b) 2C_Pt and (c) 2C_Lt.

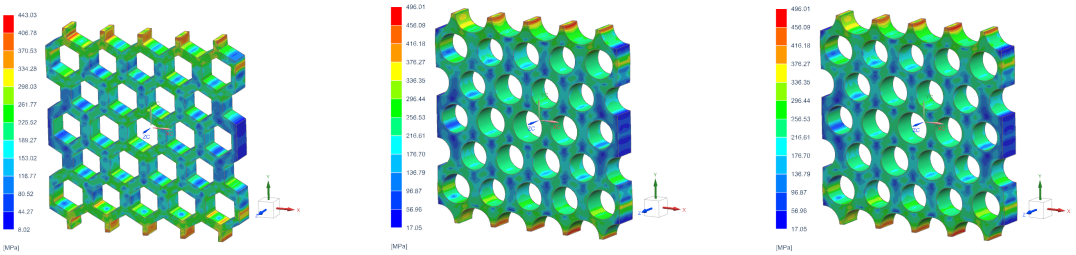

(a) (b) (c)

Figure A.10: von Mises stress of the (a) 2D, (b) 2D_Pt and (c) 2D_Lt.

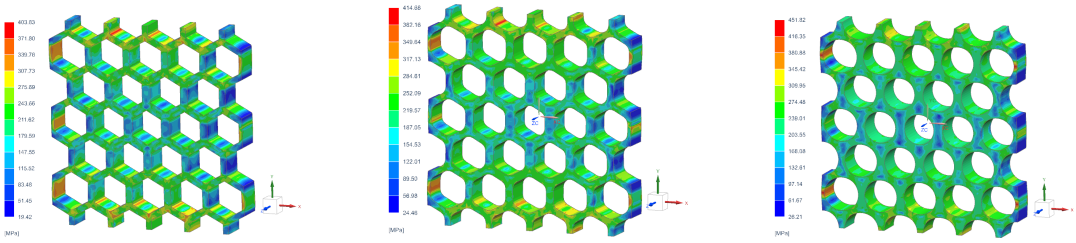

(a) (b) (c)

Figure A.11: von Mises stress of the (a) 3A+, (b) 3A+_Pt and (c) 3A+_Lt.

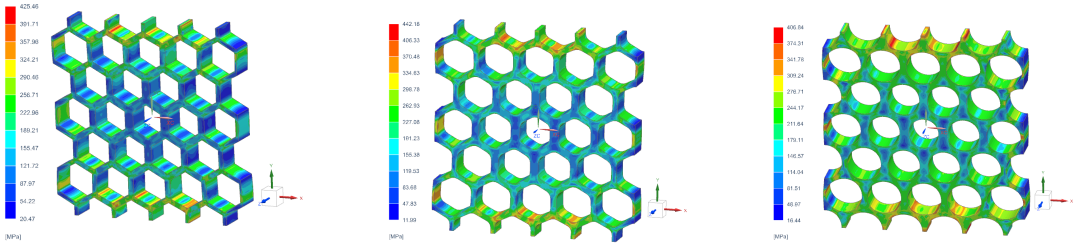

(a) (b) (c)

Figure A.12: von Mises stress of the (a) 3B+, (b) 3B+_Pt and (c) 3B+_Lt.

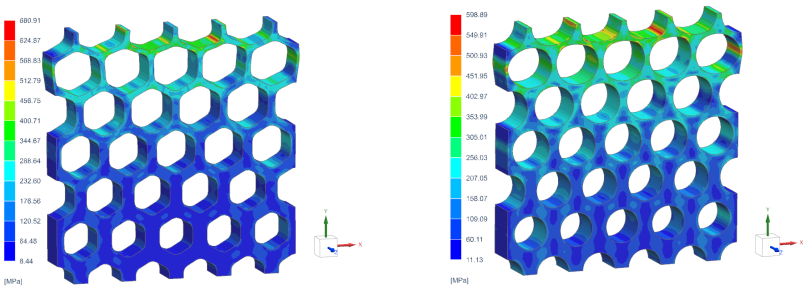

(a) **(b)**

Figure A.13: von Mises stress of the (a) 4B_Pt and (b) 4B_Lt.

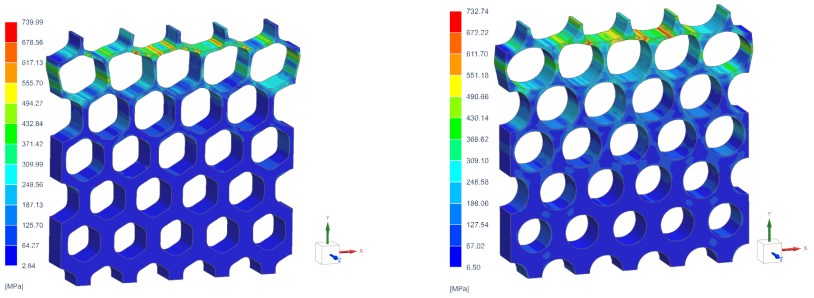

(a) **(b)**

Figure A.14: von Mises stress of the (a) 4C_Pt and (b) 4C_Lt.

B

Mechanical properties of the blocks for the performance analysis

The mechanical properties of the blocks used to determine the GEI in section 4.4 are presented in table B.1. As the plateau and lotus configuration structures have the same dimensions as the regular hexagon configuration, the dimensions for the regular hexagons will be presented.

Table B.1: Mechanical properties for the blocks.

Designation	Thickness [mm]	Height [mm]	Width [mm]	K^* [kN/mm]	${E_a}^*$ [J]	F_y [N]	σ_y [MPa]
L6	12	65.81	66	708.23	158.29	142076.2	179.389
L8	12	83.15	84	705.32	189.05	210254.4	208.586
L10	12	61.2	68	640.38	145.75	158768.7	194.569
1B	12	91.59	91.35	711.5	341.17	234695.165	214.099
2C	12	100.46	102	702.05	217.53	258001.084	210.785
2D	12			702.05	217.53	258001.084	210.785
3A+	12	88.51	90	701.4	197.7	210636.776	195.034
3B+	12			701.4	197.7	210636.776	195.034
3C-	12			701.4	197.7	210636.776	195.034
4A	12	86.6		686.76	193.35	206027.92	190.767
4B	12			686.76	193.35	206027.92	190.767
4C	12			686.76	193.35	206027.92	190.767
5HPL	12		105	583.27	180.16	221390.118	175.706
6HPL_-0.05	12			583.27	180.16	221390.118	175.706